The spatial distribution of soft X-ray selected AGNs at low redshifts

Dissertation
zur Erlangung des Doktorgrades des Fachbereichs Physik der Universität Hamburg

vorgelegt von
Frank Tesch
aus Bremen

Hamburg
2000

Gutachter der Dissertation:
Prof. Dr. D. Reimers
Prof. Dr. S. Refsdal

Gutachter der Disputation:
Prof. Dr. D. Reimers
Prof. Dr. J. H. M. M. Schmitt

Datum der Disputation:

Abstract

Within the ROSAC project, an international collaboration, optical follow-up spectroscopy has been carried out in order to reveal the AGN nature of candidates taken from the ROSAT All-Sky Survey (RASS). The goal of this project was the study of low redshift AGNs with regard to their clustering properties and the emergence of superstructures, that are formed by AGNs.

An area of 363.4 deg^2 in the constellation of Ursa Major ($8^h < \alpha < 11^h$, $45° < \delta < 58°$) was selected and a sample of 161 AGNs, in the redshift range $0.1<z<0.5$, was constructed. The surface density of $\sim$0.44 AGNs/deg^2 is the largest of soft X-ray selected AGNs ever gathered. The final AGN sample is about 81% complete, and the missing 19% had to be simulated.

Due to the inhomogeneous exposure times in the RASS, which led to a mountainous shape of the X-ray flux limits, the determination of the selection functions was a costly task. The main selection function was the X-ray luminosity function of the sample, that is consistent with formerly investigated samples of X-ray AGNs.

The clustering properties were explored by using the 2-point correlation function, $\xi(r) = (r/r_0)^{-\gamma}$. As comparison to the AGN sample random samples were generated by the means of the X-ray luminosity function, resulting in a clustering signal of $r_0 = 7 \pm 2 h^{-1}$Mpc with a fixed $\gamma = 1.8$ on scales $r < 10 h^{-1}$Mpc. This result is statistically insignificant due to the low number of AGN pairs on small scales. However, this trend could be confirmed with larger samples in the future.

The minimal spanning tree technique was successfully applied to search for superstructures within the AGN sample. Two new AGN groups on the 3.1σ and 2.1σ significance level were found. They contain 14 and 6 members at redshifts of $\sim$0.21 and $\sim$0.28, respectively. The number of superstructures found in the random samples is of the same order as for the AGN sample, which implies that such large structures resemble chance fluctuations.

Finally, dark matter N-body simulations in the form of a biased and an unbiased sample were used to examine the AGN clustering properties in a more detailed way. It turned out that the AGN sample was biased with respect to the unbiased dark matter in the Universe with a linear bias parameter of $b_{X-ray} = 1.5^{+0.2}_{-0.3}$. Moreover, it appeared that the probability of finding superstructures is dependent on the bias of the considered population. Nevertheless, it is unlikely to find an enhanced number of superstructures even in a weakly biased sample. This is another proof for the random character of superstructures in the Universe.

Altogether, the results of the ROSAC project in conjunction with earlier studies of AGN clustering and environments underline the requirement for a minor merging process as ignition of the nucleus activity in low luminosity AGNs at low redshifts.

Zusammenfassung

Die vorliegende Arbeit beschreibt die Ergebnisse einer Analyse der räumlichen Verteilung von Aktiven Galaxien Kernen (AGN) im Rotverschiebungsbereich $0.1<z<0.5$. Die AGN stammen aus einer im ROSAT All-Sky Survey (RASS) selektierten fluß-limitierten Stichprobe auf einer Fläche von 363.4 deg^2 im Sternbild Ursa Major. Die Identifizierung wurde im Rahmen einer internationalen Kollaboration, dem ROSAC Projekt, durchgeführt. Es wurde eine Vollständigkeit von 81% erreicht, so daß der unvollständige Teil der Stichprobe durch Zufallszahlenstichproben simuliert wurde.

Um Vergleichsstichproben für die statistische Analyse zu gewinnen, mußte die Auswahlfunktion bestimmt werden. Aufgrund starker Inhomogenitäten der Belichtungszeiten im RASS sind die abgeleiteten Flussgrenzen ebenfalls sehr unterschiedlich. Folglich ist die Bestimmung der Auswahlfunktion, die im wesentlichen durch die AGN Leuchtkraftfunktion gegeben ist, äußerst aufwendig. Erfreulich ist die gute Übereinstimmung der berechneten AGN Leuchtkraftfunktion mit früheren Arbeiten zu diesem Thema.

Für die Untersuchung der Clustering Eigenschaften wurde die 2-Punkt Korrelationsfunktion, $\xi(r) = (r/r_0)^{-\gamma}$, ausgewählt. Zufallsstichproben dienten als Vergleich zur wahren AGN Stichprobe, wobei ein Signal von $r_0=7\pm2h^{-1}$Mpc auf Skalen $r < 10h^{-1}$Mpc bei fest vorgegebenem Parameter $\gamma=1.8$ gefunden wurde. Wegen der geringen Anzahl von AGN in der vorliegenden Stichprobe ist dieses Ergebnis nicht signifikant. Dieser Trend kann jedoch in der Zukunft durch größere Stichproben bestätigt werden.

Die *Minimal Spanning Tree* Technik wurde erfolgreich zur Suche nach großräumigen Strukturen in der vorliegenden AGN Stichprobe angewandt. Zwei AGN Gruppen mit 14 und 6 Mitgliedern bei einer Rotverschiebung von $\sim$0.21 und $\sim$0.28 wurden auf einem Signifikanzniveau von 3.1σ und 2.1σ entdeckt.

Aus *Dark Matter N-body* Simulationen folgte, daß die AGN Stichprobe von einer nicht *gebiasten* Stichprobe abweicht. Diese Abweichung läßt sich durch einen linearen bias Parameter $b_{X-ray}=1.5^{+0.2}_{-0.3}$ beschreiben. Außerdem zeigte sich, daß stärker *gebiaste* Stichproben zu einer höheren Auftrittswahrscheinlichkeit von AGN Gruppen führten. Bei dem relativ schwachen *Biasing* der vorliegenden AGN Stichprobe ist es jedoch unwahrscheinlich, daß eine erhöhte Anzahl von AGN Gruppen gefunden wird. Dies unterstreicht den Zufallscharakter bzgl. des Auffindens von AGN Gruppen. Nichtsdestotrotz können diese Strukturen wahre Dichteerhöhungen auf großen Skalen im Universum nachzeichnen.

Insgesamt unterstützt das Ergebnis des ROSAC Projektes in Verbindung mit früheren Untersuchungen zum AGN Clustering und ihren kosmologischen Umgebungen *Minor Merging* Prozesse als auslösendes Ereignis der Kernaktivität in leuchtkraftschwachen AGN bei kleinen Rotverschiebungen.

Contents

List of Figures

List of Tables

Chapter 1

Introduction

The past few decades have led to a gigantic development in the field of cosmology, the formerly pursued issue of *chasing* after cosmological parameters is being superseded by the work on large-scale structures. In other words, attention is drawn on how the structures traced by matter (luminous material in form of galaxies) have evolved from tiny perturbations in the primordial density field visible as temperature fluctuations in the cosmic microwave background radiation. Early sky surveys aiming at collecting numerous galaxies revealed the first indications of cellular structures in the distribution of *local* galaxies, followed by the discovery of features like voids and superclusters, which in turn span a structural network. Due to their restricted luminosities, galaxies can only be observed in the nearby Universe and more powerful sources are needed in order to study large-scale structures in the far Universe. Quasars or Active Galactic Nuclei (AGNs) generate the required luminosities and are useful sources mapping structures in the deep Universe, where structure formation scenarios provide high density peaks as birth places for the first objects and/or agglomerations ever formed. Rich clusters of galaxies as well as quasars present populations that could reside in such density peaks, whereas groups of quasars could point to the largest peaks in the density field or to a few close density peaks, that could be the progenitors of superclusters in the local Universe. Especially, the lack of samples at intermediate distances, between the local Universe and the epoch when the number density of quasars peaked, has prevented us from making inferences of structure evolution. Within the scope of this work, light will be shed on this still *dark* issue.

1.1 Cosmology

The common basis for large-scale structure studies in the Universe is the knowledge of the applied cosmological model. Most of the cosmological models are based on an initial *Big Bang*, followed by an extremely short period, that is governed by quantum gravitation. This first fraction of the Universe history is still unknown, due to the lack of our knowledge on the theory of quantum

gravitation so far. Its threshold is given by the *Planck time* $t_p \approx 10^{-43}$s, where classical physics comes into play. Particles such as quarks are formed, while subsequent decrease of the temperature leads to the formation of larger particles: nucleons followed by the nucleosynthesis of D, ^{3}He, ^{4}He, and ^{7}Li. More and more nucleons and electrons 'recombine' to hydrogen chiefly, so that most of the electrons are absorbed. Now photons are unhindered, their mean free path length is of the order of c/H, and they decouple from matter. The Universe is still dominated by radiation (with respect to matter). The end of this era is marked by the formation of neutral hydrogen. This process, known as recombination, is also the birth of observational astronomy, since photon propagation was prevented before by Thompson scattering. Later on the transition from the radiation- to a matter-dominated Universe occurred by the virtue of their distinct energy density dependencies on the scale factor. This equality of matter and radiation density was accomplished at about $z \approx 1500$. The three redshift times for the processes of **photon decoupling** $z_{\rm dec}$, **H-recombination** $z_{\rm rec}$, and **matter-radiation equality** $z_{\rm eq}$ are given approximately by (Kolb & Turner 1990)

$$1 + z_{eq} = 2.32 \cdot 10^4 \, \Omega_m h^2 \approx 1500 \tag{1.1}$$

$$1 + z_{rec} = 1380 \, (\Omega_b h^2)^{0.023} \approx 1240 - 1380 \tag{1.2}$$

$$1 + z_{dec} = 1100 \, (\Omega_m / \Omega_b)^{0.018} \approx 1100 - 1200 \tag{1.3}$$

From now on matter governs the Universe and the radiation cannot prevent the gravitational growth of primordial density fluctuations anymore. The stage is open to the field of structure formation.

However, within the first moments of the Universe some enigmas were generated in the standard isotropic cosmology, such as the horizon problem, the flatness problem, and the expansion problem. An extremely fast expanding Universe for a short period could solve these problems. This phase is known as inflationary universe. The theory of inflation has been of paramount importance to cosmology, since it provides us with a model to overcome the shortcomings of the standard cosmology, and at the same time it explains the origin of initial inhomogeneities, the seedings for large-scale structures in the early Universe (Guth 1981, Kolb & Turner 1990, Linde 1993, Liddle & Lyth 1993, and references therein). Quantum fluctuations in the inflaton field whose vacuum energy drives inflation are responsible for the emergence of the seminal inhomogeneities that are imprinted in the temperature fluctuations of the Cosmic Microwave Background Radiation (CMBR).

The redshifted relic of the last-scattering surface is the CMBR. Penzias & Wilson (1965) serendipitously found this isotropic radiation at 7.35 cm with a temperature of 3.5 K. Further proof of such a radiation was made by the Cosmic Background Explorer Satellite (COBE), launched in 1989 (Smoot et al. 1990). The measured data showed a perfect blackbody spectrum with a temperature of (2.728±0.004) K (Wright et al. 1994, Fixsen et al. 1996). In the 1940s an *echo* from the Big Bang was already postulated at about 5 K (Gamov 1946 and Alpher & Herman 1948). Prior to this discovery, the excitation of

rotational energy levels in interstellar CN molecules in the direction toward the star ξ Ophiuchi showed the first fingerprint of a background radiation (McKellar 1940). Unfortunately, it was not recognized as being of cosmological origin. Recent high-resolution measurements of the interstellar lines of CN have strengthened the COBE result (Crane et al. 1986, Roth, Meyer and Hawkins 1993). Anisotropies in the CMBR have an immense meaning to the formation of large-scale structures and galaxies as well as to our knowledge of the early Universe. They are the first unambiguous visible seeds of density inhomogeneities in the Universe, the beginning of the growth of structures via gravitation. By all means, observational or theoretical results in the cosmological field of large-scale structures have to be reconciled with the CMBR.

1.1.1 Cosmological models

The assumption that the strongest force on large scales in the Universe is gravity, leads to the best available theory we have: Einstein's theory of general relativity. This theory describes gravity accurately well. The *cosmological principle* is a fundamental principle on which most cosmological models are based - at least on large scales. Moreover, it is independent of the theory for gravitation. The *cosmological principle* comprises the following statements regarding to the distribution of matter and radiation in the Universe:

HOMOGENEITY and ISOTROPY

An homogeneous Universe means a constant density, whereas isotropy can be described by *the same in all directions*. Interestingly, isotropy implies homogeneity, but not the reverse. The advantage of considering a homogeneous Universe is that our neighborhood becomes representative for the entire Universe. There is ample evidence for an isotropic Universe coming from the CMBR particularly. Implementing the motion of the Galaxy with respect to the cosmic rest frame (dipole anisotropy) the temperature of the CMBR is extremely uniform. Hence, an isotropic expansion of the Universe would lead to an anisotropy in the temperature measurements of the CMBR. Nevertheless, the first Redshift Surveys of galaxies in the local Universe, for instance CfA Redshift Survey (Huchra et al. 1983 (CfA1) and Huchra et al. 1999 (CfA2)), showed clearly inhomogeneities. How does it match to the cosmological principle? Firstly, these inhomogeneities arise on small scales only. Secondly, large-scale surveys, such as the Las Campanas Redshift Survey (Shectman et al. 1996), found an emergence of homogeneous patterns on scales $>100h^{-1}$Mpc (Tucker et al. 1997). Therefore, a transition from small scale inhomogeneities to a homogeneous Universe on large-scales does not jeopardize the cosmological principle.

Under consideration of the cosmological principle, the geometry of the spacetime can be described by the Robertson-Walker metric, which is the most general metric for this concern:

$$ds^2 = dt^2 - a^2(t)\left[\frac{dr^2}{1-kr^2} + r^2 d\theta^2 + r^2 \sin^2\theta\, d\phi^2\right] \tag{1.4}$$

where the spatial curvature k (-1,0,1) tells us whether space is hyperbolic, flat or spherical. The coordinates t, r, ϕ, and θ are referred to as comoving coordinates. The *cosmic scale factor* $a(t)$ describes the expansion of the Universe as a function of time, and is scaled to be unity at the present epoch $a(t=0) = a_0 = 1$. An homogeneous expansion therefore implies $r(t) = a(t)r_0$, where r_0 is any distance at the present epoch, and $r(t)$ describes this distance as a function of time.

The dynamics of the Universe is governed by the Friedmann equation, a particular solution of Einstein's field equations

$$\left(\frac{\dot{a}}{a}\right)^2 = \frac{8\pi G\rho}{3} - \frac{k}{a^2} + \frac{\Lambda}{3} \tag{1.5}$$

$$\frac{\ddot{a}}{a} = -\frac{4\pi G}{3}(\rho + 3p) + \frac{\Lambda}{3}. \tag{1.6}$$

The first equation is equal to H^2, which is the Hubble parameter whose current value at t_0 is denoted H_0. The Hubble constant describes the expansion of the Universe, its actual value is 71 ± 6 kms^{-1}Mpc^{-1} according to the Hubble Space Telescope Key Project on the Extragalactic Distance Scale (Mould et al. 2000). Usually the inverse and dimensionless Hubble constant $h = H_0/100$ is preferred, so that distances are given in units of h^{-1}Mpc (for H_0=100(km/s)/Mpc: h=1). Equation (1.5) means that three different terms drive the expansion of the Universe: a matter term Ω_m, a curvature term Ω_k, and a cosmological constant term Ω_Λ. Defining for the present epoch

$$\Omega_m = \frac{8\pi G}{3H_0^2\rho} \tag{1.7}$$

$$\Omega_k = -\frac{k}{a_0^2 H_0^2} \tag{1.8}$$

$$\Omega_\Lambda = \frac{\Lambda}{3H_0^2} \tag{1.9}$$

the first Friedmann equation can be written as

$$1 = \Omega_m + \Omega_k + \Omega_\Lambda. \tag{1.10}$$

This simple sum rule has been dubbed *cosmic triangle* (Bahcall et al. 1999), whereby an equilateral triangle is depicted by the three Omegas and every point within the triangle lies at an intersection of lines of constant Ω_m, Ω_k, and Ω_Λ. As of this writing new ideas pertaining the acceleration of the Universe are a matter of debate. In contrast to the cosmological constant Λ (a static uniform vacuum density) a dynamical form of evolving inhomogeneous dark matter, called quintessence, becomes more and more fashionable (see Caldwell et al. 1998, Ma et al. 1999, Wang et al. 2000, and references therein). Consequently, the triangle could be extended by adding fourth component (Ω_Q) in the future.

1.1.2 Gravitational growth of inhomogeneities

As we already know from the observational results of the CMBR and from the theory of inflation, density inhomogeneities were generated at an early stage of

the Universe. The regarded quantity is the **density contrast**

$$\delta(x) = \frac{\rho(x)}{\rho_0} - 1 \tag{1.11}$$

where $\rho(x)$ is the matter density at any location x in the Universe, and ρ_0 is the mean background density.

It is clear that gravitation is the dominant force, that governs the evolution of these small deviations from homogeneity and isotropy. If the mean free path of a particle is small, matter can be treated as an ideal fluid. In the Newtonian limit the motion of self gravitating particles can be described by the following set of equations:

- *Euler equation*

$$\frac{\partial(a\mathbf{v})}{\partial t} + (\mathbf{v}\cdot\nabla_{\mathbf{x}})\mathbf{v} = -\frac{1}{\rho}\nabla_{\mathbf{x}}\mathbf{p} - \nabla_{\mathbf{x}}\phi \tag{1.12}$$

- *Continuity equation*

$$\frac{\partial\rho}{\partial t} + 3H\rho + \frac{1}{a}\nabla_{\mathbf{x}}\cdot\rho\mathbf{v} = 0 \tag{1.13}$$

- *Poisson equation*

$$\nabla^{\mathbf{2}}_{\mathbf{x}}\phi = 4\pi G a^2(\rho - \rho_0) = 4\pi G a^2\rho_0\delta \tag{1.14}$$

These equations can be linearized under the condition that $\delta \ll 1$. As long as this condition holds linear theory is applicable. A linear second order differential equation is obtained for the linear density contrast under the assumption that pressure can be ignored (p=0)

$$\ddot{\delta} + 2H\dot{\delta} - \frac{3}{2}\Omega H^2\delta = 0. \tag{1.15}$$

For simplicity a spatially flat pressureless matter-dominated Universe is considered. Therefore, $\rho_0 = 1/6\pi G t^2$ and equation (1.15) gives two linearly independent power-law solutions $\delta(\mathbf{x},t) = D_{\pm}(t)\delta(\mathbf{x})$. The quantity $D_{\pm}(t)$ denotes the **linear growth factor** where $D_+(t) \propto a(t) \propto t^{2/3}$ is the growing mode and $D_-(t) \propto t^{-1}$ is the decaying mode. A more general expression of the growth factor in terms of the cosmic expansion factor is (Heath 1977 and Carroll, Press & Turner 1992):

$$\delta(a) = \frac{5}{2}\Omega_m\frac{1}{a}\frac{da}{d\tau}\int_0^a\left(\frac{da'}{d\tau}\right)^{-3}da' \tag{1.16}$$

where $\tau = H_0 t$ is a dimensionless time variable. Note that the expansion of the Universe suppresses the growth of structure formation, since the accretion onto the primordial density fluctuations is prevented by the expansion. The linear growth factor *dictates* how the density fluctuations evolve in the linear regime ($\delta \ll 1$) as a function of the background cosmology. Hence, it is interesting

to derive the linear growth factor in different cosmologies. The more simple cosmologies are those with $\Omega_k = 0$ and $\Omega_\Lambda = 0$. The linear growth factor is given by Sahni & Coles (1995) as

$$D_+(z) = \frac{1 + 2\Omega_m + 3\Omega_m z}{|1 - \Omega_m|^2} + 3\Omega_m \frac{(1+z)\sqrt{1+\Omega_m z}}{|1-\Omega_m|^{5/2}} f(\Omega_m, z), \tag{1.17}$$

where

$$f(\Omega_m, z) = -\frac{1}{2}\log[\frac{\sqrt{1+\Omega_m z} + \sqrt{1-\Omega_m}}{\sqrt{1+\Omega_m z} - \sqrt{1-\Omega_m}}], \tag{1.18}$$

$$f(\Omega_m, z) = \arctan\sqrt{\frac{1+\Omega_m z}{\Omega_m - 1}}, \tag{1.19}$$

for a closed ($\Omega_m < 1$) and an open ($\Omega_m > 1$) Universe, respectively. A good approximation for $\Omega_m \leq 1$ is

$$D_+(z) \simeq \left(1 + \frac{3}{2}\Omega_m\right)\left(1 + \frac{3}{2}\Omega_m + \frac{5}{2}\Omega_m z\right)^{-1}, \tag{1.20}$$

which, setting $\Omega_m = 1$ (standard cosmology), gives

$$D_+(z) \simeq (1+z)^{-1}. \tag{1.21}$$

The linear growth factor is normalized to $D_+(z=0) = 1$. The fitting formula for $\Omega_m < 1$ was taken from Peebles (1980) and is also discussed in Lahav et al. (1991). Another important case is that of a spatially flat ($\Omega_k = 0$) model with cosmological constant ($\Omega_\Lambda \neq 0$), so that $\Omega_\Lambda + \Omega_m = 1$. Now the growing mode of the linear growth factor is

$$D_+(z) = A\frac{5}{6}B_x\left(\frac{5}{6}, \frac{2}{3}\right)\left(\frac{\Omega_m}{\Omega_\Lambda}\right)^{1/3}\left[1 + \frac{\Omega_m}{\Omega_\Lambda(1+z)^{-3}}\right]^{1/2}, \tag{1.22}$$

$$x = \frac{\Omega_\Lambda(1+z)^{-3}}{\Omega_m + \Omega_\Lambda(1+z)^{-3}}, \tag{1.23}$$

where A is a constant calibrated by the value of $D_+(z=0) = 1$ and B_x is the incomplete beta function.

The statistics of primordial density fluctuations comprise the entirety of all modes. So far, the discussion was about a single Fourier mode $\delta(\mathbf{x}, t)$ only. The different modes usually have discordant amplitudes and a discussion can be done in the framework of Fourier transform. The Fourier modes, however, are statistically independent if the distribution is statistically homogeneous. Moreover, the Fourier modes would be eigenfunctions of the spatial translation operator $i\nabla_x$ and the density field would consist of a stochastic superposition of such modes with different amplitudes. The Fourier transform of the density contrast $\delta(\mathbf{x})$ and its inverse transformation $\hat{\delta}(\mathbf{k})$ are written as

$$\hat{\delta}(\mathbf{k}) = \frac{1}{(2\pi)^3}\int d^3\mathbf{x}\, e^{-i\mathbf{kx}}\delta(\mathbf{x}) \tag{1.24}$$

$$\delta(\mathbf{x}) = \int d^3\mathbf{k}\, e^{i\mathbf{kx}}\hat{\delta}(\mathbf{k}). \tag{1.25}$$

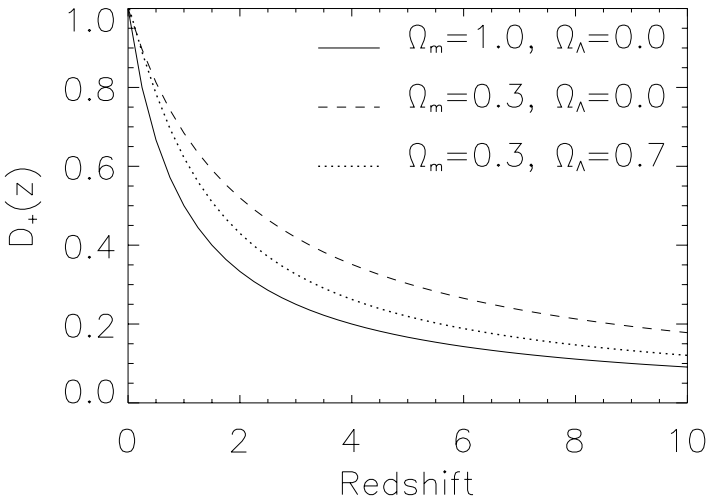

Figure 1.1: The linear growth factor for three different cosmologies is depicted as a function of redshift. For the model ($\Omega_m = 0.3, \Omega_\lambda = 0.7$) the normalization factor A is ~ 2.22.

The **power spectrum** P(k) of the density field can be expressed as a function of the variance of the amplitudes for a given **k**

$$< \hat{\delta}(\mathbf{k}_1)\hat{\delta}(\mathbf{k}_2) >= P(k_1)\delta^D(\mathbf{k}_1 + \mathbf{k}_2), \tag{1.26}$$

where δ^D is the Dirac delta function. That takes into account the symmetry for the power spectrum. Interestingly, the corresponding quantity in real space is the two-point correlation function, $\xi(r)$, or better autocovariance function, which can be derived from redshift surveys:

$$< \delta(\mathbf{x}_1)\delta(\mathbf{x}_2) >= \xi(|\mathbf{x}_1 - \mathbf{x}_2|) = \xi(\mathbf{r}). \tag{1.27}$$

The two-point correlation function is the Fourier transform of the power spectrum for a statistically homogeneous random field:

$$\xi(x) = \int d^3\mathbf{k} e^{i\mathbf{kx}} P(k) \tag{1.28}$$

$$P(k) = \frac{1}{(2\pi)^2} \int d^3\mathbf{x} e^{-i\mathbf{kx}} \xi(x). \tag{1.29}$$

This relation is known as the Wiener-Khintchin theorem (Coles 1996). Both the power spectrum and the two-point correlation function give a complete statistical characterization of the density field if this is a Gaussian random field. Inflationary theory predicts exactly this kind of field, that is generated by quantum fluctuations in a scalar field (Brandenberger 1985).

The need of a transfer function: The majority of the matter in the Universe is not made of atoms! The primordial power spectrum $P_p(k)$ describes the first

available mass spectrum of the Universe. Its evolution would simply scale with the linear growth law if there were not any other physical effects to consider. In reality the initial spectrum does not reach the present epoch unchanged due to physical processes that arise as soon as fluctuations enter the cosmological horizon. The primordial spectrum is influenced by cosmological parameters and by the form of non-baryonic matter. The type of non-baryonic matter plays a major role in reshaping the spectrum, whose influence is comprised in the **transfer function** $T(k)$, that logically transfers the primordial spectrum to the present epoch

$$P_0(k) = P_p(k) \cdot T^2(k). \tag{1.30}$$

Before discussing the transfer function in detail, statements should be made on the non-baryonic matter. Nowadays, three forms of non-baryonic dark matter are competing: (1) Hot Dark Matter (HDM), (2) Cold Dark Matter (CDM), and (3) Warm Dark Matter (WDM) or Mixed Dark Matter (MDM). The WDM and MDM model are just two expressions meaning the same. The HDM model refers to low-mass neutral relativistic particles such as neutrinos or the more exotic majorons. These particles have a cosmological number density comparable to that of photons, which imposes a restriction to their mass, $\Sigma m_i(\nu) \leq \Omega_\nu 92 h^2 \mathrm{eV}$. Neutrinos are responsible for a free streaming, so that small density fluctuations are smoothed out early and structures form at supercluster size with $M \approx 10^{15} M_\odot$, called Zel'dovich pancakes. Fragmentation of these pancakes leads to smaller and smaller structures. The main problem of this model, called top-down, is the formation of galaxy-like structures at a late stage of the Universe, z<2, (Subramanian & Padmanabhan 1993), which is ruled out by observations.

Weakly Interacting Particles (WIMPs) and Massive Astrophysical Compact Halo Objects (MACHOs) are the representatives of the CDM model. WIMPs and MACHOs are non-relativistic, thus an early suppression on small scales is prevented and structures form and grow according to the bottom-up scenario, which is also called the hierarchical model. Even though this model gives a better output than the HDM model and even though observed structures in the Universe are traced more convincingly, problems emerge as well. Specifically, the prediction of small scale clustering is too strong, whereas on large scales good agreement is achieved.

In cosmology, the two existing fluctuation modes are adiabatic and isocurvature. The latter perturb the entropy density but not the energy density, whereas adiabatic fluctuations affect the matter and radiation component in a way that the entropy does not vary spatially. As of this writing no successful model of structure formation has been constructed with isocurvature modes. However, adiabatic fluctuations are predicted by inflationary theories, which strengthen their selection. The growth of structures can be influenced by some processes on small scales: free streaming of dark matter particles at the speed of light can erase perturbations, relativistic particles may cause a suppression of structure evolution, and the coupling of photons and baryons can hamper the growth of the baryonic component. For statistically homogeneous initial Gaussian fluctuations these effects can be put together in a single function, the transfer function $T(k)$, that relates the primordial power spectrum $P_p(k)$, which is usually taken

to be proportional to a power law k^n, to the current power spectrum $P(k)$.

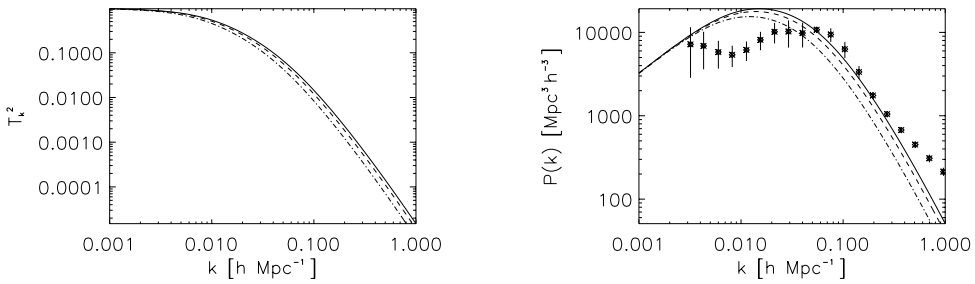

Figure 1.2: The CDM transfer function $T(k)$ and the power spectrum, according to equation (1.30), are shown for three different fits: Bardeen et al. (solid), Peacock & Dodds (dashed), and Sugiyama (dotted-dashed). The power spectrum is normalized to the microwave anisotropies, as given by the 4 year data from the COBE DMR experiment (Bunn & White 1997, Liddle et al. 1996), while applying a cosmology with $\Omega_m = 0.3$, $\Omega_\Lambda = 0.7$, and $H_0 = 70$. The right panel includes the estimated power spectrum (diamonds) from the APM angular galaxy catalogue (Gaztañaga & Baugh 1998).

Bardeen et al. (BBKS, 1986) presented a transfer function for a CDM model with adiabatic fluctuations from numerical calculations, that considers the physical processes responsible for the change of the primordial power spectrum:

$$T(k) = \frac{\ln(1+2.34q)}{2.34q} \cdot [1 + 3.89q + (14.1q)^2 + (5.46q)^3 + (6.71q)^4]^{-0.25} \quad (1.31)$$

with $q = k/(\Omega_m h^2)$, which includes the *shape parameter* $\Gamma{=}\Omega_m h^2$. Peacock & Dodds (1994) found a fitting solution for CDM models requiring $\Gamma = (0.255 \pm 0.017) + 0.32(1/n - 1)$. Furthermore, they note that the BBKS scaling applies for models with zero baryon content only and propose the scaling:

$$q = k/(\Omega_m h^2 \exp(-2\Omega_b)). \quad (1.32)$$

The primordial ratio of the number of deuterium to hydrogen nuclei created in the Big Bang nucleosynthesis is the most sensitive measure for the baryon density Ω_b. Quasar absorption systems give measurements of the primordial deuterium and the best value obtained recently in this way is $\Omega_b h^2{=}0.019{\pm}0.0024$ (Burles et al. 1999). Sugiyama (1995) verfied that Peacock's modification applies well for $\Omega_m{=}1$ models. However, further refinements are needed for low-density Universe models, since the effect of baryons is larger. Sugiyama proposed the following scaling:

$$q = \frac{k(T_{CMB}/2.7K)^2}{\Omega_m h^2 \exp(-\Omega_b - \sqrt{h/0.5}\Omega_b/\Omega_m)} \quad (1.33)$$

As long as the the density contrast is small ($\delta \ll 1$) linear theory gives excellent predictions of the growth of structures in the Universe. This regime breaks

down as soon as the density contrast approaches unity, and the transition to the quasi-linear and later to the non-linear regime is reached. The phases of the Fourier components $\delta_{\mathbf{k}}$ differ from their initial values and the power spectrum changes as well. Now, N-body simulations come into play (Bertschinger 1998) to overcome the problems that arise while entering the non-linear regime, where bound structures (e.g. galaxies) form. Physical processes like cooling, feedback and star formation as well as hydrodynamical effects (shocks) have to be considered. The spatial dark matter component is likely to differ from that of luminous material, which invoked the concept of **biasing**. Mass is only converted into light at the densest regions in the Universe, creating a luminous component more clustered than the mass (Kaiser 1984). It is useful to introduce the linear bias factor b,

$$\xi_{AGN}(r) = b^2 \xi_{mass}(r), \tag{1.34}$$

if $b = 1$ AGNs would perfectly trace matter in the Universe. It may be the case that each class of objects is biased in a different manner or, even worse, that the bias of the same class of objects is dependent on the selection criteria. For instance, X-ray and optical selected AGNs could be biased differently. In any case, the knowledge of the bias parameter, which is certainly not just a constant but a function of the mass and redshift, offers the opportunity to estimate the clustering properties of objects by applying dark matter N-body simulations. Collapsed dark matter haloes are generally considered as galaxies or AGNs in N-body simulations. Mo & White (1996) developed a simple analytic model for the gravitational clustering of dark matter haloes based on the Press-Schechter formalism (1974), which was tested against dark matter N-body simulations in order to understand how the spatial distribution of dark matter haloes (possible AGNs) is biased relative to that of the mass

$$b(M, z) = 1 + \frac{1}{\delta_{c,0}} \left[\frac{\delta_c^2(z)}{\sigma^2(M)} - 1 \right] \tag{1.35}$$

where $\delta_c(z)$ is the threshold density for the collapse of a homogeneous spherical perturbation at redshift z ($\delta_c(z) = D(z) \cdot \delta_{c,0}$). The quantity $\sigma(M)$ is called rms fluctuation of the linear density field on mass scale M, which is

$$\sigma^2(M) = \frac{1}{2\pi^2} \int_0^\infty k^2 P(K) W^2(kr) dk, \tag{1.36}$$

where the spherical top hat window function is given by

$$W(kr) = \frac{3(kr \sin kr - \cos kr)}{(kr)^3}. \tag{1.37}$$

Other smoothing filters as the spherical top hat window, which is frequently used, are conceivable (e.g. a Gaussian-filter).

1.1.3 Theory of Great Attractor-like structures

The growth of interest in incorporating superstructures in the theory of structure formation was ignited by the discovery of the Great Attractor (Lynden-Bell

et al. 1988). Further evidence for the existence of large structures came from the $128h^{-1}$Mpc periodicity of the galaxy distribution observed by Broadhurst et al. (1990), which originates from the tails of superclusters according to Bahcall's (1991) observational investigation. Despite the observational proof, such one-dimensional signatures of periodicity can arise in pencil-beam surveys as a result of small scale galaxy clustering (Kaiser & Peacock 1991 and Park & Gott 1991). Great Attractor-like structures are defined as places in the gravitational potential field where infall from all directions occurs. These superstructures result from the gravitational growth of initially small random Gaussian fluctuations. They may be at a quasi-linear or slightly nonlinear stage of evolution and may not have had enough time to form gravitationally bound system like clusters of galaxies. The clustering of Abell clusters (e.g. the Great Attractor consists of six such clusters) has been explained as being formed from rare peaks of primordial density fluctuations having random phases. It was shown that rare density peaks have enhanced correlations, that produce the required signal for Abell clusters in the two-point correlation function (Kaiser 1984). Under the hypothesis that AGNs reside in clusters of galaxies, one would expect similar correlations of about $20h^{-1}$Mpc for them leading to a few superstructures. Nevertheless, the large extensions (100-200h^{-1}Mpc) of AGN superstructures claimed to be found in observations (s. chapter 1.4.2) challenge large-scale structure formation scenarios, if they represent physical enhancements in the underlying density of the Universe (Bertschinger & Juszkiewicz 1988 and Silk & Weinberg 1991).

The theoretical approach to Great Attractor-like structures has always been based on the linear evolution of Gaussian density fields, that was carefully deduced by Bardeen et al. (1986; BBKS) in three dimensions. In this work they defined some parameters as follows:

$$\nu = \frac{\delta}{\sigma_0} \tag{1.38}$$

$$\gamma = \frac{\sigma_1^2}{\sigma_0 \sigma_2} \tag{1.39}$$

$$R_* = \sqrt{n}\frac{\sigma_1}{\sigma_2}. \tag{1.40}$$

The meaning of these parameters is: ν is the measure of the peak height in units of the rms density fluctuations σ of a given scale, γ is the width of the power spectrum, and R_* is a measure of the coherence scale in the field. The quantities γ and R_* are called *spectral parameters*, since they are related to various moments of the power spectrum

$$\sigma_j^2 = \int \frac{k^2}{2\pi^2} P(k) k^{2j} dk. \tag{1.41}$$

In order to smooth the density field on a certain scale two filters or smoothing functions are in use, a *Gaussian filter*

$$P(k, R_G) \sim e^{-(kR_G)^2} P(k) \tag{1.42}$$

and a *top hat filter*

$$P(k, R_{TH}) = \left(\frac{3(\sin(kR_{TH}) - kR_{TH}\cos(kR_{TH}))}{(kR_{TH})^3} \right)^2 P(k). \tag{1.43}$$

The mass enclosed by the two smoothing functions is the same for R_G=0.64R_{TH}, and the characteristic mass enclosed by a Gaussian smoothing function in the present Universe is

$$M_G = (2\pi)^{3/2}\rho_0 R_G^3 = 4.37 \times 10^{12} R_G^3 h^{-1} M_\odot. \tag{1.44}$$

The interesting quantity is the number density of peaks higher than a given height ν

$$n_{pk}(\nu) = \int_\nu^\infty N_{pk}(\nu')d\nu', \tag{1.45}$$

which is presented in BBKS (figure 3), whereas the asymptotic cumulative number of arbitrary heights can be evaluated analytically:

$$n_{pk}(-\infty) = 0.016 R_*^{-3}. \tag{1.46}$$

Using the above quoted relations, a simple estimation for superclusters of galaxies can be performed. The typical mass of a supercluster of galaxies is of the order of $10^{16}h^{-1}M_\odot$, which refers to a Gaussian smoothing scale of $13h^{-1}$Mpc. The spectral parameters for this scale are taken from BBKS (figure 1): $\gamma \approx 0.78$ and $R_* \approx 1.2R_G$. The number density over all heights gives $n_{pk}(-\infty) = 4.22 \cdot 10^{-6} h^3 \mathrm{Mpc}^{-3}$, which is certainly not more than an upper limit of the space density of superclusters of galaxies, since such big structures require large heights of the field ($\nu \gg 1$). Selecting ν=3 the product $n_{pk}(>\nu)\cdot R_*^3$ yields $\sim 1.5 \cdot 10^{-3}$ (figure 3 from BBKS) and $n_{pk}(>\nu) \approx 4 \cdot 10^{-7} h^3 \mathrm{Mpc}^{-3}$. In contrast, Abell clusters of richness class $\geq$1 have a space density of $\sim 6 \cdot 10^{-6} h^3 \mathrm{Mpc}^{-3}$, which can be derived from the BBKS formalism with the corresponding mass of clusters. At last, Heavens (1991) found that the number density of attractors is lower than the number density of peaks, by a factor of $[(n+5/n+1)]^{3/2}$ for Gaussian-filtered fluctuations with spectral index n, which is a factor of 5 for n=1.

Modeling of Great-Attractor-like structures exhibits that these large structures evolve from high-density peaks with overdensities $\delta \sim$ (1-2)/(z+1), peak-half widths $R_{\delta/2}$=(20-25)/(z+1)h^{-1}Mpc, and a mass $M_{GA} \sim 5 \cdot 10^{16} M_\odot$ (Hnatyk, Lukash & Novosyadlyj 1995). In all applied models (CDM, HDM, and MDM), they found that Great-Attractors are rare phenomena, only 150 of them reside in the contemporary horizon in the CDM model, while the numbers increase for the MDM model (N=720) and the HDM model (N=860). This result is supported by van Dalen & Schaeffer (1992), who estimated the number of Great Attractors based on a Gaussian smoothed amplitude of the density fluctuation on a scale of $24h^{-1}$Mpc of $\delta = 1.2 \pm 0.4$ (Bertschinger et al. 1990a) and the BBKS formalism. Their work clearly showed that the appearance of Great Attractors is enhanced in HDM cosmologies in comparison to CDM models.

Further evidence for the existence of Great Attractor-like structures or their precursors could be generated at the last scattering surface as $\Delta T/T$ spots in the maps of the CMB radiation. Bertschinger et al. (1990b) found that the gravitational potential field of the local Great Attractor and its surrounding regions produces a maximum Sachs-Wolfe[1] anisotropy of $\Delta T/T=(1.7\pm0.3)\cdot10^{-5}$ on an angular scale of 1° if the cosmological density parameter Ω is 1. This CMB anisotropy is slightly smaller than the upper limit on this scale, $\Delta T/T\leq3.5\cdot10^{-5}$ (Meinhold & Lubin 1991). For smaller values of Ω, the angular scale would decrease, while the amplitude $\Delta T/T$ would increase. The expected number of detectable hot spots for which $\Delta T/T$ exceeds the level of detection ($3\sigma_T \approx6.6\cdot10^{-5}$) depends on the cosmological model. A CDM model will produce ≈170 hot spots in the whole sky with $\Delta T/T\geq3\sigma_T$, which matches to the number of Great Attractors (N=150) found by Hnatyk, Lukash and Novosyadlyj (1995).

An analysis restricted to high-redshift AGNs (mainly quasars) made by Komberg & Lukash (1994) face the idea that AGN groups at z≈1-2 belong to concentrations of young clusters of galaxies, which are the progenitors of quasi-linear systems like the local Great Attractor. The power spectrum on scales 10-100h^{-1}Mpc, which ranges from the dynamical clustering scale to the coherence scale of Great Attractors, seems to be nearly flat: $\Delta_k \sim k^3P(k) \sim k^\gamma$ with $\gamma = 1^{+0.6}_{-0.4}$. The authors proposed three generations of quasars: (1) Early quasars at z≥3 of which only a small fraction is known today; (2) Quasars formed by the process of massive merging (major mergers) inside young groups of galaxies. This generation displays the majority of observable quasars and peak at z∼2-3; (3) Quasars in massive cD galaxies at low or intermediate redshifts. The most distant quasars are distributed randomly in space, whereas the second generation of quasars was born in density peaks, they are at least partially related to the formation of distant Great Attractors. First they were formed in (the central part of) protoclusters at z≈2.5, that evolve into progenitors of Great Attractors, which are seen as groups of AGNs. The era at which protoclusters (1-3h^{-1}Mpc) were formed may be reflected by the present epoch of Great Attractors, where only the central part became non-linear (10-30h^{-1}Mpc). Consequently, the density contrast at z≈2.5 averaged on the cluster window should be equal to that for z=0 averaged over the Great Attractors.

Since AGNs cover the entire redshift z=0-2.5, evolutionary studies of large-scale structures are in principle feasible, even if the number of objects is rather small. Specifically, the lack of low-redshifts samples of AGNs deeper than typical galaxy redshift surveys (z>0.1), still prevents an understanding of the evolution of structure on large scales.

[1]The Sachs Wolfe effect (1967) arose at the time of last scattering (recombination) due to gravitational perturbations. Photons that had to climb out of potential wells produced by high-density regions were redshifted and set their fingerprint in the cosmic microwave background as anisotropies.

1.2 Active Galactic Nuclei - AGNs

The expression *Active Galactic Nuclei*[2] (AGNs) refers to phenomena that occur in the central part of galaxies. Although evidence for the existence of different classes of galaxies had already started being gathered. At the beginning of the century, it was still a long way to the discovery of AGNs. The first optical spectra of galaxies, formerly called nebulae, with strong emission lines were obtained by Fath (1911). He wrote in his article: *..the spectra of spiral nebulae vary from one in which the bright lines of the gaseous nebulae are the most prominent features to one closely analogous to that of the sun.* A few decades later, Carl Seyfert (1943) obtained spectra of six extragalactic nebulae with high-excitation nuclear emission lines forming a class of objects with similar spectral characteristics. Nevertheless, the discovery of the enigmatic class of AGNs was a long time coming. The upcoming radio surveys within the 1950s and 1960s were the basis for the initial work on AGNs. The 3rd Cambridge Catalogue (3C, Edge et al. 1959) turned out to be the golden treasury. This catalogue contained 471 sources numbered sequentially by right ascension. Sources like 3C 48 and 3C 273 played a major role, since they showed extremely small angular sizes (star-like objects), strong emission lines, and a certain variability. Unlike earlier investigations Maarten Schmidt (1963), who took a spectrum of the optical counterpart of 3C 273, made the decisive claim that the 4 emission lines ([OIII], Hα, Hβ, and Hγ) in 3C 273 were redshifted by 16% equivalent to z=0.158. A second look on 3C 48's spectrum revealed a redshift of 0.368 (Greenstein & Matthews 1963). A new business of determining redshifts was born and many other AGNs were observed shortly after Schmidt's and Greenstein's publications. In order to produce the high luminosities of AGNs extreme physical conditions are required. Supermassive black holes were first suggested in the 1960s as explanation to the huge energetical outcome of AGNs (Salpeter 1964 and Lynden-Bell 1969). The importance of AGNs for galaxy formation and evolution was also recognized (Burbidge, Burbidge & Sandage 1963), since the growth of black holes is believed to be closely linked to galaxy formation. All the above combined with the fact that AGNs can be found over a large redshift range due to their high intrinsic luminosities motivated their search as well as the study of their characteristics.

1.2.1 Origin and formation of AGNs

AGNs release a big amount of energy in the form of radiation making them observable at large distances in different wavelength ranges. The fundamental question is how to generate the energy output. A first approach was made by invoking the gravitational nature of the phenomenon (Hoyle & Fowler 1963) and the existence of collapsed systems or super massive black holes. Arguments for

[2]The generic term AGN (singular) or AGNs (plural) is used throughout this thesis for any kind of object showing nuclear activity, such as Quasars, QSOs, Seyfert galaxies, BL Lacs, LINERs etc. Recall, that the first AGNs were called *quasi-stellar radio sources*, which was shortened to *quasars*.

the existence of such massive black holes could be provided by some dynamical search techniques (Kormendy & Richstone 1995).

The problem of the formation of AGNs was first addressed by Rees (1984), who presented a schematic diagram of possible routes for AGN evolution. The starting point is always a **gas cloud**, that evolves through several physical mechanisms into a **massive black hole**. By the virtue of Krolik (1999) three possibilities exist for the initial creation of black holes: (1) collapse of an isolated star, (2) merger of two neutron stars or (3) collapse of a gas cloud. The subsequent growth of the black hole (mass) can lead to super massive monsters required in AGNs to generate their gigantic luminosities.

An estimation of the mass of the central object can be made assuming an isotropic, ionized hydrogen gas in the stationary regime around a black hole. The forces exerted on the gas are the radiation pressure pointing outwards and the gravitation pointing inwards. In order to fuel an AGN the gravitational force must be larger or equal to the radiation pressure. This most simple scenario, *spherical accretion*, (no rotation of the black hole is assumed) was worked out by Bondi (1952) for accretion onto stars. Under the assumptions of a spherical accretion and the equilibrium between the radiation pressure and the gravitation, the maximum luminosity of a source with a given mass M, called Eddington luminosity L_{Edd}, is given by

$$L_{\rm Edd} \approx 1.26 \times 10^{38} \frac{M}{M_\odot} erg\, s^{-1}. \tag{1.47}$$

The typical luminosities of AGNs, $L \sim 10^{46}$ erg s^{-1}, imply central masses of the order of 10^8 solar masses (M_8). Several other quantities are associated to the Eddington luminosity: the Eddington accretion rate, at which emission at the Eddington luminosity can be sustained

$$\dot{M}_{\rm Edd} \approx 2.2 M_8 M_\odot yr^{-1}, \tag{1.48}$$

the Eddington time is defined as the time to *swallow* all the mass around it, while radiating at the Eddington limit.

$$t_{\rm Edd} \approx 4 \times 10^8 yr. \tag{1.49}$$

Infalling material into a black hole is assembled onto a disk, which is flattened due to the rotation of the black hole. The Lense-Thirring precession forces the disk to align with the black hole's angular momentum. Viscous dissipation in the disk heats matter which radiates energy, while spiraling inwards in order to compensate the energy loss. Finally, matter is *swallowed* by the black hole. For a rotating black hole angular momentum considerations discriminate between geometrically thin or thick accretion disks, that can be described as a function of the ratio of their height over their radius. In thin accretion disks the gas is in Keplerian orbit at each radius and slow radial infall occurs as viscosity transfers angular momentum outward. If the material is unable to cool and radiate away the energy dissipated by viscous friction, the disk becomes geometrically thick

(Rees 1984). The accretion rate at the outer part of the accretion disk governs the geometry of the disk, the higher the accretion rate is the thicker the disk is. The most direct proof of the existence of an accretion disk is the shape of the UV/optical continuum emission with the dominant feature of the *big blue bump* (Shields 1978 and Malkan & Sargent 1982). The origin of the big blue bump has been ascribed to thermal (non-stellar) local blackbody emission from the accretion disk.

After its formation, a super massive black hole's fueling is still a contentious issue, where the interstellar matter is channeled toward the center of the host galaxy. On its way to the center the matter has to cross a barrier of angular momentum and an efficient mechanism of extracting angular momentum from the gas has to be found. Two scenarios are principally competing: (1) bar-driven inflows and (2) galaxy encounters or mergers (Struck 1999). The nonaxisymmetric forces in the disks of barred galaxies lead to inward flows of the gas without the help of any kind of 'outer disturbances' such as interactions or mergers (Simkin et al. 1980 and Shlosman et al. 1990). Numerical simulations of disk galaxy mergers of comparable mass (called **major merger**) show strong gaseous inflows igniting heavy star formation and nuclear activity (Mihos & Hernquist 1996). In mergers between gas-rich disks and less massive dwarf galaxies (called **minor mergers**) dynamical friction decays the orbit of the satellite and large-amplitude spirals develop in the primary disk. The consequent nonaxisymmetric structures in the gas differ from those in stars, so that stars are enabled to torque the gas, which in turn, deprives the gas of its angular momentum funneling it inwards (Hernquist & Mihos 1995). The induced central activity may not happen earlier as the dwarf galaxy sinks to the central kiloparsecs of the massive galaxy. Barnes & Hernquist (1992) emphasized in their review about *Dynamics of interacting galaxies* that the triggering of AGN activity through mergers might be wishful thinking, just a few years before Hernquist performed the numerical simulations of major and minor mergers. The enormous development in this field has changed our view significantly. A more detailed discussion about evidences from observations for the onset and fueling of AGNs will be given in the discussions (chapter 5).

1.2.2 Spectral types of AGNs

After a brief presentation of the energy generation problem within the central part of AGNs, spectral types of AGNs are touched shortly. There is a big number of textbooks and publications available about this subject. For the ROSAC project, that aims at studying the clustering properties of AGNs in general, the individual spectral type is of no importance as long as the object matches the criterion to be classified as AGN. Notwithstanding, a short discourse about the AGN zoo may be of some help.

Common characteristics of quasars according to M. Schmidt (1969) are: very small angular size with a radio counterpart (star-like objects), time-variable continuum flux, large UV flux, broad emission lines, and large redshifts. Nowadays, not all of the above mentioned properties are necessary for an object to

be an AGN. In contrast to radio-loud objects, radio-quiet AGNs do also exist and their appearance in the Universe is about 10 times more frequent than for radio-loud AGNs. According to Wilkes & Elvis (1987) the radioloudness R_L is defined by the ratio of radio flux to optical flux as R_L=log$f_{\rm radio}/f_B$. AGNs are tossed into radio-loud objects if their radioloudness R_L >1. Another common feature of most AGNs is their X-ray emission (Elvis et al. 1978). Concerning the variability, it is interesting to note that its discovery was made even before the interpretation of redshifted emission lines in the optical spectra of 3C 273 (Smith & Hoffleit 1963). The timescales of variability varies from a few months down to a few days and even less, which clinches the size of the radiating region to the order of light days. Furthermore, variability has been found to occur at all wavelengths. The large UV flux originates from the thermal emission of the accretion disk, where the flux-peak of the entire AGN spectrum is reached at the *big blue bump* ($\sim$ 1100Å). Emission lines are a common feature of AGN spectra, apart from the class of Blazars[3], where emission lines are hardly found. In Blazars a relativistic jet points towards the observer and the continuum emission is enhanced, so that possible emission-lines are 'overpowered' (Blandford & Rees 1978). The emission-line regions are radially stratified with respect to the center of the AGNs, the broad-line region (BLR) is located closer to the central engine than the narrow-line region (NLR). Emission lines in both regions are triggered through photoionization of the ionized gas by the continuum radiation from the central source. In contrast to the BLR, the NLR is spatially more extended and its electron density is much lower allowing forbidden atomic transitions, whereas forbidden transitions are collisionally supressed in the BLR. Line widths in the BLR cover the range from $\Delta_{v_{\rm FWHM}}$ = 500 kms^{-1} to $\Delta_{v_{\rm FWHM}}$ = 10,000 kms^{-1} and the large Doppler widths lead frequently to blended lines. A good example for a feature of several blended lines is the *small blue bump* (Wills, Netzer, and Wills 1985), that consists of Fe II and Balmer emission lines. Typical broad-lines are Ly$\alpha\lambda$1216, C$_{IV}\,\lambda$1549, C$_{III]}\lambda$ 1909, Mg$_{II}\,\lambda$ 2798, H$\beta\lambda$ 4861, H$\alpha\lambda$ 6562. (A more detailed list of broad emission lines as well as narrow emission lines can be found in Cohen (1983) and Ferland & Osterbrock (1986).) Some prominent narrow emission lines are $[O_{II}]\lambda$ 3727, $[O_{III}]\lambda$ 4959, $[O_{III}]\lambda$ 5007, $[O_I]\lambda$ 6300 revealing line widths of $\Delta_{v_{\rm FWHM}}$ <500 kms^{-1}, narrower than those in the BLR.

Even though the spectral type for the ROSAC AGNs was not always determined due to already quoted reasons, at least some permanently appearing types are stressed here, such as Quasars, Seyfert galaxies, Low-Ionization Emission-line Region galaxies (LINERs), and Starburst galaxies. Even though the latter do not belong to the class of AGNs, their incorporation and relation to AGNs may become clear later. In the meantime, quasars and Seyfert galaxies seem to be forming a unique type in spite of their different luminosities. The limit M_B=-23 (La Franca & Cristiani 1997) has often been used as border between them,

[3]The term Blazar was introduced by E. Spiegel in 1978 in order to describe highly variable, polarized, and radio-emitting objects. Blazars comprise BL Lac objects and Flat Spectrum Radio Quasars (FSRQ), formerly known as Optically Violent Variables (OVV). BL Lac objects, in turn, are named after BL Lacertae, which was thought to be a variable star with a featureless spectrum: with weak or without any emission lines

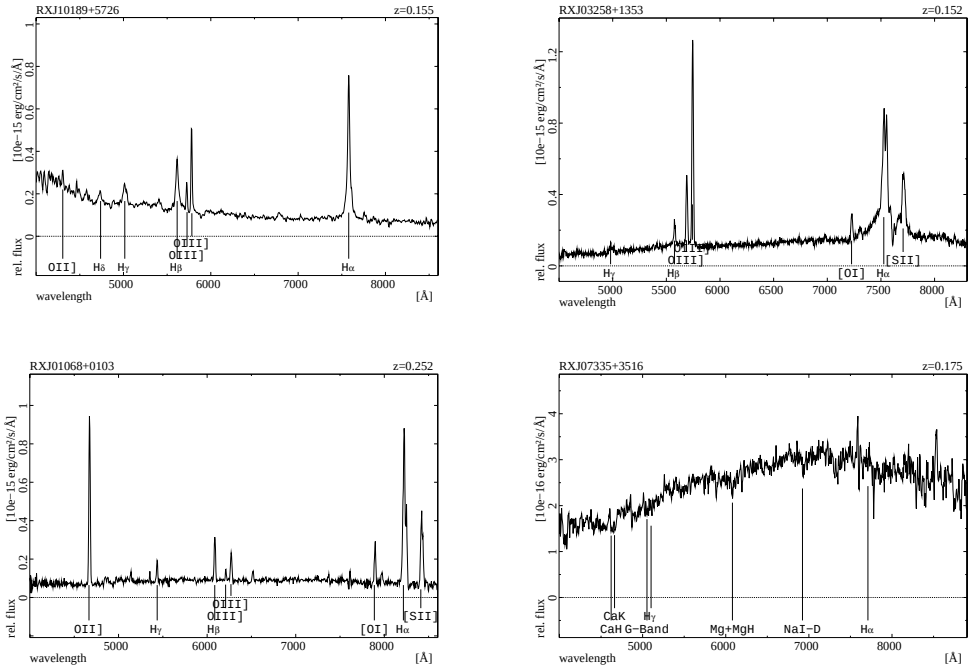

Figure 1.3: Optical spectra from the ROSAC project are shown in order to visualize the spectral features of four AGN classes. The upper spectra are Seyfert galaxies, on the left is a Seyfert 1 galaxy exhibiting the Balmer lines H_α, H_β, H_γ, H_δ, and O_{III}, on the right is a Seyfert 2 galaxy with $O_{III}/H_\beta > 3$ and strong S_{II} lines. The lower spectra present the LINER RXJ101068+0103 with strong O_{II} and O_I lines and a BL Lac object, that resembles a normal galaxy at a first glimpse. However, the weak Ca-break and the much stronger continuum in comparison to normal galaxies underline the AGN nature of this source. Further support for the classification as AGN is given by its large radio flux of 102 mJy at 1.4 GHz (NRAO VLA Sky Survey (NVSS), Condon et al. 1999).

Quasars being the brighter objects. However, this cut-off is not based on any physical arguments! Consequently, the question arises: is there still a need to distinguish between Quasars and Seyfert galaxies? At first, it has to be mentioned that two types of Seyfert galaxies exist: Seyfert 1 galaxies and Seyfert 2 galaxies. The latter ones are dominated by narrow-emission lines, whereas Seyfert 1 galaxies show broad-emission lines as well as narrow-emission lines resembling Quasars, only having lower luminosities and generally smaller redshifts. This spectral difference is explained in a simple model (Antonucci 1993) as orientation effect, where the Seyfert 2 galaxy is seen edge-on obscuring the central region and the Seyfert 1 galaxy face-on. However, Quasars do not show similar features to Seyfert 2 galaxies, which means that high-redshifted Seyfert 2 galaxies or type-2 quasars are unknown so far. Their discovery may come in the future, but as long as these objects are not observed the simultaneous use of the terms Quasars and Seyfert galaxies will be found in the literature.

A new class, named LINERs, having optical spectra dominated by emission-lines from low ionization species was defined by Heckman (1980). The line widths are similar to those in the narrow-line region, but with a lower luminosity. In contrast to Seyfert galaxies, lines such as $[O_{II}]\lambda 3727$, $[O_I]\lambda 6300$, $[N_{II}]\lambda 6584$, and $[S_{II}]\lambda\lambda 6717$, 6731 are strong in LINERs while $[O_{III}]$ is weak. Due to their low luminosity LINERs populate the faint end of the AGN luminosity function and their redshifts are small, so that the local Universe seems to be populated by numerous LINERs (Ho 1996). Another group of galaxies which is spectroscopically similar to H II regions comes up frequently in the Universe showing extended emission regions. Low-ionization lines such as $[O_I]\lambda 6300$ are generally weak (French 1980). Related to the group of H II region-like objects are the more luminous starburst galaxies (Weedman et al. 1981, Feldman et al. 1982 and Balzano 1983), both exhibit narrow emission line features, while broad emission lines usually lack. Their optical morphology resembles Seyfert galaxies having a bright, starlike nucleus. A hot and young star population is certainly responsible for the photoionization, which in turn provides the observable line properties (Huchra 1977). What remains is to find a way of separating AGNs from starburst galaxies resp. H II region-like galaxies spectroscopically. The current method is to consider emission line ratios. The criterion $[O_{III}]\lambda 5007/H\beta \geq 3$ turned out to be a good basis for defining an object as Seyfert 2 galaxy (Shuder & Osterbrock 1981), whereas most LINERs show $[O_{III}]\lambda 5007/H\beta < 3$ (Keel 1983). One criterion is certainly not sufficient for the separation, since some starburst also exhibit the same ratio of $[O_{III}]\lambda 5007/H\beta$ as Seyfert 2 galaxies do. A more detailed discussion of the spectral classification of emission-line spectra of extragalactic objects including further line ratios such as $[N_{II}]\lambda 6583/H_\alpha$, $[S_{II}]\lambda\lambda 6716{,}6731/H_\alpha$, and $[O_I]\lambda 6300/H_\alpha$ was done by Baldwin, Phillips & Terlevich (1981) and Veilleux & Osterbrock (1987). The importance of starburst galaxies in the study of AGNs is not only due to their spectral similarities, but also to the nuclear starburst scenario, which presents an ideal situation for the development of AGNs. The bursts of star formation supplies material for the accretion onto a black hole, since many massive stars are trapped in the nuclear region. The idea of transition from galaxies to AGNs, has been strengthened by studies of ultraluminous infrared galaxies (Sanders et al. 1988). The link between starburst galaxies (as progenitors of AGNs) and AGNs will be discussed extensively at the end in chapter 5.

1.3 Statistical tools

Many statistical tools, such as nearest-neighbor test, Kolomogorov-Smirnov test, Fourier power spectrum analysis etc., have been applied to study the clustering properties of galaxies, clusters of galaxies or AGNs. It turned out that the simple two-point correlation function method due to its direct relation to the mass power spectrum is mostly suitable for studying how objects cluster in space. The search for extended (super)structures is best examined by the three dimensional minimal spanning tree technique. Both statistical methods

are explained in this chapter.

1.3.1 Two-point correlation function

The distribution of objects in the Universe is according to the cosmological principle homogeneous and isotropic on large scales. However, on smaller scales ($\leq 100 - 200h^{-1}$Mpc) correlations between the positions of objects do exist due to the inhomogeneity of the Universe. At first only extragalactic nebulae (this expression has been transformed into galaxies) were regarded as tracers of structures, later on clusters of galaxies as well as AGNs followed.

Two different ideas were competing pertaining the description of the distribution of objects: firstly, the **cluster theory** which assumed that galaxies belong to clusters of galaxies which in turn are distributed in a random or a correlated way (Neyman & Scott 1952 and Neyman, Scott & Shane 1953). Secondly, a theory that considers galaxies as fluctuations in a density field (Limber 1953, 1954, 1957 and Rubin 1954). This idea is based upon a theory developed by Chandrasekhar & Muench (1952). Limber and Rubin preferred short-range functions of the form $\exp(-r^2/r_0^2)$ or $\exp(-r/r_0)$. However, this kind of functions is not appropriate for the present samples. The cluster theory and the fluctuation theory converge for a Gaussian-type cluster and a Gaussian-type correlation function (Neyman 1962).

An approach to find a well-fitted correlation function that has held up to now was done by Totsuji & Kihara (1969), who studied the distribution of galaxies (Shane & Wirtanen 1967). They published for the first time a power-law of the form $\xi(r) = (\frac{r}{r_0})^{-\gamma}$ with a correlation length $r_0 = 4.7$ Mpc and $\gamma = 1.8$. Notwithstanding, this work is permanently overseen and publications like Groth & Peebles (1977) or Peebles (1980) are cited instead. Admittedly, Peebles' textbook *The Large-Scale Structure of the Universe* (1980) is a milestone in the field of large-scale structures with its extended description of statistical tools, in particular of the two-point correlation function in space as well as in angular coordinates, and its link to structure formation via gravitational growth.

To introduce the concept of the standard correlation analysis the masses of galaxies or other extragalactic objects are neglected. The probability δP of finding an object in a small volume δV_1 and another in the volume δV_2 separated by a distance $\vec{r}_{12}$ is

$$\delta P = \bar{n}^2 (1 + \xi(\vec{r}_{12}))\, \delta V_1 \delta V_2, \tag{1.50}$$

where $\bar{n}^2$ is the mean number density of objects, which is independent of position and makes the correlation function dimensionless. The function $\xi(r)$ is called the *two-point correlation function*. In a uniform random Poisson point process where objects are distributed completely randomly the probabilities of finding objects within the volumes δV_1 and δV_2 are independent, so that $\xi(r_{12}) = 0$. If $\xi(r_{12}) > 0$, objects are clustered and if $\xi(r_{12}) < 0$ objects are anticlustered, they avoid each other. An appropriate fit to the current data on small scales

seems to be a power-law

$$\xi(r) = \left(\frac{r}{r_0}\right)^{-\gamma}, \tag{1.51}$$

where $\gamma \approx 1.8$ and r_0, called the *correlation length*. Of course, the correlation length depends strongly on the sort of objects, e. g. galaxies and clusters of galaxies show different clustering strengths. Another representation of the power-law is the following

$$\xi(r) = Ar^{-\gamma}, \tag{1.52}$$

where $A = r_0^{\gamma}$ denotes the *correlation amplitude*.

Interestingly, the integrated two-point correlation function $J_3(R)$ is directly related to the mass fluctuations (1.36) on the scale R,

$$J_3(R) = \int_0^R \xi(r) r^2 dr = \frac{R^3}{3}\sigma^2(R). \tag{1.53}$$

In principle, the normalization of the power spectrum for a given spectral index n can be derived from observations by calculating the integrated two-point correlation function. However, the two-point correlation function receives contributions on small scales that are dominated by nonlinear[4] effects/evolution, which have not been understood so far. Conversely, on larger scales the evolution is well described by linear theory, and the relation between the two-point correlation function and the mass fluctuations (expressed by $\sigma(R)$) turns out to be meaningful on scales R large enough to obey linear theory. The value $J_3(R)$ was determined for the CfA Redshift Survey to be $270h^{-3}$Mpc at R=$10h^{-1}$Mpc, and $600h^{-3}$Mpc at R=$30h^{-1}$Mpc (Davis & Peebles 1983). Root-mean-square mass fluctuations $\sigma(R)$ on these scales are easily yielded to be 0.9 and 0.25 respectively. Some problems arise by applying this normalization: the transition between nonlinear and linear theory is marked by $\sigma_m \approx 1$, which occurs at R $\approx$ $8h^{-1}$Mpc. To be sure of working in the range where linear theory is applicable means considering scales larger than $10h^{-1}$Mpc where the uncertainties of $\xi(r)$ increase. Additionally, it remains the well-known problem of *biasing*.

To circumvent the problems of nonlinear theory, density inhomogeneities have to be considered on larger scales. Hence, a **double power-law model** has been proposed to fit current samples of galaxies. The double power-law is defined by two slopes γ_1 and γ_2 for the small- and large-scale power laws, the separation scale r_s between these two regimes, an upper limit R_{lim} for the correlation, and the two amplitudes D_1 and D_2 for the two different regimes (Calzetti et al. 1992),

$$1 + \xi(r) = \begin{cases} D_1 r^{-\gamma_1} & r < r_s \\ D_2 r^{-\gamma_2} & r_s < r < R_{lim} \\ 1 & r > R_{lim} \end{cases} \tag{1.54}$$

It turns out that this kind of power-law extends the measurement of inhomogeneities up to scales of $30h^{-1}$Mpc well into the linear regime. Guzzo et al.

[4]The nonlinear regime is reached if the density contrast is $\delta \geq 1$, which is certainly the case for scales of galaxies. However, even larger scales of a few Mpcs are at least in the transitory range between the nonlinear and the linear regime.

(1991) analyzed a sample of galaxies in the Perseus-Pisces region, and fitted a double power-law to the data with $\gamma_1 = 1.8$ for r $\leq 3.5h^{-1}$Mpc and $\gamma_2 = 0.8$ for $3.5h^{-1}$Mpc < r $\leq 30h^{-1}$Mpc. Another investigation was carried out using the CfA1 survey (Dekel & Aarseth 1984). The authors fitted a double power-law up to $17h^{-1}$Mpc with a break at $3h^{-1}$Mpc, which is similar to Guzzo's result. The slopes were determined to be $\gamma_1 = 1.8$ and $\gamma_2 = 0.85$. The double-power law and its physical implications to the formation of large-scale structures can be regarded as an extension of the standard two-point correlation function, that has not gained acceptance so far.

In case the existing data set consists only of a projected two-dimensional catalogue of objects, then an **angular correlation function w(θ)** can be determined, defined in analogy to the spatial correlation function

$$\delta P = \bar{n}_\Omega^2 (1 + w(\theta_{12}))\delta\Omega_1 \delta\Omega_2, \tag{1.55}$$

which is the probability of finding two objects in the elements of solid angles $\delta\Omega_1$ and $\delta\Omega_2$ separated by an angle θ on the celestial sphere, with $\bar{n}_\Omega$ being the mean surface density of objects. The single angular power-law is given by

$$w(\theta) = \left(\frac{\theta_0}{\theta}\right)^{\gamma-1} = \frac{A}{\theta^{\gamma-1}} \tag{1.56}$$

One of the most useful aspects of the spatial and angular correlation functions is their relation to each other, which is given by the **Limber equation** (Limber 1954, Peebles 1980). Consequently, the spatial two-point correlation function can be extracted from the angular correlation function under certain assumptions: Clustering has to be considered as being independent on luminosity, known as *Limber hypothesis*, which appears to be verified by observations. Additionally, relativistic corrections can be ignored. The amplitude A of the angular correlation function is related to the one of the spatial correlation function, expressed by r_0^γ, through the equation (Peebles 1980):

$$A = r_0^\gamma \left(\frac{H_0}{c}\right)^\gamma \sqrt{\pi} \frac{\Gamma(\frac{\gamma-1}{2})}{\Gamma\frac{\gamma}{2}} \frac{\int_0^\infty dy \phi^2(y)[1+z(y)]^{-p} y^{5-\gamma}/F(y)}{[\int_0^\infty y^2 dy \phi(y)/F(y)]^2} \tag{1.57}$$

The parameter y is related to the redshift and to the matter density Ω_m as follows

$$y = 2\frac{(\Omega_m - 2)\sqrt{(1+\Omega_m z)} + 2 - \Omega_m + \Omega_m z}{\Omega_m^2 (1+z)}. \tag{1.58}$$

A substantially important function is the **selection function** $\phi(y)$, it can be written as

$$\phi(y) = \int_{L_{min}}^\infty \Phi(L) dL. \tag{1.59}$$

Finally, $F(y) = \sqrt{1 - y^2(\Omega_m - 1)}$.

The advantage of the angular correlation function is the possibility to circumvent the induced distortions by peculiar motions of galaxies.

Redshift space distortions - Real space. Linear theory predicts a boosted two-point correlation function measured in redshift space $\xi(r)$ with respect to

the real space function $\xi(s)$, since peculiar velocities distort the clustering signal in redshift-space (Kaiser 1987)

$$\xi(r) = \left(1 + \frac{2}{3}\frac{\Omega_m^{0.6}}{b} + \frac{1}{5}\frac{\Omega_m^{1.2}}{b^2}\right)\xi(s) \tag{1.60}$$

where b is the biasing factor. Later on (in chapter 1.5), the two-point correlation function in redshift-space as well as in real-space, derived from galaxy redshift surveys, will be presented.

The question how to derive practically the two-point correlation function $\xi(r)$ or $w(\theta)$ from an actual data set remains. For this purpose the number of pairs on a certain scale r has to be determined in the actual sample as well as in the random samples. The generation of the random samples is of paramount importance, since the same boundary conditions and the same selection function must be taken into account as in the real data set. The following estimators are used commonly, note that estimators are generally furnished with a $\hat{}$,

$$1 + \hat{\xi}_1(r) = \frac{DD(r)}{RR(r)} \tag{1.61}$$

$$1 + \hat{\xi}_2(r) = \frac{DD(r)}{DR(r)} \tag{1.62}$$

$$1 + \hat{\xi}_3(r) = \frac{DD(r) - DR(r)}{RR(r)} \tag{1.63}$$

$$1 + \hat{\xi}_4(r) = \frac{DD(r) \cdot RR(r)}{DR^2(r)} \tag{1.64}$$

$$1 + \hat{\xi}_5(r) = \frac{DD(r) - 2DR(r) + RR(r)}{RR(r)} \tag{1.65}$$

where $DD(r) = P_{DD}(r)/(N(N-1))$, $DR(r) = P_{DR}(r)/(NN_R)$, and $RR(r) = P_{RR}(r)/(N_R(N_R-1))$ are normalized counts, with N and N_R being the total number of objects in the actual data set and random-objects. P_{DD} is the number of pairs of objects in the separation bin r$\pm$dr/2 in the actual data set, P_{DR} pairs between random catalogue and actual data set, and P_{RR} pairs in the random catalogue. In practice, at least one of the presented estimators is calculated, but the advantages and disadvantages of the different estimators are mostly not considered. The first three estimators are introduced by Totsuji & Kihara (1969), Davis & Peebles (1983), and Hewett (1982). An examination of the bias and variance of the different estimators has been done by Landy & Szalay (1993). They recommend the fifth estimator over the first and second due to its variance that is effectively Poissonian, whereas the variance of other estimators are significantly greater than Poissonian. In contrast, Hamilton (1993) prefers the fourth estimator, which does not suffer from limitations on the uncertainty of the correlation function. A recent analysis (Kerscher 1999 and Kerscher, Szapudi & Szalay 2000) of the different estimators using the Virgo Hubble Volume simulation cluster catalog (Colberg et al. 1998) shows a comparable behavior of all estimators on small scales. On large scales the

fourth and the fifth estimators are superior with respect to the others, showing smaller deviations for a given cumulative probability.

The estimation of the statistical errors of the two-point correlation function has been discussed intensively in the literature (Peebles 1973, Peebles 1980 and Mo, Jing & Boerner 1992). Commonly used are Poisson error bars

$$\frac{\Delta\xi}{1+\xi} = \frac{1}{\sqrt{P_{DD}}}. \tag{1.66}$$

Another method to estimate the sampling errors is the **bootstrap resampling technique**, which has been proposed first by Barrow, Bhavsar & Sonoda (1984) and was applied in astronomy later on by Ling, Frenk & Barrow (1986). The bootstrap resampling technique uses the data under study making repeated random drawings to derive the sampling fluctuations. The error resulting from the bootstrap method gives errors that are $\sim \sqrt{3}$ larger than for Poisson errors at all scales (Mo, Jing & Boerner 1992).

At the end of this section **higher-order statistics** are stressed at least briefly. The two-point correlation function provides a complete description of clustering only in the case of a Gaussian distribution. This fact underlines the importance of the assumption that the primordial density fluctuations obey a Gaussian random field. However, the patterns of large-scale structures appear rather non-Gaussian (voids, great walls, clusters, filaments, sheets etc.), so that a really complete description of all these structures cannot be done with second-order statistics (two-point correlation function). Therefore, a series of N-point correlation functions are necessary. However, as long as Gaussian fields are considered all correlations above the two-point level either vanish, if odd, or can be expressed in terms of two-point functions, if even. Note, that all efforts, which have been undertaken to demonstrate the existence of non-Gaussian random fields, have failed so far (Benoist et al. 1999 and references therein). For example, topological-defect models entirely produce non-Gaussian perturbations.

1.3.2 Minimal Spanning Tree

A graph theoretical technique, called **minimal spanning tree (MST)**, is used to assess intrinsic patterns in a distribution of AGNs in space. The sensitivity to specific patterns, such as filaments, of the two-point correlation function is low, so that additional statistics must be used. The minimal spanning tree technique has been applied to other scientific problems, e.g. for minimal cost analysis in economy as well as for certain problems in chemistry and biology (Dussert et al. 1987), before it was adopted for astrophysical problems (Barrow, Bhavsar & Sonoda 1985). Details of the historical evolution of the MST technique are outlined in Graham & Hell (1985).

The data set (sample of AGNs) is termed as graph G and will be composed of nodes (AGNs) and edges (lines connecting AGNs). Each edge has a weight, which is the Euclidean distance between its nodes, and a sequence of edges joining nodes is a path. As soons as a path between any pair of nodes exists,

the graph is called connected. A connected graph, that contains no closed paths is a tree, which becomes a *spanning tree* if all nodes of the data set are included. Finally, a minimal spanning tree is the spanning tree with minimum length, where the length is just the sum over all lengths of all edges.

The search for superstructures of AGNs started with the simple construction of the three-dimensional MST for the entire AGN sample. Algorithms for this purpose were provided by Kruskal (1956) and Prim (1957), the latter has been used in this work. In order to get an idea of the scales at which superstructures can be found, the MST is separated at incremental distances of $1h^{-1}$Mpc. It means that all edges from the initial MST having a larger weight than the considered separation distance are erased and the remaining number of connected (sub)trees is counted at each separation distance. A single object without any connection to its neighbors is not considered as a tree, otherwise most of the structures would be counted at the smallest separation. The separation distance with the most numbers of connected structures is called *critical separation distance*, and this is the scale at which one has to look for superstructure candidates. Note, that if the separation distance is too small only pairs or triplets appear, whereas on large separation distances very extended structures are selected. The last step is to separate the MST at the critical separation distance. For each connected structure the median length of its edges has to be calculated and the structures are ranked with respect to this value. All structures, which consist of less than five members, should be erased from the list of ranked structures in order to pick only 'real' superstructures.

The determination of the significance level of the superstructure candidates is of paramount importance. A method, which has been successfully proven in two dimensions (Hoffman & Jain 1983 and Dussert et al. 1987, 1988), is the use of the normalized mean, m, and normalized standard deviation, σ, of the edge-lengths of the MST. An extension to three dimensions was presented by Graham, Clowes & Campusano (1995). The values m and σ have to be normalized to make a comparison of different distributions (AGN samples from different surveys) feasible. All edge-lengths are divided by $(N^2V)^{1/3}/(N-1)$, where N is the number of AGNs and V is the volume of the survey. As a comparison to the structure candidate m_R and σ_R from random generated MSTs, which have the same number of AGNs in the same volume, are obtained. The significance level of clustering in a candidate superstructure is determined by how many random MSTs have values of m_R and σ_R less than m and σ from the MST of the candidate. For the generation of 10,000 random MSTs the significance level in per cent is calculated by $(\mathrm{n}/10000)\cdot 100$, where n is the number of random MSTs for which $\mathrm{m}_R \leq \mathrm{m}$ and $\sigma_R \leq \sigma$.

This method was successfully applied to AGN samples by Graham, Clowes & Campusano (1995) as well as Tesch & Engels (2000), who found 4 new AGN groups in total (s. chapter 1.4.2).

1.4 Observational evidence for AGN clustering and groupings

1.4.1 AGN clustering

Historically, the spatial analysis of AGN clustering got started with the work of P. Osmer in 1981. Nevertheless, some angular double AGNs were discovered before (Stockton 1972, Wampler et al. 1973, Bolton et al. 1976) showing contradictory results concerning the angular pairing of AGNs. At this early stage of clustering investigations with AGNs the aim has been to find close pairs of some arcminutes distance without knowing the redshift of each objects. No significant pairing was found by Setti & Woltjer (1977) considering 175 UV excess (UVX) objects down to B=19.5 in a $6^\circ \times 6^\circ$ degree field (Braccesi et al. 1970), whereas another study found significant pairing within 2' around radio detected QSOs of UVX objects (Bolton et al. 1976). It turned out that all these pairs have had discordant redshifts.

A first attempt to study the spatial clustering of a sample of 174 high-latitude AGNs in the Cerro Tololo Inter-American Observatory (CTIO) surveys (Osmer & Smith 1980 and Osmer 1980) was performed in 1981 (Osmer 1981) showing a few close pairs and even groups of 3 and 4 objects with small redshift deviations. However, the subsequent statistical examination of the data yielded no significant clustering.

Investigating two AGN samples from Savage & Bolton (1979) on a surface of 25 deg^2 each (field size $5^\circ \times 5^\circ$), Chu & Zhu (1983) found contradictory clustering results, while applying the nearest-neighbor test and correlation function test: the sample of 124 AGNs centered on (02^h,-50°) showed the first significant clustering signal at all, whereas for the other sample of 116 AGNs centered on (22^h,-18°) no evidence for clustering showed up.

The early studies of AGN clustering suffered from low space densities within the samples, which restricted the analysis to larger scales ($\geq 100h^{-1}$Mpc). A large sample of over 2,000 AGNs with published redshifts (from the Véron catalogue) was used by Shaver (1984), who found an excess of AGN pairs on small separations ($< 5h^{-1}$Mpc). Only 2.4 pairs are expected for an unclustered population, whereas 12 pairs appeared in the sample. This result revealed AGN clustering, that is comparable to 'normal' galaxies at the current epoch.

Finally, the two-point correlation function as described in chapter 1.3.1 was used for the first time exploring a well-defined sample of 171 color-selected AGNs (Shanks et al. 1987), which is complete to z=2.2 and B≤21 mag. This sample was the first completed part of the Durham/AAT UVX survey (Boyle et al. 1990) comprising six 4.5×4.5 deg^2 areas. A 2.4σ clustering signal was detected at small scales, i.e. r≤10h^{-1}Mpc for q_0=0.5. At larger scales (10<r≤1,000h^{-1}Mpc) the correlation function is consistent with zero. Further support on large scales was provided by a study of 862 high-redshift (1.8<z<2.6) AGNs taken from six UK Schmidt objective prism plates covering ∼200 deg^2 (Drinkwater 1988). On intermediate scales (10-100h^{-1}Mpc, only this range was

regarded in this work) no evidence for clustering was reported underlining the small scale clustering properties of AGNs.

The advent of deep AGN surveys in the 80s offered further opportunities to study the clustering properties of AGNs. Iovino & Shaver (1988) combined 3 AGN surveys including the UVX selected sample of Shanks et al. 1987 of 171 AGNs. Another UVX survey provided 80 AGNs distributed on an area of 10 deg^2 with a magnitude limit of B=19.5 mag (Barbieri et al. 1987). The 3rd survey is based on Canada-France-Hawaii Telescope (CFHT) blue grens observations, contributing 125 AGNs brighter than B=20.5 mag on an area of 5.2 deg^2 (Crampton, Cowley and Hartwick 1987). The final sample consisted of 376 AGNs, which was divided into a low-redshift (z<1.5) sample and one at high-redshifts (z>1.5). The clustering signal found in earlier investigations at small scales (r<10h^{-1}Mpc) was confirmed on the 4.7 σ level in the low-redshift sample. At higher redshifts, on the other hand, the number of pairs is close to random expectations. Noteworthy, the clustering amplitude in this work turned out to lie between that of galaxies and clusters of galaxies. Following Shaver's examination from 1984, Chu & Zhu (1988) used the Hewitt-Burbidge QSO catalog (1987). In the catalogue are 3861 AGNs, of which 70 were not considered due to inaccurate coordinates. Evidence for AGN clustering on scales smaller than 10 h^{-1}Mpc are reported. A completely new result was that radio-loud AGNs showed stronger clustering than other types of AGNs. A negative clustering result of an inhomogeneous sample of 146 AGNs (Osmer & Smith 1980, Arp 1984, and Kunth & Sargent 1986) in the constellation Sculptor was presented by Anderson, Kunth and Sargent (1988), who applied the scrambling method to measure the correlation function. Here the random samples are generated by randomly permuting the redshifts in the original catalog. The strengths and weaknesses of this method as well as the selection effects of the sample have to be understood pretty well before applying it.

Six complete AGN surveys ((1) Large Bright Quasar Survey (LBQS, Hewett et al. 1995) at the stage of 1991 including 11 fields and 1006 AGNs, (2) Boyle et al. 1990, (3) Boyle et al. 1991, (4) Crampton et al. 1989, (5) La Franca et al. 1992, (6) Zitelli et al. 1992) were assembled for another AGN clustering study (Andreani & Christiani 1992) yielding 1642 AGNs. The surveys rely on different selection techniques, chiefly on UV excess and slitless spectroscopy. The UV excess catalogs were cut at a redshift of 2.2, while AGNs selected with slitless spectroscopy were accepted up to redshifts of 3.1. The clustering correlation length r_0 turned out to show a correlation length of 5.9h^{-1}Mpc, 4.1h^{-1}Mpc, and 3.2h^{-1}Mpc at average redshifts of 0.70, 1.44, and 2.15.

Another investigation of large scale clustering (r>10h^{-1}Mpc) using a sample of 723 AGNs taken from more than one survey was conducted by Mo & Fang (1993). 476 AGNs were taken from the Durham/AAT UVX survey (Boyle et al. 1990) and three randomly selected fields at high Galactic latitudes (Boyle, Jones and Shanks 1991). The second part of 247 AGNs stemmed from the CFHT grens survey (Crampton, Cowley and Hartwick 1989), where 23 AGNs forming a group of AGNs were excluded. The authors decided to

use the integral two-point correlation function $\bar{\xi}(r)$, which is related to the usual two-point correlation ξ by equation 1.53. Significant clustering was found for r$\leq 30h^{-1}$Mpc, while in the range $10\leq$r$\leq 50h^{-1}$Mpc $\bar{\xi}(r)$ is well described by a power law $\bar{\xi}(r) = (74 \pm 10)/r^{1.8}$ corresponding to a correlation length r_0 =$6.6h^{-1}$Mpc. A weakly significant (2σ) detection of an evolving clustering amplitude (A(z<1.5)/A(z>1.5)$\sim$2) was made.

The first clustering analysis of 183 X-ray selected AGNs at low redshifts (z<0.2) revealed a barely significant level of clustering $\xi(r < 10h^{-1}\text{Mpc})=0.7 \pm 0.6$ (Boyle & Mo 1993). The AGNs were taken from the published catalogue of the Einstein Extended Medium Sensitivity Survey (EMSS, Stocke et al. 1991), that extends to fairly bright flux limits S(0.5-2 keV)>10^{-13}ergs^{-1}cm^{-2} over an area of 770 deg^2.

An extension of the work of Andreani & Christiani (1992), who used 6 surveys (see above), was carried out by combining eight published samples of AGNs totalling 2,203 AGNs (Komberg, Kravtsov and Lukash 1994). They added the grism survey (Osmer & Hewett 1991) and an UVX survey (Warren, Hewett and Osmer 1991). Strong clustering was obtained in the AGN distribution at scales r<$20h^{-1}$Mpc. The correlation length was $r_0=6\pm1.2h^{-1}$Mpc with γ=1.8 for the entire sample. The clustering evolution of AGNs was studied by dividing the sample into subsamples with smaller redshift ranges. The characteristic scales r_0 are $8.5\pm4h^{-1}$Mpc,$10\pm2h^{-1}$Mpc,$4\pm3h^{-1}$Mpc for low ($0.1\leq$z<1.1), moderate ($1.1\leq$z<1.7), and high ($1.7\leq$z<4.5) redshifts, respectively.

A series of three papers about AGN clustering was written by T. Shanks and collaborators between 1994 and 1996. The first one (Shanks & Boyle 1994) combined the Durham/AAT UVX survey (Boyle et al. 1990), the ESO/AAT survey (Boyle et al. 1991, Zitelli et al. 1992), and the CFHT (Crampton et al. 1989) having 420, 83, and 215 AGNs in the redshift range 0.3<z<2.2. The statistical examination of the 718 AGNs supported the clustering result of Komberg et al. (1994) with a correlation length of $\approx 6h^{-1}$Mpc on a 4 σ level for the entire sample, which is not surprising, since this sample presents a subsample of the other larger one. A new feature was the 2 σ anticorrelation ($\xi \approx$-0.1) in the range 40<r<$100h^{-1}$Mpc. The second publication of this series aims at studying the clustering properties of IRAS Seyfert galaxies (Georgantopoulos & Shanks 1994). The Seyfert galaxies were selected from the IRAS Point Source Catalog (de Grijp et al. 1987) restricted to z<0.1 and a 60μm flux f_{60} >0.5 Jy. The sample consists of 192 Seyferts (of which 56 Seyfert 1s and 136 Seyfert 2s) satisfying the above criteria. Evidence for clustering at the 3 σ level at separations smaller than $20h^{-1}$Mpc was found: $\xi=0.51\pm0.15$ (z<0.02) and $\xi=0.80\pm0.34$ (z>0.02). Moreover, cross-correlation functions of the separate Seyfert 1 and Seyfert 2 galaxy samples with the IRAS galaxies were comparable, according to that Seyfert 1 and Seyfert 2 galaxies reside in similar environments on scales <$20h^{-1}$Mpc. The last work within this series used the LBQS (Hewett et al. 1995) plus the three samples from paper I (Shanks & Boyle 1994). For the LBQS individually a weak clustering signal at small scales was found, $\bar{\xi}(10h^{-1}\text{Mpc})=1.86\pm1.28$, only 5 AGN pairs within

$10h^{-1}$Mpc contributed. Adding the other three surveys the integrated two-point correlation function gives $\bar{\xi}(10h^{-1}\mathrm{Mpc})=0.83\pm0.29$, which is consistent with $r_0=5.4\pm1.1h^{-1}$Mpc and $\gamma=1.8$ for $\xi(r)$.

The Palomar Transit Grism Survey (PTGS, Schneider, Schmidt and Gunn 1994) provided another AGN sample, which is suitable for clustering studies. This survey, consisting of six narrow strips comprising an effective area of 61.47 deg^2, was designed to produce a sample of z>2.7 AGNs. Hence, two measurements were performed in 1997: (1) Kundić (1997) used 4 strips on an effective area of 50 deg^2 with 232 AGNs spanning the redshift range 0.7<z<4.7. Six pairs of AGNs gave rise to the detection of significant clustering at small scales r<$20h^{-1}$Mpc on a 2 σ level, whereas clustering was found on a 3 σ level for smaller separations r<$10h^{-1}$Mpc with $r_0\approx7h^{-1}$Mpc and γ=-1.8. The clustering amplitude ratio for the high- and low-redshift subsamples were $\xi(z>2)/\xi(z<2)=1.8^{+2.5}_{-1.2}$ significantly higher than the prediction for linear theory ($\xi(r)\sim D^2(z)$). (2) Stephens et al. (1997) focused on high-redshift (2.7<z<4.75) AGNs. They analyzed 56 of 90 high-redshift AGNs from two strips covering an area of ≈22 deg^2 that have redshifts in the quoted range. A very strong clustering signal was observed: $r_0=18\pm8h^{-1}$Mpc with $\gamma=1.8$.

A recent clustering analysis of an UVX selected sample of 388 AGNs with $M_B\leq23$ was presented by La Franca, Andreani and Christiani (1998). The sample includes AGNs as faint as B=20.5 distributed over a contiguous area of 24.6 deg^2 with redshifts in the range 0.3<z<2.2 (La Franca et al. 1999). The authors detected clustering on scales r≤$15h^{-1}$Mpc with $r_0=6.2\pm1.6h^{-1}$Mpc and $\gamma=1.8$, the corresponding integrated two-point correlation function was $\bar{\xi}(\mathrm{r}=15h^{-1}\mathrm{Mpc})=0.52\pm0.20$ at an average redshift of $\bar{z}=1.3$. Splitting the sample into two subsamples gave a clustering with $r_0=4.2\pm2.5h^{-1}$Mpc at low redshifts (0.3<z≤1.4, $\bar{z}=0.97$) and $r_0=9.1\pm2.0h^{-1}$Mpc at high redshifts (1.4<z≤2.2, $\bar{z}=1.82$), which strengthens the idea of an evolution in the AGN two-point correlation function in such a way that the signal increases with redshift.

Two different soft X-ray surveys, the ROSAT Deep Survey (DRS, Shanks et al. 1991) and the ROSAT International X-ray Optical Survey (RIXOS, Mason et al. 2000), providing 235 AGNs totally, were used to study the clustering of X-ray selected AGNs. Here, the first significant (2 σ) detection of clustering of AGNs from X-ray surveys was found on scales r≤40 - $80h^{-1}$Mpc for the RIXOS sample, while the DRS sample showed no clustering on any scales. Combining the limits from RIXOS with the DRS limits the authors obtained a correlation length which spans the range $1.5<r_0<5.5h^{-1}$Mpc depending on the assumed model for clustering evolution.

Sabbey et al. (2000) used an extragalactic Hα emission-line survey to extract 108 low-redshift (0.2<z<0.37, $\bar{z}=0.26$) AGNs. There were 19 pairs of AGNs with separations r<$20h^{-1}$Mpc, including two triplets and one quadruplet. The derived clustering signal on a 3 σ level turned out to be the strongest ever measured at low-redshifts, $r_0=14.6\pm3.3h^{-1}$Mpc and $\gamma=1.8$, which is consistent with that predicted for clusters of galaxies.

The newest investigation of the angular correlation function of 2,096 AGNs from

the ROSAT All-Sky Survey Bright Source Catalogue has been just submitted (Akylas, Georgantopoulos and Plionis 2000). A 4.3 σ signal between 2° and 8° was detected. The deprojection on three dimensions, applying the Limber equation, resulted in a spatial correlation length of r_0=6.0±1.6h^{-1}Mpc, which is consistent with earlier examinations

Summary: The conclusions, which can be drawn from all the mentioned spatial investigations using the two-point correlation function on small scales, are, that (1) AGNs are clustered without any doubts, (2) there seems to be an evolution of the clustering signal towards higher redshifts, and (3) at low-redshifts the clustering properties of AGNs and normal galaxies resemble each other.

Paper	N_{AGNs}	Sample	r_0 in h^{-1}Mpc	z range
Shanks '87	171	UVX Survey	≈6.0	$\bar{z} = 1.5$
Iovino '88	376	3 Surveys	≈7.9	$\bar{z} \sim 0.9$
Andreani '90	1642	6 Surveys	5.9	0.2 - 1.1
			4.1	1.1 - 1.7
			3.2	1.7 - 3.1
Boyle '93	183	EMSS	≈4.1	<0.2
Komberg '94	2203	8 Surveys	8.5±4	0.1 - 1.1
			10±2	1.1 - 1.7
			4±3	1.7 - 4.5
Shanks '94	718	3 Surveys	6.6	0.3 - 2.2
Georgantopoulos '94	192	IRAS PSC	6.6±2.6	<0.1
Croom '96	≈1700	LBQS + 3 Surveys	5.4±1.1	$\bar{z}$=1.5
Kundić '97	232	PTGS	≈7	0.7 - 4.7
Schneider '97	56	PTGS	18±8	2.7 - 4.75
La Franca '98	338	UVX Survey	6.2±1.6	$\bar{z}$=1.34
	221		4.2±2.5	$\bar{z}$=0.97
	167		9.1±2.0	$\bar{z}$=1.82
Carrera '98	235	RIXOS + DRS	1.5 - 5.5	0.5 - 1.0
Sabbey '00	108	Hα Survey	14.6±3.3	$\bar{z}$=0.26

Table 1.1: Results of the two-point correlation function $\xi(r) = (r/r_0)^{-\gamma}$ for AGNs with γ=1.8 and q_0=0.5 are depicted. The first author of the publication, numbers of used AGNs, the origin of the sample, the correlation length r_0 in h^{-1}Mpc, and the redshift range or the average redshift of the sample are quoted.

1.4.2 Groups of AGNs

The search for *superstructures*, agglomerations at least as big as *local* superclusters, has become possible with the growing numbers of AGNs. Nevertheless, such a search has not been supported by all scientists, which was clearly demonstrated by the refusals of applications for observing within the scope of the ROSAC project. More successful have been proposals that aimed at studying the evolution of the two-point correlation function of AGNs. One of

the main drawbacks of this subject is the fact that these structures are obviously not bounded in a gravitational manner in contrast to clusters of galaxies, for instance, which makes a physical explanation even harder. A handful of AGNs distributed in a volume of 100-200 h^{-3}Mpc^3 cannot be related among themselves through gravitation. Despite this logical argument, some significant superstructures have been found.

Surprisingly, at an early stage of the spatial clustering analysis of AGNs the first superstructure or group of AGNs was detected (Webster 1982), in which the CTIO sample from Osmer (1981) was subjected to a Fourier Power Spectrum Analysis in order to seek for clustering signals. The only signal arose from a group of four AGNs at z=0.37 located in the Sculptor constellation, which has a projected extension of $60 \times 70h^{-2}$Mpc^2. The author found a probability of 10^{-4}-10^{-7} for the group to be a chance fluctuation, which indicates the nature of real structure. Due to close redshifts of the four group members, the structure's shape is flat. This flatness fits with the idea that it is a supercluster, because known examples of them are rather elongated than spherical (Oort 1981). Interestingly, a further member (A1310, z=0.36) of the group was discovered (but not recognized as such) by the Calan-Tololo Survey (Maza et al. 1995).

A more convincing group of AGNs, due to numerous members, was presented by Crampton, Cowley and Hartwick (1989) investigating a sample of 248 AGNs from the CFHT Survey (Crampton et al. 1987). The AGN group comprises 23 members with 1.0<z<1.2 and an average redshift of $\bar{z}$=1.113. Its dimensions are $\sim 45h^{-1}$Mpc in depth and $\sim 60h^{-1}$Mpc in angular coordinates. Applying the two-point correlation function method to this sample a clustering signal appears on scales r<$10h^{-1}$Mpc, which essentially comes from the group of AGNs.

Evidence for a large elongated group of 13 AGNs was found by Clowes & Campusano (1991), who used the two dimensional Fourier Power Spectrum Analysis. They studied an own defined sample of 56 AGNs in a field of 25.3 deg^2 (Clowes & Campusano 1994). The largest dimension of this group is 100-200 h^{-1}Mpc at z$\sim$1.3 and its morphology looks like a clump, but sub-grouping on scales $\sim 20h^{-1}$Mpc may occur. A recent work stressed the existence of at least 18 members in this group (Clowes et al. 1999).

The minimal spanning tree technique, a three dimensional technique, for the search of superstructures was introduced by Graham, Clowes & Campusano (1995). They illustrated the strength of this method by applying it to six surveys, three of them including all known superstructures at that time (s. above). These three structures were rediscovered and in the other three surveys another two were found additionally. One of them consists of 10 AGNs at z$\sim$1.9 and the other is a group of 7 AGNs at z$\sim$0.19. The former group has a size of $\sim 120\times90\times20h^{-3}$Mpc^3 and the latter $\sim 60\times30\times10h^{-3}$Mpc^3.

For the purpose of searching for further groups of AGNs Komberg, Kravtsov & Lukash (1996) used the 5th edition of *A catalogue of Quasars and Active Nuclei* (Véron-Cetty & Véron 1991). Their method applied was the friend-of-friend technique (Einasto et al. 1984), which is also known as percolation

method, adopting the following selection criteria: the group considered should have at least 10 members and the AGN number density in a group must exceed that of the background by at least a factor of 2. Totally 12 AGN groups were detected in their analysis, one of them turned out to be a rediscovery from an earlier investigation. The other four groups formerly found did not match the selection criteria, so that their redetection was not possible. The sizes of the 12 groups range from 70 to 160 h^{-1}Mpc.

A detection of a further AGN group was reported from the Chile-UK Quasar Survey, which is a 140 deg^2 UVX survey down to B=20. The group of 13 AGNs spans $\sim 150h^{-1}$Mpc at z$\sim$1.5 and was found by using the minimal spanning tree technique (Newman et al. 1998). Moreover, the group found by Clowes & Campusano (1991) has been confirmed in this independent sample.

Finally, Tesch & Engels (2000) reported the detection of the *Pisces AGN Group*, which is the first X-ray selected AGN group ever. The application of the minimal spanning tree technique led to 1.8 σ discovery of an AGN group consisting of 7 members in the Pisces constellation. The group extends over $140\times75\times75h^{-3}$Mpc^3 at a mean redshift $\bar{z}$=0.27.

From the observational point of view we are now aware of 18 AGN groups having extensions of 60-200h^{-1}Mpc so far. These sizes are significantly larger than typical sizes $\leq 30h^{-1}$Mpc of superclusters (Oort 1983, Bahcall & Soneira 1984, Postman, Geller, and Huchra 1988) challenging structure formation theories.

1.5 Large-scale structures traced by non-AGN objects

The results of AGN clustering studies have to be compared with the clustering properties of non-AGN objects in order to learn how these structures have evolved and to understand where to incorporate them into the existing structure network. Naturally, galaxies offer a great opportunity for comparisons due to the large number of objects with known redshifts, in particular at lower redshifts (z<0.2), where some redshift surveys have been completed. In contrast to galaxies, clusters of galaxies provide samples (e.g. Abell catalogue) to higher redshifts because of their larger luminosities. Finally, at the upper scale (100-200h^{-1}Mpc) of known structures, superclusters (defined as agglomerations of clusters of galaxies) mark the most challenging pieces of the structure network. Here, some selected surveys are presented intending to measure how the abovementioned objects cluster in the Universe.

1.5.1 Clustering of Galaxies

In a first attempt to fit a two-point correlation function to the results from a clustering investigation, the **Shane-Wirtanen catalog of galaxies** was used. (Totsuji & Kihara 1969 and Groth & Peebles 1977). Groth & Peebles calculated the two-point angular correlation function due to missing redshifts of some

galaxies within the catalog and applied Limber's equation in order to estimate the spatial correlation function, which they found to be $\xi(r) = (r/r_0)^{-1.77}$ with $r_0 = 4.7h^{-1}$Mpc.

The **CfA Redshift Survey** provided a well-defined sample of galaxies for studying the spatial distribution of these objects. Davis & Peebles (1983) used the CfA1 sample (Huchra et al. 1983), which is limited to $m_B \leq 14.5$, and derived the spatial two-point correlation function in the fiducial model of Groth & Peebles (s. above, γ=1.77) with a correlation length of $r_0 = 5.4h^{-1}$Mpc. Another clustering analysis of two slices of the extended CfA2 Redshift Survey (de Lapparent, Geller & Huchra 1986), which is restricted to $m_B \leq 15.5$, comprised 1,810 galaxies and yielded a two-point correlation function[5] $\xi(r)$ with $\gamma \approx 1.6$ and $r_0 \approx 7.5h^{-1}$Mpc (de Lapparent, Geller & Huchra 1988).

A first investigation of the galaxy-galaxy autocorrelation function for the **Las Campanas Redshift Survey (LCRS)** was presented by Tucker et al. 1997. They found a power law fit for separations $2.0 < r < 16.4h^{-1}$Mpc with correlation length $r_0 = 6.28h^{-1}$Mpc and slope $\gamma = 1.52$. Interestingly, a zero-crossing could be found on scales of 30-40 h^{-1}Mpc. The LCRS consists of six 1°.5 × 80° slices and extends to a redshift of ~ 0.2. The entire sample contains 26,418 galaxies. Jing et al. (1998) showed that the two-point correlation function of galaxies from the LCRS can be taken reliably by using high-resolution N-body simulations. The real-space correlation function is well fitted with $s_0 = 5.06h^{-1}$Mpc and $\gamma = 1.862$.

The **Stromlo-APM redshift survey** (Loveday et al. 1992) consists of 1,787 galaxies down to a magnitude limit of B=17.15. The survey strategy was to pick galaxies at a rate of 1 to 20 randomly, a method called sparse-sampling selection. Kaiser 1986 discussed this strategy in more detail regarding the search for large-scale structures. Later on, the estimates for the two-point correlation function for all galaxies on scales 0.2 - $20h^{-1}$Mpc gave a slope $\gamma = 1.71$ and $s_0 = 5.1h^{-1}$Mpc in real space. In redshift-space the correlation length is slightly higher with $r_0 = 5.9h^{-1}$Mpc and a slope $\gamma = 1.47$ (Loveday et al. 1995). An approach to consider morphological differences and luminosity showed that early-type galaxies are clustered more strongly than late-type galaxies, while low-luminosity galaxies are less clustered by a factor of ∼2 than L^* and even brighter galaxies.

The spatial clustering of galaxies in the **Canada-France Redshift Survey (CFRS)** was also calculated from the angular correlation function. This investigation comprises 591 galaxies with redshifts in the range $0 \leq z \leq 1.3$, in five CFRS fields (Le Févre et al. 1996). The sample is fitted by $\gamma = 1.64$ and the amplitude of the correlation function shows a strong decline with redshift resulting in $r_0(z = 0.53) = 1.33h^{-1}$Mpc, which is about a factor of 10 smaller than for the local galaxy population on scales $0.1 < r < 2\ h^{-1}$Mpc. Red and blue galaxies cluster similarly at $z \geq 0.5$, whereas red galaxies are more strongly correlated than blue galaxies.

[5] r refers to the correlation length in redshift-space,whereas s is measured in real-space

Guzzo et al. (1997) studied the clustering of different galaxy types in the **Pisces-Perseus redshift survey**. Their result for the early-type population was $s_0 = 8.35h^{-1}$Mpc, $\gamma = 2.05$, and $s_0 = 5.55h^{-1}$Mpc, $\gamma = 1.73$ for spirals and irregulars, respectively. They claim that redshift space distortions affect morphological types in a different way, particularly on small scales where the major effect comes from the virialized centers of clusters, the preferred location of ellipticals. Consequently, a comparison of the clustering strength of different morphological types can only be made in real-space.

The **ESO Slice Project (ESP)** is a galaxy redshift survey at the southern hemisphere consisting of two strips 1° thick in declination each, one is 22° long in right ascension and the other is 5° long. The total coverage is about 25 deg^2 and galaxies were detected down to B_J=19.4. The clustering in real-space below $10h^{-1}$Mpc is well described by $s_0 = 4.15h^{-1}$Mpc and $\gamma = 1.67$ (Guzzo et al. 2000).

The *Infrared Astronomical Satellite* (IRAS) data base provides another interesting opportunity, since it is an all-sky survey, to study the clustering properties of 5313 galaxies. Clustering in the **1.2-Jy IRAS Galaxy Redshift Survey** was measured as $\xi(r) = (r/4.53)^{-1.28}$ in redshift-space on scales $\leq 20h^{-1}$Mpc and $\xi(s) = (s/3.76)^{-1.66}$ in real-space on the same scales (Fisher et al. 1994). An optical-to-IRAS bias ratio of b_O/b_I=1.38 on a scale of $8h^{-1}$Mpc was derived from comparisons of the $\xi(r)$ correlation function.

Hermit et al. (1996) conducted the **Optical Redshift Survey (ORS)** considering subsamples within their survey they came upon variations in the two-point correlation function. According to this effect their best-fit values indicate a range: $1.5 \leq \gamma \leq 1.7$, $6.5 \leq r_0 \leq 8.8h^{-1}$Mpc in redshift-space and $1.5 \leq \gamma \leq 1.7$, $4.9 \leq s_0 \leq 7.3h^{-1}$Mpc in real-space.

A sample of 183 field galaxies from the Canadian Network for Observational Cosmology cluster survey (**CNOC**) at a median redshift of 0.37 exhibited weak clustering. The real space correlation function was fitted with γ=1.7 and $s_0 = 1.9^{+0.4}_{-0.4}h^{-1}$Mpc (Shepherd et al. 1997).

Another low-redshift project is the **Two Norris Redshift Survey**, which is based on two independent redshift surveys of faint field galaxies. The coverage of both surveys is about 20 deg^2 and contains 835 galaxies down to R$\leq$21. The correlation length is $3.7h^{-1}$Mpc with γ=1.77 in redshift-space at a median redshift z_{med}=0.3 (Small et al. 1999).

A radio all-sky sample of ~600 galaxies having flux density S>0.5 Jy at 1.4 GHz and redshifts 0.01<z<0.1 was assembled by Peacock and Nicholson (1991). The two-point correlation function was found to have the form: $\xi(r) = (r/11)^{-1.8}$.

Radio galaxy clustering at low-redshifts was explored in a recent work by Lacy (2000), who selected 29 radio galaxies in the range 0.19<z<0.45 from a contiguous 40 deg^2 area of the sky. The clustering signal of $r_0 = 17h^{-1}$Mpc arose.

As a *conclusion*, galaxies without any signs of nuclear activity cluster obeying a two-point correlation power-law with r_0 =4-6h^{-1}Mpc and $\gamma \approx$1.8, whereas radio galaxies show a much stronger clustering signal.

1.5.2 Clustering of Clusters of Galaxies

As the largest gravitationally bound objects in the Universe, clusters of galaxies are important tracers of high-peak density fluctuations in the network of visible matter. Applying the two-point correlation function method it turned out that their clustering properties are well-fitted by a power-law with $\gamma \approx 2$ and r_0=15-25h^{-1}Mpc, which is a factor 3-5 higher than what is found for galaxies.

A recent analysis of 449 X-ray selected clusters within the scope of the ROSAT-ESO Flux Limited X-ray (REFLEX) Galaxy Cluster Survey showed a correlation r_0=18.8±0.9h^{-1}Mpc on scales 4-40h^{-1}Mpc at redshifts z≤0.3 (Collins et al. 2000). The spatial two-point correlation function of 364 clusters of galaxies selected from the APM Galaxy Survey gave r_0=14.3±2.35h^{-1}Mpc (Dalton et al. 1994), which marks a lower limit of the clustering strength for clusters of galaxies. The upper limit is found to be $r_0 \approx 25h^{-1}$Mpc, measured for rich clusters of galaxies (Bahcall & Soneira 1983). There is striking evidence for the amplitude of cluster correlation function to be dependent on the cluster richness: richer clusters[6] (R≥2) showing much stronger correlations than poorer (R=1) clusters (Postman, Geller & Huchra 1986).

A more loose agglomeration of extragalactic sources in comparison to clusters of galaxies are groups of galaxies including a few tens of galaxies. The combined sample of CfA2 and Southern Sky Redshift Survey 2 gave 885 groups of galaxies, which are significantly more clustered than galaxies by a factor 1.64±0.16 (Girardi, Boschin & da Costa 2000). A volume-limited (distance-limit 78h^{-1}Mpc) sample of 139 groups shows a clustering in redshift-space matching a power-law correlation function with $r_0 = 8 \pm 1h^{-1}$Mpc (Girardi, Boschin & da Costa 2000).

1.5.3 Superclusters

Since the pioneering work of Shapley (1930), to whom the Shapley Supercluster is dedicated, superclusters of galaxies became known structures. Further investigations on large scales, which have mainly been performed with rich Abell clusters of galaxies, reported patterns with extensions of ∼300h^{-1}Mpc (Tully 1986,1987,1992). Bahcall & Soneira (1984) presented a catalogue of superclusters at z<0.1, where larger superclusters exhibit elongated sizes that exceed 100h^{-1}Mpc. Support for structures on scales of about 100h^{-1}Mpc was provided by a two dimensional measurement of the power spectrum in the LCRS (Landy et al. 1996). A strong peak on such scales appeared and the authors concluded that these structures are common features in the local Universe (z≤0.2). Some more superclusters were discovered, mostly named after the constellation where they reside in, such as Coma, Perseus, Hercules, having typical masses of 10^{15}-10^{16} $M_\odot$ (Oort 1983).

A group of researchers, known as the Seven Samurai, was able to detect a streaming motion above the cosmological expansion, that indicated a large over-

[6] R denotes the richness class

density labeled *Great Attractor* (Lynden-Bell et al. 1988). Another attractor-like structure, the *Great Wall* ($\sim 150h^{-1}$Mpc), was found in the CfA Redshift Survey (Geller & Huchra 1989).

The most extended analysis of superclusters and their incorporation in the structure network was published in a series of four papers, named *The Supercluster-Void Network I-IV* (Einasto et al. 1997c, 1997a, 1997b, and Jaaniste et al. 1998). The goal of their study was to explore the three dimensional distribution of superclusters and voids based on a catalogue of rich Abell clusters of galaxies at z$\leq$0.12. The sample comprised 220 superclusters, of which 90 were new discoveries. They showed that the supercluster void network shows regular patterns on scales $\approx 120h^{-1}$Mpc, where rich superclusters reside in chains and walls. The clustering properties of clusters in rich superclusters are by far different to clusters located in poor superclusters. The correlation lengths are $r_0 \approx 45h^{-1}$Mpc for the former ones and $r_0 \approx 17h^{-1}$Mpc for the latter. Moreover, an oscillating correlation function with decaying amplitude was found. Its minimum can be explained as the mean separation between centers of superclusters and voids, whereas the secondary maximum corresponds to the distance between superclusters across voids. The last work of this series was addressed to the shape and orientation of superclusters. Superclusters were found to be flattened and triaxial objects as not even one supercluster showed a spherical shape. The spatial orientation of superclusters, as determined from their axes, is random. No preferable orientation with respect to the line of sight, the alignment of neighboring superclusters or the surrounding large-scale structures was found.

Due to the small number of known superclusters no two-point correlation function has been calculated so far.

1.6 Large-scale structures at high-redshifts

The most distant extragalactic sources increase the available volume for any kind of studies, therefore, hunting for new record holders in the redshift domain is a popular business. Even if the current record holder is a galaxy at z=6.68 (Chen, Lanzetta and Pascarelle 1999), AGNs remain the most luminous objects known in the Universe. Since the discovery of the first AGN with z>4 in 1987 (Warren et al. 1987), more than 100 of such objects have been found. The border of redshift 5 has been recently crossed by some galaxies at: z=5.34 (Dey et al. 1998 and (a galaxy pair) Spinrad et al. 1998), z=5.60 (Weyman et al. 1998), z=5.19 (van Breugel et al. 1999), and z=5.74 (Hu, McMahon, and Cowie 1999). This is probably just a short and incomplete list of the actual most distant known objects in the Universe.

A method used for compiling high-redshift samples of galaxies has been the *Lyman break technique*, where the break in the spectrum at 912 Å in the rest frame is due to photoelectric absorption. The feature is so strong that samples of **Lyman-break galaxies (LBGs)** can be assembled easily in the redshift range 2.7$\leq$z$\leq$3.4. A sample of 871 LBGs at a median redshift $z_{median} = 3.04$

have a clustering correlation length $r_0 = 2.1h^{-1}Mpc$ (Giavalisco et al. 1998), which is comparable to that of present-day spirals. This result was derived from the angular correlation function through the Limber transformation, since N(z) of LBGs is well known. Another clustering investigation of LBGs (Adelberger et al. 1998) found a correlation length of $\approx 4h^{-1}$Mpc comparable to local galaxy samples and even stronger than intermediate redshift samples. These results are in good agreement with clustering properties of dark matter halos resulting from N-body simulations or analytic techniques. Hence, LBGs can be associated with dark matter halos with masses of the order of $10^{12}M_{\odot}$ (Steidel et al. 1998). Furthermore, the strong spikes of LBGs, which were found in the redshift histogram, have been interpreted as progenitors of present-day rich clusters of galaxies.

Chapter 2

ROSAC

Modern times are influenced more and more by marketing aspects: how can a product or project be sold in the most impressive and effective way? In the case of a project it is indispensable to commit oneself to an abbreviation of the entire project, which is substantially more than explaining the project again and again. A new project has been called into launch: *ROSAC* (A ROSAT based Search for AGN Clusters).

2.1 Definition: what is ROSAC

The ROSAC project[1] has been founded by D. Engels and F. Tesch in 1997. It aims at studying the large-scale structures of the Universe traced by AGNs, that were selected by the ROSAT satellite in the soft X-ray range (0.1-2.4 keV, 100-5 Å). Unlike many other works in the field of large-scale structures this project deals with low-redshift, chiefly $z<0.5$, AGNs. Thus ROSAC does not belong to the 'scientific mainstream', that nowadays is clearly focused on high-redshift projects. The scientific necessity of such a project is outlined in chapter 1. Recall that there were just two other projects analyzing large-scale structures with X-ray selected AGNs before. Additionally, these investigations (Boyle & Mo 1993 and Carrera et al. 1998) found only weak clustering signals using the 2-point-correlation function. For an understanding of the evolution of clustering properties low-redshift studies are needed urgently, while examinations of AGN samples at higher redshifts ($z>1$) are more numerous. These high-redshift samples exhibit a decline of the clustering amplitude towards smaller redshifts (down to $z\approx1$). However, this trend is by no means expected for even lower redshifts, if the biasing of AGNs does not strongly differ between the low- and high-redshift regime. Then dark matter N-body simulations have shown that the amplitude of the halo correlation function increases towards lower redshift after reaching its minimum at $z\sim1$-2 (Bagla 1998 and Brainerd &Villumsen 1994). Observational evidence for such an augmentation of the AGN clustering

[1] This project is financially supported by the Deutsche Forschungsgemeinschaft since the 1st of October 1997.

amplitude was provided by Sabbey et al. (2000), who found an unprecedented strength of clustering at low-redshifts, which is in contradiction to all anaylses ever performed in the local Universe, but fits perfectly well to CDM N-body simulations. On much larger scales, $\sim 100h^{-1}$Mpc, some groups of AGNs were serendipitously discovered, most of them have redshift larger than 1. These *superstructures* have been claimed to be the progenitors of *Great Attractors* in the local Universe (Komberg et al. 1994). If this is correct, such structures should be found in low-redshift ($0.1<z<0.5$) AGN samples as well. Both of the quoted topics ((1) clustering properties and (2) search for AGN groups) are targeted in the ROSAC project. Moreover, the ROSAC project will yield a well-defined AGN sample that can be used to carry out further investigations besides the clustering studies. A first attempt was made by R. Keil (diploma thesis, 2000), who explored X-ray selected Narrow-line Seyfert 1 galaxies from ROSAC and other X-ray projects (also Engels & Keil 2000).

In the upshot, the bottom line is that we do not know much about the cosmological evolution and formation of AGNs in general, and even less of X-ray selected ones. It becomes more and more clear that a real understanding of the formation of extragalactic objects and their evolutionary processes are heavily linked to the evolution of the density field, the background cosmology, and, of course, the formation and evolution of galaxies.

The ROSAC project is based on the ROSAT All-Sky Survey (RASS, Voges et al. 1999) conducted shortly after the launch of ROSAT from July 1990 to February 1991, its total survey exposure time amounts to 119.36 days. The RASS is the first All-Sky Survey in X-rays which was carried out with an imaging telescope increasing the sensitivity and source location accuracy. Former X-ray catalogues used collimated counter surveys, such as UHURU, HEAO-1 and others. The Position Sensitive Proportional Counter (PSPC) used for the RASS was optimized for the detection of point sources (Pfeffermann et al. 1988) providing the best available catalogue of soft X-ray sources. The first processing of the RASS was performed by taking into account strips of $2^\circ \times 360^\circ$ resulting in about 50,000 sources, whereas a second analysis with a detection likelihood reduced to ≥ 7 gave about 145,000 sources almost three times more. The main difference of the RASS-I and RASS-II data processing is that the overlap by at least 0.23 degrees of two neighboring strips was considered, which led to larger exposure times and problems of the source detection at the field boundaries were overcome.

Unlike recent X-ray missions, such as the **Chandra X-Ray Observatory**, (formerly known as Advanced X-ray Astrophysics Facilities (AXAF) and named in honor of S. Chandrasekhar), which is furnished with the Advanced CCD Imaging Spectrometer (ACIS) and the **X-ray Multi-Mirror satellite** (XMM) that carries the Reflection Grating Spectrometer (RGS), the X-ray information of an object from ROSAT alone is not enough to make a convincing classification. it just has served as a pointer on objects. Chandra and XMM are equipped with spectrographs in order to unveil directly the spectral fingerprint of the source without any help or follow-up spectroscopy in other wavelengths. For the pur-

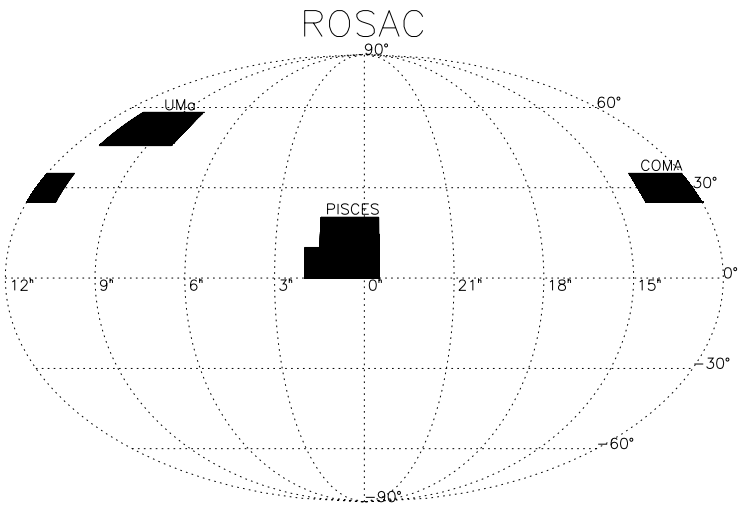

Figure 2.1: The initially defined areas in the ROSAC project, filled areas mark the selection made in the constellation Ursa Major, Coma, and Pisces on a full-sky Mollweide projection.

poses of the ROSAC project further information from other wavelengths was needed, especially the well-known optical wavelength range turned out to be an essential means for the classification of objects. The Hamburg Quasar Survey (HQS, Hagen et al. 1995), which is a wide-angle objective prism survey in the northern sky, provides the required optical information for the identification of soft X-ray selected AGNs from the RASS. Hence, observations were performed at the Hamburg Schmidt telescope, that resides on the Calar Alto (Spain) since 1980. The survey plates having a size of 24×24 cm^2, which covers a projected area of 5.5× 5.5 deg^2 on the sky, record spectra in the wavelength range between 3400 to 5400 Å. Typical exposure times were 60 minutes per plate achieving a maximal magnitude of B $\approx$ 18.5. However, the limiting magnitudes differ from plate to plate due to their quality and the observing conditions. Saturation is responsible for an upper magnitude limit of B $\approx$ 12 - 14. A 1.7° prism was used giving a dispersion of 1390 Å/mm at H_γ. Under good seeing conditions a spectral resolution of 45 Å at H_γ can be reached. After observations the plates were digitized with a PDS microdensitometer at the Hamburg Observatory. Depending on the chosen scan mode the density spectra consist of about 15 (low resolution scan) or 150 pixels (high resolution scan). Photometric sequences from Guide Star Photometric Catalogue (Lasker et al. 1988) were taken to calibrate the digitized spectral plates in the Johnson B-band (λ_{eff}=4400Å). Next to each prism plate a direct plate was taken as well. These plates were exposed for about 45 minutes reaching a deeper plate limit of B $\approx$ 20.

For the identification process of RASS sources an error circle with a radius of $40''$ was adopted for each source. An enlargement of the error circle of $2.3''$ was added due to the positional error of the spectra in the direction of dispersion leading to an ellipse. All optical counterparts within the error ellipse were taken

and the digitized objective prism spectra were considered in order to classify the RASS sources (Bade et al. 1998).

Since the ROSAC project is restricted to a lifetime of about three years, which corresponds to the typical duration of a PhD thesis, attention had to be drawn to a few chosen areas on the northern hemisphere, although an All-Sky Survey, of course, would be wishful thinking. The initial strategy was to carry out follow-up observations in three regions located in the constellation *Ursa Major (UMa)*, *Coma Berenices (Coma)*, and *Pisces* (s. fig 2.1). The choice of these regions enables observations throughout the entire year. Due to the fact that the UMa region as well as the COMA region can be reached for observations in the first half of the year, the Coma region was considered as backup only. The strategy in the Pisces region, which can be observed in the second part of the year, was dictated by the existence of a known group of AGNs (Tesch & Engels 2000) in such a manner that AGNs candidates close to the group were observed first. The areas of the ROSAC project are outlined in the following table:

Constellation	α_{2000}	δ_{2000}	$\sigma[\mathrm{deg}^2]$
UMa	8^h-11^h	45°-58°	363.40
COMA	11^h-14^h	25°-35°	389.22
PISCES	23^h30-2^h	0°-10°	373.11
PISCES	23^h30-1^h30^m	10°-20°	289.41

Table 2.1: *The boundaries of the ROSAC areas are given by α and δ comprising the surface σ. The regions in COMA and UMa extend both over 3 hours in right ascension, whereas the PISCES region is defined by two adjacent areas totally covering 662.52 deg^2.*

The next step was to think about a feasible strategy pertaining the optical follow-up observations of AGN candidates. The salient points were (1) concentration on telescopes of the 2m class, where the number of applications is decreasing with time due to the construction of larger telescopes (e.g. Keck, VLT) and (2) to convince other scientists for a collaboration, having in mind that these connections could open additional observing opportunities. The first collaboration was found rapidly; J. Wei and Prof. J. Hu from the Beijing Astrophysical Observatory (BAO) showed immediate interest in ROSAC. A second collaboration was made with C. Ledoux (ESO) and D. Valls-Gabaud (OMP Toulouse), and A. Ugryumov (SAO) joined as a further collaborator. All collaborations entailed the possibility of writing new proposals for observing time at the 2.16m telescope in Xinglong, at the 1.93m telescope at the Observatoire Haute de Provence (OHP), and at the Russian 6m telescope. Moreover, applications were made at the 2.2m telescope on Calar Alto. Apart from the Russian 6m telescope proposals all proposals had a successful issue. For a complete list of applications see table 2.2.

After three years of ROSAC, 13 applications for follow-up spectroscopy of AGN candidates were submitted to the committees of 6 different telescopes. The

ratio of approved to refused proposals is 8:4. 4 proposals were accepted at BAO and OHP (2 and 2, respectively), and the remaining four at Calar Alto. The number of observing nights summing up all approved proposals was 79, in which the nature of 366 AGNs could be revealed, amounting to about 4.6 AGNs per approved night. Admittedly, this is a rather disappointing low number of AGNs, but one should consider that only 50-60% of the entire 79 nights were suitable for observations and that the confirmation rate of the AGN candidates is about 82%, which makes our observing output somewhat more acceptable. A detailed output of all observing runs is presented for the individual telescopes in table 2.3

Year	Period	Nights	Telescope	Project	A/R	AGNs
1997	27.11-01.12	4	Calar Alto 2.2m	ROSAC	X	25
1998	Spring	3	SAO 6m	ROSAC	-	
	23.01-03.02	11	BAO 2.16m	ROSAC	X	63
	24.03-26.03	3	BAO 2.16m	ROSAC		0
	17.04-19.04	3	BAO 2.16m	ROSAC		0
	20.04-28.04	9	OHP 1.93m	ROSAC	X	39
	Fall	6	SAO 6m	ROSAC	-	
	13.09-16.09	4	Calar Alto 2.2m	ROSAC	X	38
	23.10-25.10	3	BAO 2.16m	ROSAC		13
	13.11-15.11	3	BAO 2.16m	ROSAC		17
1999	19.01-21.01	3	BAO 2.16m	ROSAC	X	18
	16.03-26.03	10	OHP 1.93m	ROSAC	X	27
	Spring	4.5	ESO 3.6m/1.5mD	SCULPTOR	-	
	Spring	5	Mt. Hopkins 1.5m	bright AGNs	-	
	13.04-15.04	3	BAO 2.16m	ROSAC		0
	03.05-10.05	8	Calar Alto 2.2m	ROSAC	X	39
	14.09-16.09	3	BAO 2.16m	ROSAC		0
	Fall	6.5	ESO 3.6m/1.5mD	SCULPTOR	-	
	Fall	4	2dF	SCULPTOR	-	
	Fall	3	CFHT 3.6m	ROSAC	-	
	Fall	2	Kitt Peak 4m	ROSAC	-	
	05.11-11.11	7	Calar Alto 2.2m	ROSAC	X	43
2000	14.03-18.03	5	Calar Alto 2.2m	ROSAC	X	34

Table 2.2: *The column A/R denotes approved (X) or refused (-) proposals. At BAO applications always cover a whole year, thus marks are only set in the column A/R for one granted application per year. The SCULPTOR project was planned as a collaboration with M. Graham and R. Clowes to study the Group of AGNs, which was first discovered by Webster (1982) located in the Sculptor constellation. Another project with M. Elvis and A. Dobrzycki as collaborators aimed at enlarging a sample of bright ($B \leq 17.5$) AGNs in order to find further clues about the Quasar Eigenvectors*

Finally, it should be mentioned that the ROSAC project has never reached its formerly defined goals due to the incompleteness in at least two of the three selected areas under study (details are presented in chapter 3). When the ROSAC project was designed, one of the basic assumptions was that the difference between RASS-I and RASS-II data was of the order of 10%, which means that about 10% more sources were expected to be found in the second RASS data processing. With release of the RASS-II data (in the mid-stage of the ROSAC project) an average increase, independently on the position on the sky, of about 50% of objects from RASS-I to RASS-II had been recognized, that dropped the completeness of the three samples dramatically. A crude estimation (s. chapter 3) shows that a prolongation of at least 2-3 years are required (for follow-up spectroscopy) to accomplish this project according to its initial goals. However, the upcoming big redshift surveys like the Sloan Digital Sky Survey (SDSS) and the 2-degree-Field QSO Redshift Survey (2QZ) will comprise of thousands of AGNs, urging the ROSAC project to be finished soon. Especially, the SDSS, that covers a large area of the RASS at the northern hemisphere, put pressure on ROSAC due to overlapping areas and sources. Therefore, the decision to accomplish at least one of the three ROSAC samples in the initially established schedule was made. At that time the UMa area was advanced most, so that the last observing run was solely used for sources in UMa.

	AGNs	Galaxies	Stars	Nights
B & B	5			
SAO	5			
BAO	111	11	15	32
OHP	66	3	12	19
Calar Alto	179	11	27	28
Σ	366	25	54	79

Table 2.3: *The observing output per telescope. Thanks to our colleagues V. Beckmann, N. Bade (B & B), and A. Urgyumov, who spend some minutes of their precious observing time at the 3.5m telescope at Calar Alto and at SAO, respectively, in order to unveil the AGN nature of another 10 objects. The numerous unclassified objects without any particular features in their spectra are not listed here.*

Chapter 3

DATA

After the description of the ROSAC project in the previous chapter, a detailed overview is given here about the data set. The initial sample was provided by the RASS, therefore it is the X-ray band that will mainly attract our attention. First of all, optical follow-up observations had to be conducted in order to confirm the AGN nature of the candidates and to get a sample with a completeness high enough for clustering analyses. No examination of X-ray selected AGNs can be found in the literature having degrees of completeness that are smaller than 88%.

3.1 The determination of the final AGN sample

The follow-up spectroscopy was performed at 2m class telescopes (s. chapter 2) leading to the discovery of 366 new AGNs. In addition to own observations, already known redshifts of AGNs that belong to our sample have been taken from published investigations and/or available catalogues, such as NASA Extragalactic Database (NED). The table 3.1 depicts the individual samples of the ROSAC project. The number of AGNs taken from the literature amounts to 308, 46% of all classified AGNs. The portion of own spectra is larger in the UMa area, since the last observing runs were mainly focused on these objects. A crude estimation of the degree of completeness for the PISCES area considering RASS-II data gives 357 new sources, which is the difference between RASS-I and RASS-II with a maximum likelihood ML $\geq$ 10. Assuming that 50% of them are AGN candidates, and taking into account our confirmation rate CR of 82% results in 144 new AGNs. For deriving the completeness in PISCES it has to be resorted to the numbers in table 3.1, where 222 known AGNs and 46 AGN candidates (45 with unknown redshifts + 1 BL Lac) are listed increasing the number of AGN candidates to 190 totally now. The completeness C is defined as

$$C = \frac{N_{AGN}}{N_{AGN} + CR \cdot (N_{\not z} + N_{\not f}) + N_{BL}}, \tag{3.1}$$

where N_{AGN} represents the number of classified AGNs, $N_{\not z}$ is for remaining AGN candidates, $N_{\not f}$ gives the number of objects without any features in their spectra,

Sample	N_{tot}	N_{AGN}	N_{rest}	$N_{\not z}$	$N_{\not f}$	N_{BL}	N_{div}	C
UMa	379	266	113	61	10	4	38	0.81
COMA	236	185	51	26	9	1	15	0.86
PISCES	307	222	85	45	11	1	28	0.83

Table 3.1: *The quoted numbers are only with respect to RASS-II in UMa, whereas COMA and PISCES refer to RASS-I.* N_{tot} *denotes the entirety of AGN candidates provided by the RASS and HQS.* N_{AGN} *represents the number of confirmed AGNs by own observations and the NED, and* N_{rest} *is just the difference between* N_{tot} *and* N_{AGN}*, consisting of* $N_{\not z}$ *(remaining AGN candidates),* $N_{\not f}$ *(featureless objects),* N_{BL} *(number of BL Lac objects without redshift), and* N_{div} *(diversity of non-AGN objects, such as normal galaxies, stars, and Cataclysmic Variables). The completeness C per sample is given by equation 3.1.*

and N_{BL} refers to BL Lacs (candidates) without redshift information. Using the mentioned relation (equation 3.1) for calculating C gives a completeness of 54%, which is inadequate for any study of clustering. Since the numbers for the COMA area are similar to that of PISCES this sample does neither reach a sufficient completeness for consideration here.

The COMA and PISCES areas provide about 340 new AGNs with respect to the RASS-II data, for which follow-up observations had to be done. In the UMa region another 61 AGN candidates remain without redshifts amounting to about 400 objects for the entire ROSAC project, which is even slightly higher as all observed objects within 3 years of ROSAC. The conclusion is that at least 2 more years of observations are required to reach the same completeness in COMA and PISCES as it exists in UMa now. But the needed observing time would be acquired much harder than before, since the committees, that decide about the allocation of observing time, are generally more sceptical about longterm projects without published results. Thus, the estimation of two more years of follow-up observations is rather optimistic.

The high completeness in the UMa area is the reason why the following investigations are addressed to the UMa sample solely. Minor revisions to the UMa sample statistics are necessary due to four objects. Three of them (an AGN, a star, and a still unclassified object) do not have an X-ray counterpart anymore, whereas these objects had a counterpart in the RASS-I processing. Conversely, the RASS-II data did not reveal any X-ray counterpart for unknown reasons. The fourth object, an AGN with z=0.948, was found with an X-ray flux, that lies below the flux limit (s. next chapter). All four objects were removed from the initial sample, resulting in a final sample of 375 AGN candidates. Likewise, the number of AGNs reduces to 264 and the number of the remaining AGN candidates is 60. However, the completeness (C=81%) for the UMa sample is not influenced by this revision.

The redshift distribution of the UMa AGN sample, having a median redshift z_{median}=0.331 and an average redshift $\bar{z}$=0.455, is shown in figure 3.1. The

largest measured redshift of the sample is 2.921 and the lowest one is 0.004. A portion of 69% of all AGNs populate the redshift range at z≤0.5 and still one third of the sample lies at z≤0.2.

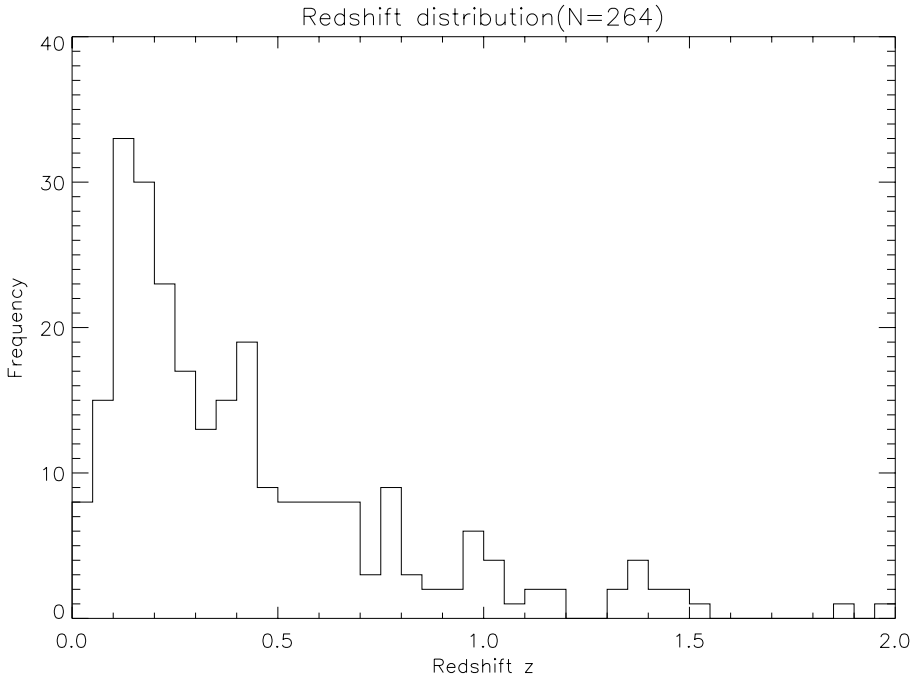

Figure 3.1: The redshift distribution of the UMa sample clearly peaks at low-redshifts in contrast to optically selected AGN samples. Three objects with z>2.0 are omitted.

3.2 X-ray information

Since soft X-ray photons are heavily absorbed by atomic hydrogen inside our galaxy, hydrogen column densities from radio observations had to be used in order to correct the X-ray flux. By means of the redshift information from optical spectra and the X-ray flux the X-ray luminosities were then calculated for a standard cosmology ($\Omega_m = 1.0, \Omega_\Lambda = 0$). Finally, flux limits for the generation of random samples were derived from exposure time and background maps provided by the ROSAT team.

3.2.1 Hydrogen column densities N_H from the Leiden-Dwingeloo Survey

Since decades radio astronomers have drawn attention to the 21-cm line of atomic hydrogen. The HI surveys are particularly important, because of the absorbing properties of neutral hydrogen when lying in the line-of-sight. Especially, X-ray photons suffer from the encounter with the abundantly existing

HI in the Milky Way, even though they are stronger absorbed by He, which is hardly present in the Milky Way.

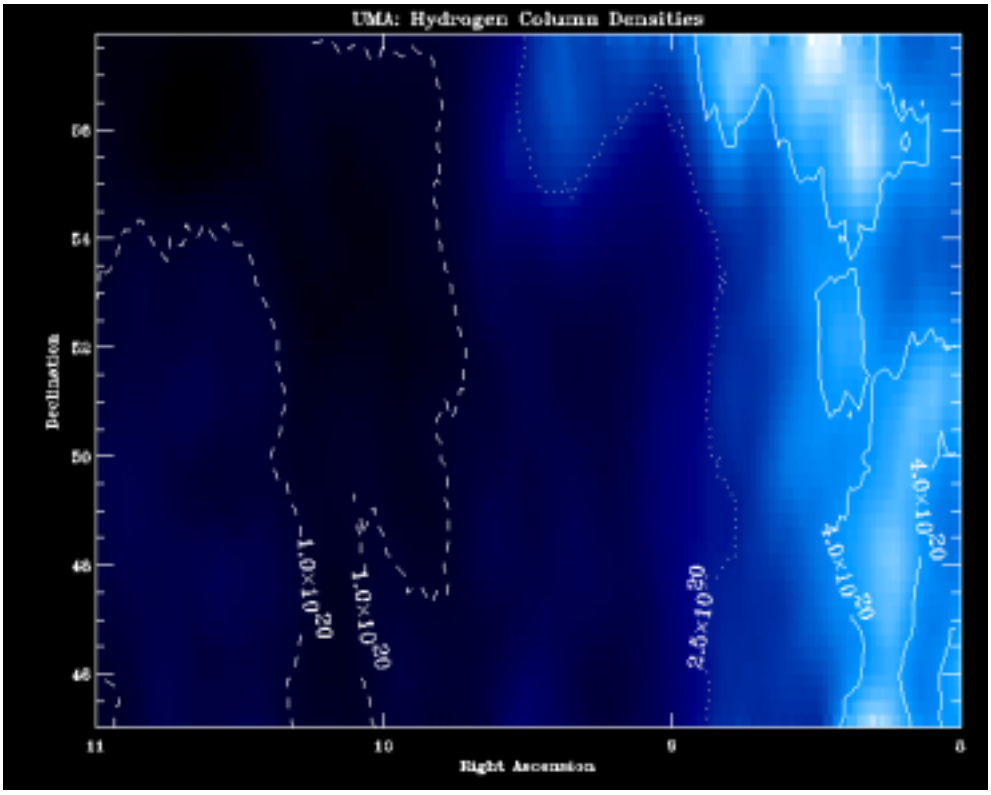

Figure 3.2: N_H in the UMa area is displayed, where right ascension (in hours) and declination (in degree) span the selected UMa region. Brighter color denotes higher hydrogen column densities as seen in the three plotted contours. The lowest column densities are clearly visible around the Lockman hole (10^h40^m, 56^d40^m), whereas the Milky Way with its much higher column densities comes up at the other end around 8^h.

An earlier survey, which was performed with a 20 foot horn reflector at the AT&T Bell Laboratories in Crawford Hill (Stark et al. 1992), was the commonly used catalogue for hydrogen column densities until recently. Nowadays the Leiden/Dwingeloo Survey offers a marvelous catalogue of atomic hydrogen emission, which can be used to calculate hydrogen column densities. Due to its better resolution and larger sky coverage older HI surveys have been replaced by the Leiden/Dwingeloo Survey. The entire sky above declination of -30 degrees, on a half degree grid, over a velocity range of 1,000 km/s at a resolution of 1 km/s is now available. The fits-files of the 206,668 radio spectra and sky maps in different velocity ranges can be downloaded from a CD that is enclosed to the *Atlas of Galactic Neutral Hydrogen* (Hartmann & Burton 1997). The integration over the radio spectra times a conversion factor (CF) provides the hydrogen column densities:

$$N_H = CF_H \cdot \int T_b \cdot dv. \tag{3.2}$$

T_b denotes the brightness temperature in degrees of Kelvin and *dv* refers to the velocities in km/s. Using a value of 0.18224 as conversion factor CF_H, the hydrogen column densities are given in $10^{19}\mathrm{cm}^{-2}$ (Hartmann & Burton 1997).

Before using this atlas few manipulations of the column densities had to be done, since contamination by galaxies led to systematically larger hydrogen column densities in certain regions of the sky. Therefore the spectra, where galaxies can be clearly seen, were selected and the contribution of the galaxy was subtracted. In seven cases the overlap of the galaxy radio emission and the interstellar medium component was so strong that a subtraction was not possible. Nevertheless, 55 spectra were obviously contaminated by galaxies.

For every AGN in the UMa sample a hydrogen column density can be calculated. All radio spectra within a radius of 1° around each AGN were taken and weighted by their distance from the AGN. A weighted average seems to be more plausible than an arithmetic average, since the closer the radio spectrum lies to the AGN the stronger the influence at the location of the AGN.

The smallest hydrogen column density in UMa of $\sim 4 \cdot 10^{19}\mathrm{cm}^2$ (table 3.2) at $10^h 40^m$ and $56^d 40^m$ is part of the *Lockman Hole* (Lockman, Jahoda & McCammon 1986), which is a region of extremely low hydrogen absorption. Towards the galactic plane the N_H values increase as expected, culminating at $8^h 32^m$ and $57^d 38^m$.

Sample	$N_{H_{max}}$	$N_{H_{min}}$
UMa	53.52	4.06
COMA	24.60	8.15
PISCES	72.29	15.76

Table 3.2: *Maxima and minima of the hydrogen column densities in units of* $10^{19}\,cm^{-2}$ *in the different areas of ROSAC.*

3.2.2 ROSAT data

The most important quantity from the X-ray data set is the count rate in units of counts per second. The X-ray flux f_x is related to the count rate through a conversion factor

$$f_x = CF \cdot count\,rate \tag{3.3}$$

where

$$CF = \frac{\int_{E_1}^{E_2} E^{1-\Gamma} exp(-N_H \cdot \sigma(E))dE}{\int_{E_1}^{E_2} E^{-\Gamma} \cdot A(E)dE} \tag{3.4}$$

(Tananbaum et al. 1979). The interstellar photoelectric absorption $\sigma(E)$ in the Galaxy disturbs the X-ray photon on its way to the observer. Morrison & McCammon (1983) obtained an effective absorption cross-section for the interstellar medium (ISM) using available atomic cross-sections and cosmic abundances. The effective surface of the telescope A(E) (Trümper 1991) as a function of the

energy have to be added as further ingredient. The photon number index Γ is related to the spectral index α_x as $\Gamma=\alpha_x+1$. To make the results comparable to other investigations of X-ray AGNs a spectral index $\alpha_x=1$ was selected for the entire sample. From the physical point of view this does not make much sense, since some objects certainly do not follow a spectral power-law in the soft X-ray band and others have discordant values from 1! ROSAT's energy range is given by E_1=0.1keV and E_2=2.4keV. The hydrogen column density was taken as explained from the Leiden/Dwingeloo survey (fig. 3.2).

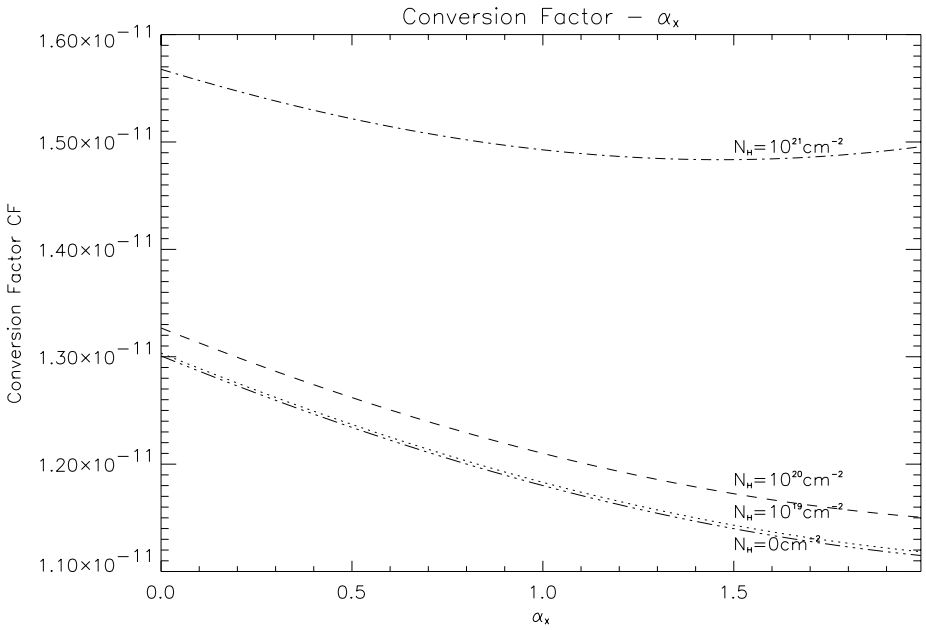

Figure 3.3: The Conversion factor as a function of the spectral index α_x for several hydrogen column densities, ranging from completely unabsorbed X-ray photons (N_H=0) to $N_H=10^{21}cm^{-2}$.

Figure 3.3 illustrates the dependencies of the conversion factor on the spectral index α_x. Indirectly, it is the measured X-ray flux that is influenced by the changes of CF and N_H. In general, the larger the hydrogen column density the larger the conversion factor is. This means that two sources with similar count rates but different N_H absorption also differ in their X-ray fluxes, so that the more absorbed source has a larger X-ray flux. For low hydrogen column densities (e.g. $N_H \leq 10^{20}cm^2$), the conversion factor decreases monotonically with increasing spectral index.

The X-ray flux for the UMa sample is easily derived from equation 3.3, for the ROSAT count rates, the conversion factor, and a spectral index α_X=1.0. The next step is to include the redshift in order to calculate the X-ray luminosity as

$$L_x = 4\pi f_x d_L^2 (1+z)^{\alpha_x - 1} \tag{3.5}$$

(Peterson 1997), where d_L is the luminosity distance (s. Appendix A). The factor $(1+z)^{\alpha_x-1}$, named k-correction, is equal to unity for the applied spectral

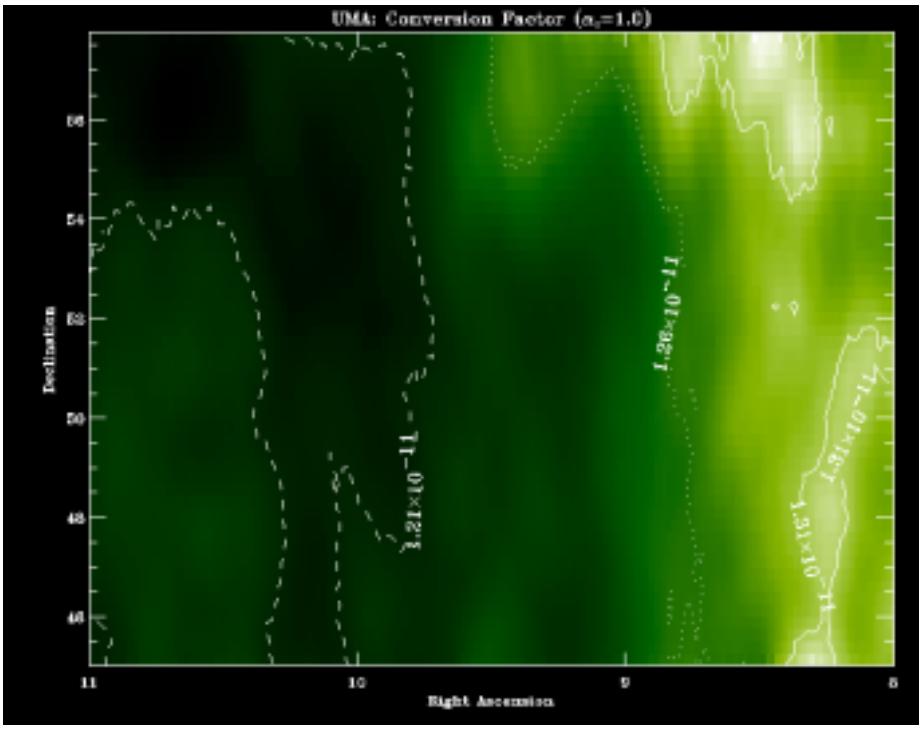

Figure 3.4: The conversion factor CF for the UMa sample derived from hydrogen column densities of the Leiden/Dwingeloo Survey. Strong features of the conversion factor can be refind in the map of hydrogen column densities (3.2). The largest value is CF=$1.344{\cdot}10^{-11}$ and the lowest one is $1.192{\cdot}10^{-11}$.

index (α_x=1).

One major concern for the generation of random samples, which are required for the clustering analysis (s. chapter 4), is how to get flux limits from the X-ray data. It is obvious that the exposure time t_{exp} influences their calculation as well as the chosen maximum likelihood, ML. The smaller ML the more objects are considered in the ROSAT source detection algorithm and the lower is the flux limit. But the number of misidentifications among the X-ray sources is also increasing with decreasing maximum likelihood. Therefore, a rather conservative value of ML=10 was selected. For each of the three areas of ROSAC, exposure time maps and background maps have been made available by the ROSAT team with respect to the RASS-II data processing. These maps have a resolution of $0.25\times0.25\mathrm{deg}^2$, which is higher than the one of the Leiden/Dwingeloo Survey for determining hydrogen column densities. The center of each of the $0.25\times0.25\mathrm{deg}^2$ fields was chosen to calculate the hydrogen column density as described before. For a given position in the sky, the *minimum counts for detection* $C(\alpha,\delta)$ are obtained from

$$\sqrt{ML} \sim \frac{C(\alpha,\delta)}{\sqrt{C(\alpha,\delta) + b \cdot t_{exp}}} \tag{3.6}$$

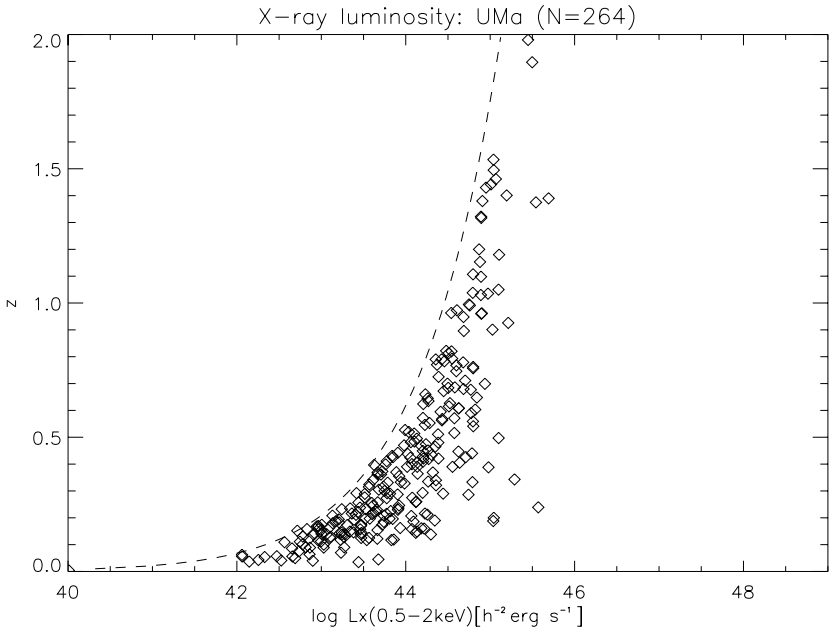

Figure 3.5: The soft X-ray luminosities of the AGNs in the UMa sample with their corresponding redshifts are shown as diamonds. The dashed line represents the X-ray luminosity based on the lowest X-ray flux limit $f_{x_{limit}} = 1.941 \cdot 10^{-13} ergcm^{-2}s^{-1}$.

or

$$C(\alpha,\delta) = 0.5(ML + \sqrt{ML^2 + 4 \cdot b \cdot t_{exp} \cdot ML}), \tag{3.7}$$

where t_{exp} denotes the RASS exposure time and b the background count rates, both as function of the position (α, δ). The minimum counts for detection divided by the exposure time gives the minimum count rates and the conversion from count rates to fluxes, here the flux limit, is achieved by multiplying the count rates by the conversion factor as a function of the hydrogen column densities:

$$f_{x_{limit}}(\alpha,\delta) = CF(N_H(\alpha,\delta)) \cdot \frac{C(\alpha,\delta)}{t_{exp}(\alpha,\delta)}. \tag{3.8}$$

The flux limits were derived for a spectral index α_x=1.0 in order to make them comparable to the other investigations.

3.3 Optical information

Next to the X-ray data, that define the initial sample, optical data for the UMa sample are available too. From the digitized Hamburg objective prism plates apparent magnitudes m_B in the Johnson b-band, since this filter is fully covered by the spectra, have been derived (Engels, Cordis & Köhler 1994). An internal characteristic curve was calibrated by the means of photometric sequences from the Guide Star Photometric Catalogue I for the bright end (B<16) and own

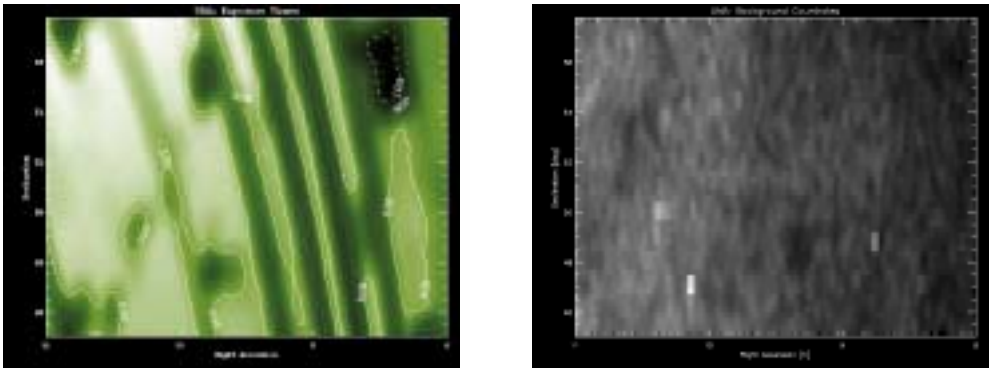

Figure 3.6: The RASS exposure time map in units of seconds for the UMa region is shown in the left panel with an upper and lower limit of 657.97s and 19.35s. The less spectacular panel on the right presents the background count rates.

sequences obtained at the 1.2m telescope on Calar Alto were used for the faint end (15<B<20). The accuracy of the brightness calibration turned out to be 0.3 down to B≈18.5 and, of course, larger for fainter magnitudes, while approaching the plate limit. However, the estimation of an error for fainter magntiudes is insecure, but at least 0.5. In a recent determination of the B-magnitudes in the UMa region, the brightness calibration of the individual plates was attuned to its neighboring plates in contrast to the former work, where the plate itself was only taken into account regardless on its neighbors.

By means of the B-magnitudes the optical absolute magnitude M_B can be calculated as:

$$M_B = m_B - A_B(\alpha,\delta) - K(z) - 5 \cdot log d_L - 25 \tag{3.9}$$

where d_L is the luminosity distance (s. appendix A) and K(z) is the K-correction for a power-law spectral energy distribution $F_\nu \sim \nu^{-\alpha}$, which approximates the AGN continuum fairly well,

$$K(z) = 2.5(\alpha_{opt} - 1) log(1+z). \tag{3.10}$$

Flatter spectra (α_{opt} <1) yield a negative K-correction, since such sources have a bluer spectra and the brighter part is brought into the observed waveband by the Doppler shift. The foreground extinction $A_B(\alpha,\delta)$ is a function of the position (α,δ) at the hemisphere due to its dependence on the hydrogen column densities N_H. The color excess is given by E(B-V)=A_B-A_V. Seaton (1979) found R=A_V/E(B-V)≈3.2, so that A_B=(1+R)E(B-V) and with E(B-V)=$N_H/4.8{\cdot}10^{21}$ the foreground extinction is simply

$$A_B(\alpha,\delta) \approx 4.2 \frac{N_H[cm^{-2}]}{4.8 \cdot 10^{21}}. \tag{3.11}$$

The completeness of the UMa sample can be improved by introducing a second limit to the initial X-ray conditions in the Optical. Therefore a cut in the

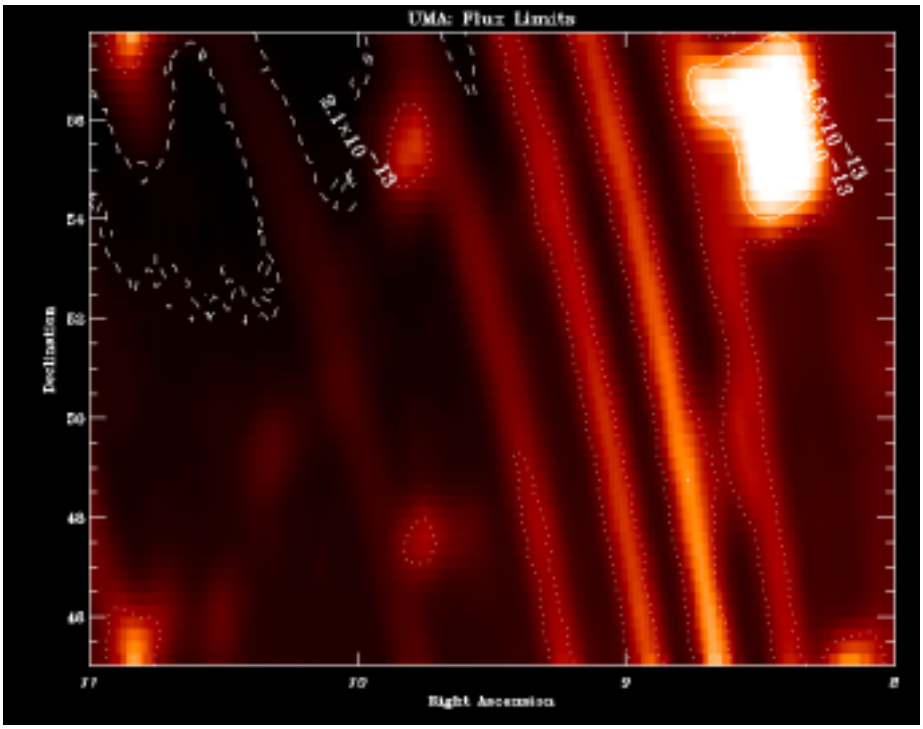

Figure 3.7: From equation 3.7 derived X-ray flux limits $f_{x_{limit}}$ for the UMa sample. Brighter areas denote higher flux limits, where the extrema are $1.94 \cdot 10^{-13} ergcm^{-2}s^{-1}$ and $6.82 \cdot 10^{-12} ergcm^{-2}s^{-1}$. The features are chiefly drawn from the exposure times.

distribution of apparent B-magnitudes at B<19.0 (figure 3.8) was applied. The selection of this *magnitude cut* is simply explained by the fact, that for brighter B-magnitudes more and more AGNs would be excluded from the *subsample* and on the other hand this magnitude represents the upper reliable determination of B-magnitude. Taking both arguments into account, B<19.0 is an optimized cut. Among the AGN candidates (N_{γ}=60) are 55 objects with B-magnitudes fainter or equal to 19.0, so that they have to be erased for the calculation of the new completeness of the subsample. The number of featureless objects (N_{f}=10) and BL Lacs (N_{BL}=4) remain unchanged, while 42 faint AGNs with known redshifts are omitted too. Finally, 222 AGNs are facing 15 AGN candidates, whereby the confirmation rate (∼82%) has to be applied yet, leading to a much better completeness C=222/(222+0.82·15+4)≈93%.

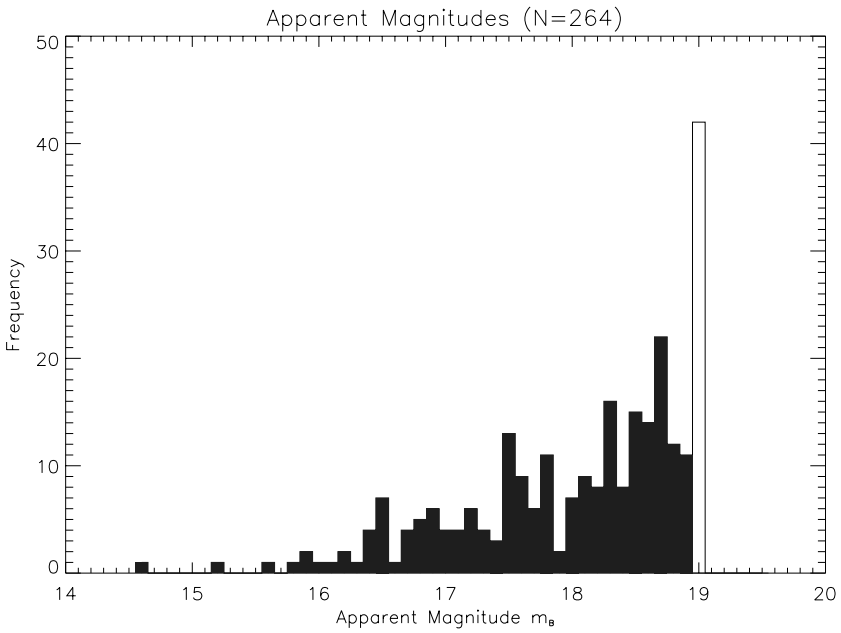

Figure 3.8: The apparent magnitudes in the Johnson B-filter for the UMa sample are presented including all bars of the histogram. The sum over the filled bars represent a subsample of N=223 with B<19.0.

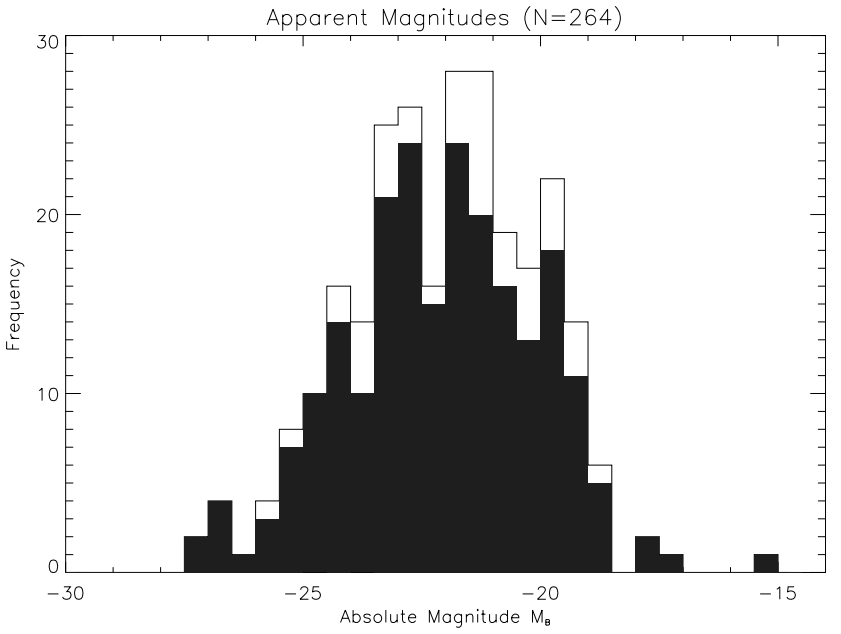

Figure 3.9: In conjunction with figure 3.8 the corresponding optical absolute magnitudes M_B (according to equation 3.8) are shown for the entire UMa sample (all bars) and a subsample with B<19.0 (filled bars).

Chapter 4

Data analysis

4.1 AGN selection function

The common property of available soft X-ray redshift surveys is the decrease of the number density of objects with redshift. This can be expressed in terms of a selection function (Strauss et al. 1991, Yahil et al. 1991 and Strauss & Willick 1995). The AGN selection function is based on the AGN luminosity function, which is the number of AGNs per unit comoving volume per unit interval of luminosity. This chapter deals with the derivation of the AGN selection function, that is needed for the generation of random samples.

4.1.1 V_e/V_a test

An early test devised by Schmidt (1968), called $V/V_{\rm max}$ *test*, is a means for studying the evolution of objects. A superior but related method to the $V/V_{\rm max}$ *test* was introduced by Avni & Bahcall (1980). The new variable, $V_{\rm e}/V_{\rm a}$, is the ratio of the volume enclosed by an object to the volume available to the same object. The enclosed volume of an object is simply given by its redshift z and formulae (A.10). For the available volume of an object its maximal redshift $z_{\rm max}$ has to be calculated, which the object could have while reaching the flux limit of the sample. The combination of ($L_{\rm x}$, $f_{\rm x_{lim}}$) is needed for deriving $z_{\rm max}$, and the comoving volume with respect to $z_{\rm max}$ determines the available volume. If the luminosity function Φ(L,z) is independent of z, the number of objects, N, of a given luminosity, L, per unit comoving volume is the same over the entire redshift range. Hence, $V_{\rm e}/V_{\rm a}$ is uniformly distributed in the interval [0,1] and the expected mean is $<V_{\rm e}/V_{\rm a}>$=0.5 with a dispersion σ^2=1/(12N). In an expanding Universe deviations from 0.5 as mean value for $V_{\rm e}/V_{\rm a}$ indicate that the comoving density of objects evolves.

The $V_{\rm e}/V_{\rm a}$ test was applied to two samples in UMa: (a) X-ray selected sample and (b) optically complete sample (B<19.0). The treatment of a sample, that has been constructed by more than one selection criteria (e.g. sample (b), where an optical flux limit is added an initially X-ray selected sample), is also described

z range	N	V_e/V_a	σ_{V_e/V_a}	N	V_e/V_a	σ_{V_e/V_a}
0.0-0.3	125	0.469	0.03	110	0.445	0.03
0.3-0.7	88	0.485	0.03	74	0.508	0.03
0.7-1.25	35	0.501	0.05	26	0.513	0.06
1.25-2.0	13	0.698	0.08	11	0.714	0.09
all	264	0.462	0.02	222	0.433	0.02

Table 4.1: *V_e/V_a is shown for both samples in UMa, the proper or real sample comprising 264 AGNs and one with B-magnitudes smaller than 19.0 (N=222). Both samples were divided in four redshift bins.*

by Avni & Bahcall (1980). Here z_{max} has to be chosen from the following relation: $z_{max}=\min(z_{max}^{X-ray}, z_{max}^{optical})$, then the V_e/V_a test is applied as before. The results, presented in table 4.1, are consistent with a value $V_e/V_a=0.5$ to redshifts as high as 1.25, which is expected for a uniformly distributed, complete, and unbiased sample. At higher redshifts V_e/V_a is significantly larger than 0.5 indicating evolution of AGNs.

4.1.2 AGN X-ray luminosity function

Another way of studying the distribution of sources as a function of redshift is the *luminosity function* $\Phi(L_x, z)$, which is defined as the number of AGNs of a given luminosity per unit comoving volume. Usually the evolution of the luminosity function is expressed in three different ways: *pure density evolution (PDE)*, *pure luminosity evolution (PLE)*, and *luminosity-dependent density evolution (LDDE)*, where the starting point is always the *local luminosity function* $\Phi(L_x, z = 0)$, which is multiplied by an evolution function e(z) corresponding to the favored evolution scenario. In a PDE scenario (Schmidt 1968) all objects have the same luminosity independently of their redshifts and it is their density that varies with z. PLE (Mathez 1976) suggests that the comoving density is the same but that luminous AGNs were more frequent in the past. Finally, LDDE (Schmidt & Green 1983) as the name indicates, suggests a density evolution that depends on the luminosity bins.

Numerous calculations of the X-ray luminosity function of X-ray selected AGN samples have been published (e.g. Maccacaro et al. 1991, Boyle et al. 1993, Boyle et al. 1995, Page et al. 1996, Boyle et al. 1997, Jones et al. 1997, Page et al. 1997, and Miyaji, Hasinger & Schmidt 2000). Attention is drawn here to the work of Miyaji, Hasinger & Schmidt (2000), who used data from 7 ROSAT surveys of various depth to investigate the evolution of the 0.5-2.0 keV soft X-ray luminosity function. Their combined sample consists of 691 AGNs having X-ray fluxes from $4.2{\cdot}10^{-11}$ to $1.7{\cdot}10^{-15}$ ergs^{-1}cm^{-2}. An analytical description of the X-ray luminosity in the overall redshift and luminosity range was found using Kolmogorov-Smirnov tests and Maximum-Likelihood fits, and the form of the LDDE model is well supported by the data in contrast to the classical

PLE and PDE models. Their analytical expression for the present-epoch (local) X-ray luminosity function is fitted by a double power-law:

$$\frac{d\Phi(L_x, z=0)}{dLogL_x} = \frac{A}{(L_x/L_*)^{\gamma 1} + (L_x/L_*)^{\gamma 2}}. \tag{4.1}$$

The evolution function for the PDE or PLE model is

$$e(z) = \begin{cases} (1+z)^{p1} & (z \le z_c) \\ e(z_c)[(1+z)/(1+z_c)]^{p2} & (z > z_c) \end{cases} \tag{4.2}$$

and for the preferred LDDE model

$$e(L_x, z) = \begin{cases} (1+z)^{max(0, p1-\alpha Log(L_a/L_x))} & (z \le z_c; L_x < L_a) \\ (1+z)^{p1} & (z \le z_c; L_x \ge L_a) \\ e(L_x, z_c)[(1+z)/(1+z_c)]^{p2} & (z > z_c) \end{cases} \tag{4.3}$$

where the parameters A, $\gamma 1$, $\gamma 2$, L_*, p1, p2, L_a, and z_c are model dependent (s. table 4.2).

Model	A	L_*	$\gamma 1$	$\gamma 2$	p1	p2	α	$LogL_a$	z_c
LDDE	$1.01{\cdot}10^{-6}$	3.00	0.75	2.25	5.1	0.0	1.7	44.1	1.57
PLE	$4.0{\cdot}10^{-6}$	1.33	0.60	2.34	3.0	0.3			1.42
PDE	$6.0{\cdot}10^{-7}$	4.32	0.74	2.28	4.6	0.6			1.60

Table 4.2: *The fitting parameters are derived for the standard cosmological model ($\Omega_m = 1, \Omega_\Lambda = 0$).*

The X-ray luminosity function evolves from the present-epoch towards higher redshifts via the evolution term:

$$\frac{d\Phi(L_x, z)}{dLogL_x} = \frac{d\Phi(L_x, z=0)}{dLogL_x} \cdot e(L_x, z), \tag{4.4}$$

where $e(L_x, z)$ cn be replaced by $e(z)$ depending on the model.

In practice, the luminosity function is often calculated using the accessible volume $\Sigma(1/V_a)$ estimator, which was used for the UMa sample as well. The X-ray luminosity function and its error in different redshift shells are

$$\frac{d\Phi}{dLogL_x} = \frac{1}{\Sigma_i V_a(L_{x_i}) \Delta LogL_x} \tag{4.5}$$

$$\sigma\left(\frac{d\Phi}{dLogL_x}\right) \approx \frac{1}{\sqrt{\Sigma_i V_a^2(L_{x_i})} \Delta LogL_x}. \tag{4.6}$$

For the UMa sample, AGNs with redshifts z<0.5 have been taken into account, since the number of objects decreases for larger redshifts, so that this part of the sample is unsuitable for clustering sudies. A comparison of the X-ray luminosity function in UMa with the LDDE and PDE model from Miyaji et

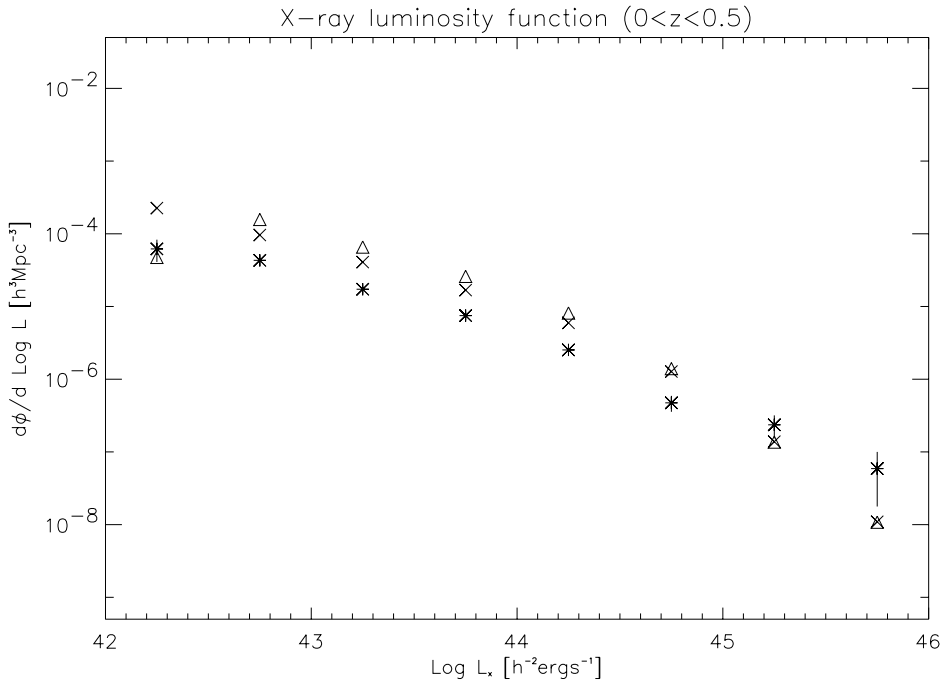

Figure 4.1: The X-ray luminosity function for 182 ROSAC AGNs in UMa is shown as stars with 1σ errors. The LDDE model (triangles) and the PDE model (crosses) slightly deviate between 42.5 and 45 in $\log L_x$ from the UMa sample, which can be explained by the incompleteness of the UMa sample.

al. is depicted in figure 4.1. In spite of the incompleteness of the order of 20% in the UMa sample its X-ray luminosity function fits well to the analytical description of Miyaji et al. at low redshifts. A much better fit can be expected from a complete UMa sample, as the deviations in different luminosity bins will be smaller or even vanish, and the luminosity function in the bins centred on 42.25, 44.75, 45.25, and 45.75, that harbor less than 10 objects, will be estimated more reliably. While Miyaji's LDDE model provides the best fit to the studied data (of 862 AGNs) and it appears that the complete UMa sample would also match well to this model, it reliably serves as selection function for the generation of random samples.

The number of AGNs as function of its redshift can be derived from the LDDE model of the X-ray luminosity function as follows (Miyaji, Hasinger & Schmidt 2000)

$$N(z) = \int_{L_{min}}^{L_{max}} \frac{d\Phi}{dLogL_x} d_a^2(z)(1+z)^3 c\frac{d\tau}{dz}(z) A(L_x/d_l), \qquad (4.7)$$

where $d\tau/dz$ is the look-back time, d_a the angular distance (s. Appendix A) and $A(L_x/d_l)$ is the available survey area as a function of the X-ray flux (Fig. 4.2). In order to get the correct units for N(z), the available survey area has to be taken as dimensionless, which means that it has to be divided by the surface of the whole UMa region (A_{UMa}=363.4 deg^2), so that its values span

the range from 0 to 1. The determination of N(z) has been restricted to low redshifts (z<0.5), since this is the range under investigation. To visualize what is expected for a complete sample in UMa, the calculation of N(z) has been performed for 225 AGNs, which should be close to 100%. Surprisingly, it is obvious from the N(z) function (4.2) that AGNs are chiefly missing at low redshifts (z<0.1), and the redshift range 0.1< z <0.5 corresponds well, besides a few lacking objects, to the observed number of AGNs. This mismatch could be produced by the fact that host galaxies are often visible at redshifts z<0.1, which yield to a classification of galaxies and not AGNs. Moreover, the number of AGNs at z<0.1 would be larger as previously expected. Nevertheless, the good agreement in the redshift range 0.1< z <0.5 encourages to take those AGNs, which populate this range. Otherwise the random samples would consist of substantially more AGNs at z <0.1 and the clustering signals would be swamped away. Note, that the separation two objects have under an angle of 10° is $49h^{-1}$Mpc (Appendix A) at z=0.1 and the separation under the same angle corresponds to $25h^{-1}$Mpc at z=0.05. Consequently, more objects in the random sample would contribute to clustering signals on scales $<20h^{-1}$Mpc, since angle separations of ≈5-15° at z<0.1 are sufficient for that.

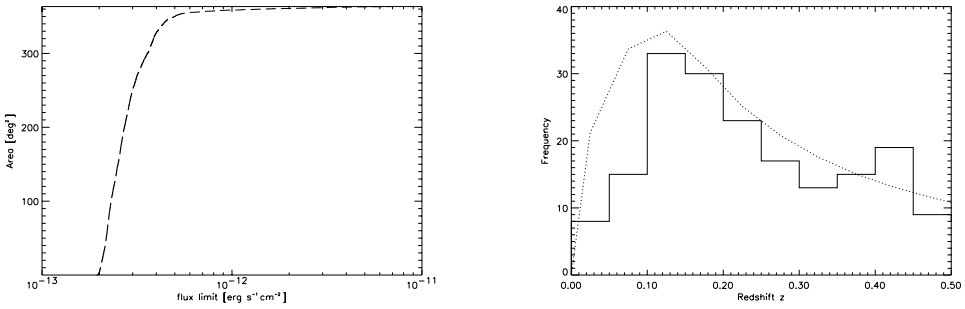

Figure 4.2: The available area as a function of the flux limit is depicted for the UMa area (contiguous surface of 363.4 deg^2) in the left panel. The right panel shows the number of AGNs derived from the luminosity function (4.1) at different redshifts. The histogram includes the 182 AGNs from the UMa sample at z<0.5, whereas the dotted line refers to a complete sample of 225 AGNs in UMa.

4.2 2-point correlation function

The spatial correlation function of AGNs at low redshifts is expected to exhibit signals on small scales similar to normal galaxies. None of the investigations has found significant clustering on scales larger than $20h^{-1}$Mpc, so that attention is drawn to smaller scales. 19 pairs of AGNs in the UMa sample have separations smaller than $20h^{-1}$Mpc (s. Appendix C). Among them form three triplets, two of which are real triplets in the sense that all three separations between them are smaller than $20h^{-1}$Mpc. The third triplet shows a filamentary-like shape (fig.

4.3). In total 31 AGNs produce clustering signals on small scales, which makes about 12% of the whole UMa sample. Most of the 19 pairs have redshifts smaller than 0.2, only three of them have larger redshifts (0.211, 0.215, and 0.334). No contributions are made by larger redshift AGNs, which strengthens the restriction to consider AGNs with z<0.5.

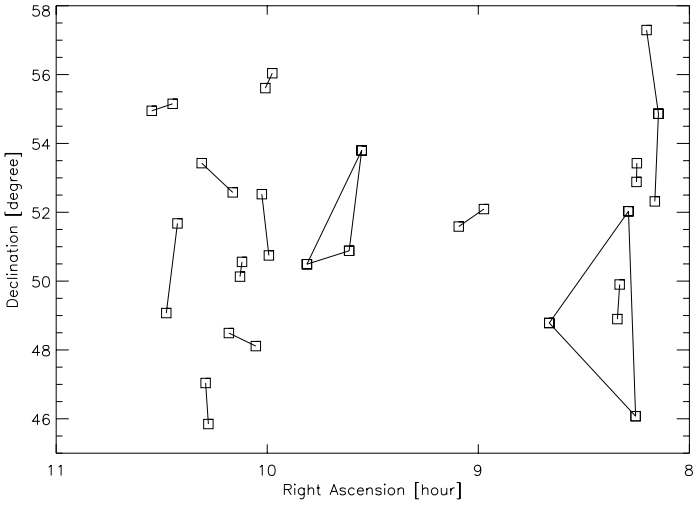

Figure 4.3: The spatial distribution of the 19 pairs in the UMa sample is shown.

scales [h^{-1}Mpc]	0-5	5-10	10-15	15-20	Σ
$N_{pairs}(z<0.5)$	1	5	6	7	19
$N_{pairs}(0.1<z<0.5)$	1	3	2	5	11
$N_{pairs_{B<19.0}}(0.1<z<0.5)$	0	2	2	3	7

Table 4.3: *Pair statistics for the UMa sample on small scales r<20h^{-1}Mpc. The numbers of pairs drops from 19 with z<0.5 to 11 if the ones with z<0.1 are erased and only 7 remain for the brighter optical part (B<19.0).*

4.2.1 The generation of random samples

The procedure of generating random samples having the same selection effects as the real sample comprises three steps: (1) take redshifts from N(z), (2) take L_x from $d\Phi(L_x,z)/d\log L_x$ for a given redshift, and (3) pick (α,δ) from flux limits ($f_x \sim L_x/d_l^2(z)$). Generally, random numbers x_i of a specific distribution $g(x)$ are picked by generating uniformly distributed pairs (x_i,y_i) in the range $[x_{min},x_{max}]$ and $[min(g(x)),max(g(x))]$ respectively. If the requirement $y_i \leq g(x_i)$ holds, then the quantity x_i will be taken as input for the random catalogue, otherwise it will be repeated from the beginning. This loop is not interrupted before the required number of random data points is reached.

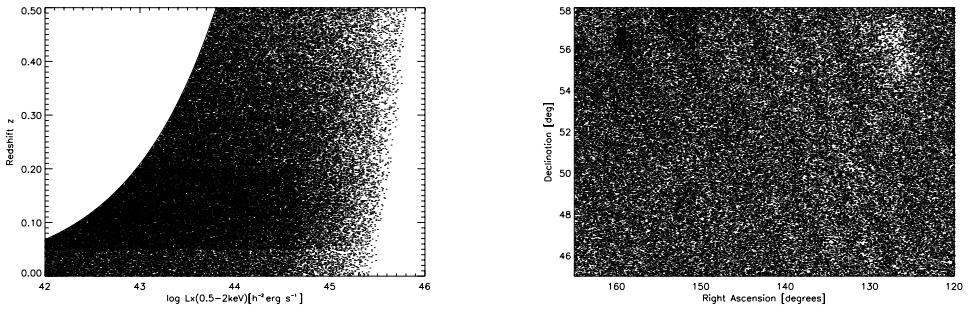

Figure 4.4: A generated random catalogue of 100,000 AGNs is shown with redshift as a function of X-ray luminosity and positions (α, δ). The simulated distributions are evidently akin to the real sample (figs 3.5 and 3.7).

The described procedure was applied to the function N(z) and the X-ray luminosity function $\mathrm{d}\Phi(\mathrm{L_x}, \mathrm{z})/\mathrm{d}\log \mathrm{L_x}$ in order to get random pairs (L_x,z). The luminosity function depends on the redshift via the evolution term $e(z)$. Therefore, the redshift has to be generated before the X-ray luminosity. The random pair (L_x,z) was used to derive the X-ray flux f_x from equation (3.5) and the position on the sky (α, δ) was assigned by means of the flux limits. One of the 9,360 subfields of the flux limit map was taken randomly, and if $\mathrm{f}_x \leq \mathrm{f}_{x_{limit}}$ a position within the subfield (0.25×0.25 deg^2) was assigned by chance to the redshift z, otherwise another subfield was picked and so on. Any number and size of randomly generated catalogues of AGNs (α, δ, z) can be produced by this method utilizing as comparison to the real sample.

4.2.2 Three samples in UMa

Three samples in the UMa region were defined in the redshift range $0.1 < z < 0.5$ and the method described earlier was applied to get random samples having the same number of entries and selection effects as the real sample: (1) including all observed AGNs (N=161), (2) taking AGNs with B<19.0 (N=134), and (3) taking (1) plus AGNs from the incomplete part of the sample, where the part of AGN candidates has to be simulated according to the selection functions (N=199). For each sample 10,000 random samples were generated and the 2-point correlation function has been calculated using five different estimators described in chapter 1. The procedure for sample (1) is straightforward, whereas sample (2) needs few additions due to the optical limit of B<19.0. As a first step, it is recommended to calculate the following quantity according to Stocke et al. (1991)

$$\log(\mathrm{f_x}/\mathrm{f_B}) = 5.37 + \log \mathrm{f_x} + \frac{\mathrm{B}}{2.5}. \tag{4.8}$$

From this distribution (fig. 4.5) a $\log(\mathrm{f_x}/\mathrm{f_B})$ value was selected randomly and the corresponding B-magnitude was derived from equation (4.7). If this B-magnitude is smaller than 19.0, the generated AGN is taken as input for the

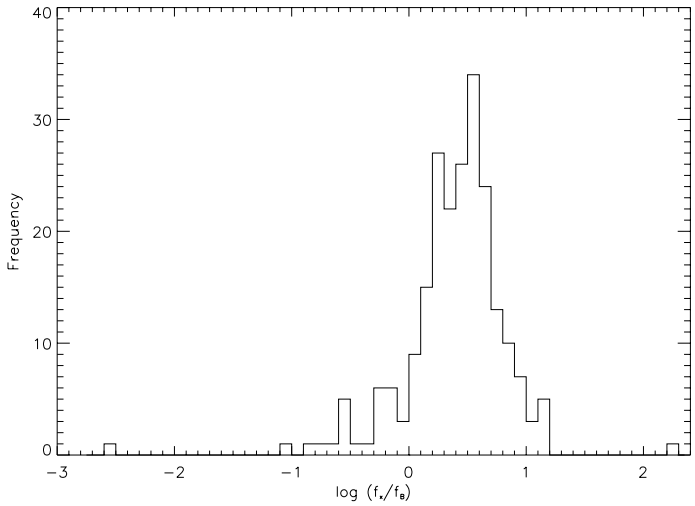

Figure 4.5: The histogram of $\log\left(\frac{f_x}{f_B}\right)$ is in good agreement with a former analysis of Bade (1993), who also studied AGNs from ROSAT. The maximum and minimum values of $\log(f_x/f_B)$ are 2.27 and -2.55, respectively. The distribution has a mean of 0.39 with a standard deviation of 0.44, and the median is 0.43.

random catalogue, otherwise the procedure will be repeated until the required number of random AGNs have entered the catalogue. For the sample (3) the number of AGN candidates that have to be added to the real sample is calculated as follows: 71 AGN candidates, belonging to the featureless objects ($N_{\not f}$=10) or to the one that have not been observed so far ($N_{\not z}$=61), have to be considered, while taking into account the confirmation rate of 82% for them. Another 4 objects with unknown redshifts were classified as BL Lacs due to their spectra. The sum of these components is multiplied by the fraction objects that populates the redshift range $0.1< z <0.5$ in the real sample (61%). The assumption that the missing AGN candidates obey the same redshift distribution as the already known AGNs in UMa has been made. These considerations yield $0.61\cdot(0.82\cdot(61+10)+4)=38$ AGNs, that were added to the real sample of 161 AGNs amounting to 199 AGNs in the regarded redshift range.

4.2.3 Results

As it has been emphasized in chapter 1., some estimators are available for the calculation of $\hat{\xi}(r)+1$ and five of them were chosen for application here[1] : (1) DD(r)/RR(r), (2) DD(r)/DR(r), (3) (DD(r)-DR(r))/RR(r), (4) DD(r)$\cdot$RR(r)/DR^2(r), and (5) (DD(r)-2DR(r)+RR(r))/RR(r). In order to exhibit a clustering signal on a certain scale r, these estimators have to be larger than 1. A concise comparison among them reveals that the esti-

[1]Recall, that DD(r) and RR(r) denote the number of AGN pairs in the real sample and number of AGNs in the random catalogue on scales r. DR(r) is a cross term between one real AGN with the whole random catalogue.

r	DD(r)	DR(r)	RR(r)	$\Delta\xi_{poiss}(r)$	$\xi_1(r)$	$\xi_2(r)$	$\xi_3(r)$	$\xi_4(r)$	$\xi_5(r)$
0-5	1	0.20	0.23	4.35	3.35	4.00	2.48	4.75	2.61
5-10	3	1.37	1.55	1.12	0.94	1.19	0.05	1.48	0.17
0-5	0	0.17	0.17						
5-10	2	0.80	1.07	1.32	0.87	1.50	0.12	2.34	0.37
0-5	1.3	0.23	0.36	3.17	2.61	4.65	1.97	7.85	2.33
5-10	3.5	1.77	2.45	0.76	0.43	0.98	-0.29	1.74	-0.02

Table 4.4: *The clustering results of three differently defined samples on scales r<10h^{-1}Mpc in two bins (0-5h^{-1}Mpc and 5-10h^{-1}Mpc) are depicted for various estimators of the 2-point correlation function and the poissonian error. The samples (1), (2), and (3) as presented in the text, are shown from top to bottom in this table.*

mators (3) and (5) require more stringent constraints than the other, with DD(r)>DR(r)+RR(r) and DD(r)>2DR(r). The less firm constraints are DD(r)>RR(r), DD(r)>DR(r), and DD(r)>DR^2(r)/RR(r) for the estimators (1), (2), and (4) respectively. If there are not significant differences between DR(r) and RR(r), the number of pairs DD(r) in the sample must be twice as large for the estimators (3) and (5) as for the other three estimators in order that the same clustering signal shows up. Consequently, it is not surprising that both estimators find smaller clustering results than the others (table 4.4). The clustering results in the three investigated samples in UMa do not differ significantly from each other. This accordance makes the extracted clustering signal more robust, although not statistically significant, and gives hope that this trend will hold in larger samples, where the signal would be significant above a certain number of AGNs.

The two-point correlation function results for the three different samples were fitted to the standard power law $\xi(r) = (r/r_0)^{-\gamma}$ (fig. 4.7, only for the X-ray selected sample). For this purpose, the minimum χ^2-method was used (i) with r_0 and γ as free parameters (ii) with a fixed exponent γ=1.8. No evidence for clustering on scales larger than $10h^{-1}$Mpc can be seen and the signals on smaller scales are not statistically significant. The plotted errors are poissonian, which generally underestimate the error from bootstrap sampling by a factor of ∼1.7 (chapter 1).

The best-fit for the case of two free parameters yielded r_0=$14h^{-1}$Mpc and γ=0.9, but the 1 σ and 3 σ contours of the χ^2-method indicate that there is a large range of possible values (fig. 4.6). Customarily, the power law is fitted with a fixed γ value of 1.8, which has initially emerged from clustering of galaxies and has been applied to AGNs as well. In order to compare the results with other investigations, this step should be done too. The fitting results are irrefutably dependent on the included data points. Three approaches were performed, one takes into account all nine positive pairs DD(r) binned on $5h^{-1}$Mpc scales over the range 0-$100h^{-1}$Mpc, and two were chosen from bin

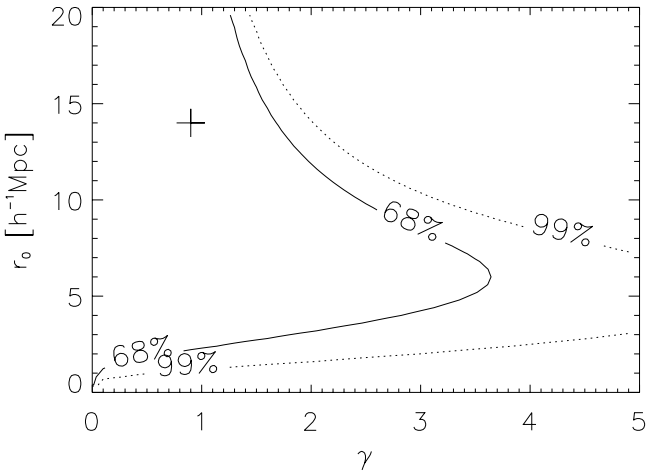

Figure 4.6: The two free parameter χ^2 test gives r_0=14h^{-1}Mpc and γ=0.9 as best fit, marked as (+). The 1 and 3 σ contours comprise a big range of possible values. Specifically, the *nose* at smaller correlation lengths gives confidence, that an extension of this sample will provide a better fit.

sizes of $1h^{-1}$Mpc on small scales ($r < 10h^{-1}$Mpc) including 11 and 18 data points with DD(r)/RR(r)>1 and DD(r)>0 respectively. The results, presented in table (4.5), extend over a range of r_0 ~5-10h^{-1}Mpc with a mean around $7h^{-1}$Mpc. On no account, the correlation length can be more constricted with this sample. Further work has to be conducted in this field with larger samples to investigate this trend and provide significant clustering results at low redshifts.

fitted data points	scales	r_0 [h^{-1}Mpc]	χ^2
DD(r)/RR(r)>0 (N=18)	r<30	$5.71^{+2.86}_{-5.71}$	5.6
DD(r)/RR(r)>0 (N=11)	r<30	$8.59^{+2.52}_{-3.34}$	1.4
DD(r)>0 (N=9)	r<100	$6.97^{+1.97}_{-2.61}$	6.8

Table 4.5: *Power law χ^2-fit of the 2-point correlation results from table (4.4) for the UMa sample with 161 AGNs with a fixed γ=1.8 and 1 σ errors for the correlation length r_0. The choice of the included data points is evidently important to the results.*

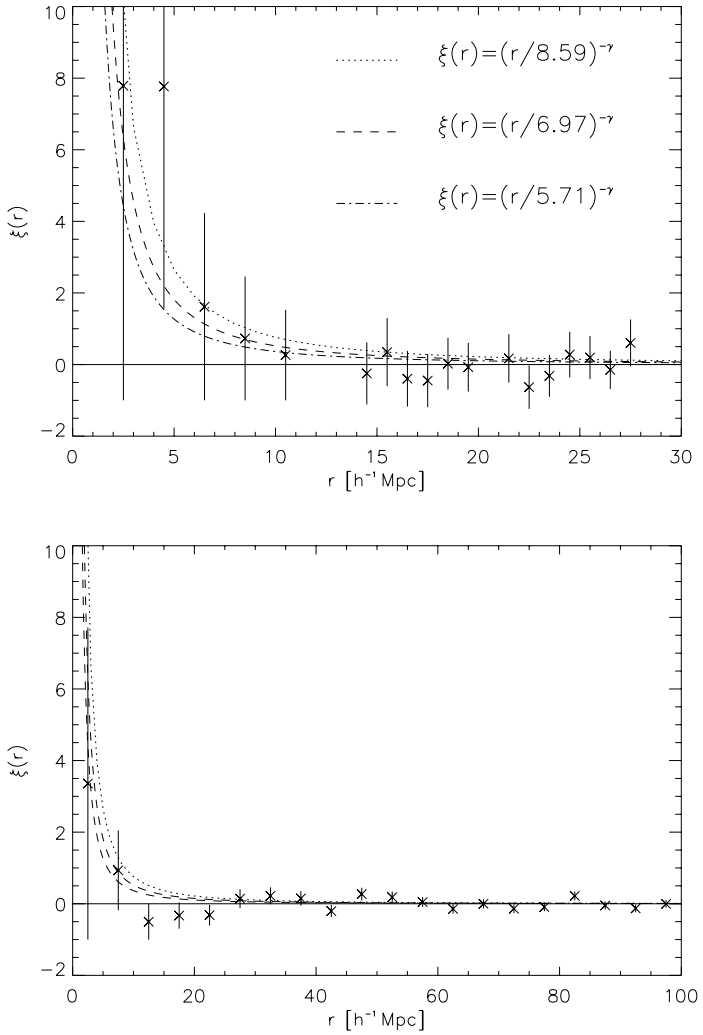

Figure 4.7: The two-point correlation function is plotted on small ($r < 30h^{-1}$Mpc) and large ($r < 30h^{-1}$Mpc) scales for three different fits, as described in text (see also table 4.5). The upper panel is binned to $1h^{-1}$Mpc, whereas the lower panel shows binning of $5h^{-1}$Mpc.

4.2.4 Estimations

The question remains as to how many AGNs are required to exhibit a significant clustering signal under the assumption that the observed clustering trend is real. Therefore, the expected number of pairs of an unclustered in comparison to a clustered population is required.

The number of pairs $N_{\rm pairs}$ with separations $< r$ in a uniformly distributed population in space is

$$N_{\rm pairs} = \frac{N}{2}\left(\frac{4}{3}\pi r^3 \frac{N}{V}\right), \tag{4.9}$$

where N is the number of objects located in the volume V. The volume was calculated from equation (A.10) in the redshift range $0.1< z <0.5$ as V=$4.84465 \cdot 10^7 h^{-3}$Mpc for $\Omega_{\rm ster} = (\pi/180)^2\Omega$, and Ω is the solid angle in square degrees covered by the survey (363.4 deg^2), which gives N_{pairs}=1.12 for r=$10h^{-1}$Mpc and N=161. For a clustered population, the expected number of pairs is

$$N_{\rm c} = N_{\rm pairs} + \frac{N}{2}\frac{N}{V}\int_0^r \xi(r) dV. \tag{4.10}$$

The power law of the 2-point correlation function with r_0=$7h^{-1}$Mpc and γ=1.8 was chosen, so that the integral was easily determined with $dV = \frac{4}{3}\pi r^2 dr$. The expected number of pairs of such a clustered population is N_c=1.61.

In order to measure clustering signals that are significant on the 1 σ level, the basic requirement is given by $\Delta\xi(r) < \xi(r)$, which can be replaced for the standard estimator DD(r)/RR(r) by [DD(r)/RR(r)]/[(DD(r)/RR(r)-1)]^2 <RR(r). Considering the ratio R=$N_c/N_{\rm pairs}$=1.4375 of the clustered population to the unclustered one, which is identical to DD(r)/RR(r), gives R/(R-1)^2 <RR(r). Then the minimum number $N_{\rm min}$ of required AGNs, that show significant clustering is

$$N_{\rm min} > \sqrt{\frac{2V\frac{R}{(R-1)^2}}{\frac{4}{3}\pi r^3}}. \tag{4.11}$$

The minimum number of AGNs in the UMa sample is $N_{\rm min}$=417 with respect to the 1 σ poissonian error and r_0 =$7h^{-1}Mpc$, while the number of required AGNs is found to be 706 and 247 for correlation lengths of $5h^{-1}$Mpc and $10h^{-1}$Mpc, respectively. The estimate of $N_{\rm min}$ hinges strongly upon the clustering strengths.

The simulated complete UMa sample warrants an outlook as to what the final stage of the UMa sample, if it is ever reached or not, could contribute. The values for DD(r<$10h^{-1}$Mpc)=4.8 and RR(r<$10h^{-1}$Mpc)=2.8 are taken from table 4.4. Applying a correlation length r_0=$7h^{-1}$Mpc yields that 281 AGNs are required to achieve significant clustering signals. This estimation, in contrast to the others, is in the scope of the ROSAC project, if the maximum likelihood (the detection probability) of the RASS sources will be lowered (increased), so that the number of AGNs spirals up. In terms of the surface density (N/Ω) 0.77 AGNs/deg^2 are required for significant clustering. The UMa sample (N=161) has a surface density of 0.44 AGNs/deg^2, which is still too low.

4.2.5 The influence of the cosmology

How does the AGN clustering signal change, if another cosmology is considered? For the sake of simplicity and comparability, the standard cosmology ($\Omega_m = 1, \Omega_\Lambda = 0, \Omega_k = 0$) has been applied throughout this work. Fortunately, the whole procedure of deducing the 2-point correlation function does not have to be repeated, while adopting another cosmology. The separations between AGNs scale with a factor, that is defined by the formerly applied cosmology with respect to the new one as a function of redshift. This factor can be taken

as inverse cube-root of the volumes ratios according to Popowski et al. (1998) and Martini & Weinberg (2000). The factor for a Λ-model ($\Omega_m = 0.3, \Omega_\Lambda = 0.7, \Omega_k = 0.0$) and an open model ($\Omega_m = 0.3, \Omega_\Lambda = 0.0, \Omega_k = 0.0$) were derived with respect to the standard model ($\Omega_m = 1.0, \Omega_\Lambda = 0.0, \Omega_k = 0.0$) at $z = 0.5$ to $\sim$1.3 and $\sim$1.1, respectively. Subsequently, the correlation length, r_0, in the two compared cosmologies increases by these factors to 9.1 and $7.7h^{-1}$Mpc.

4.3 Seeking superstructures

The minimal spanning tree technique was applied to the UMa sample using the algorithm of Prim (1957). At first the minimal spanning tree for the entire sample of 264 AGNs was calculated. A plot in three dimensions is presented in Figure 4.8.

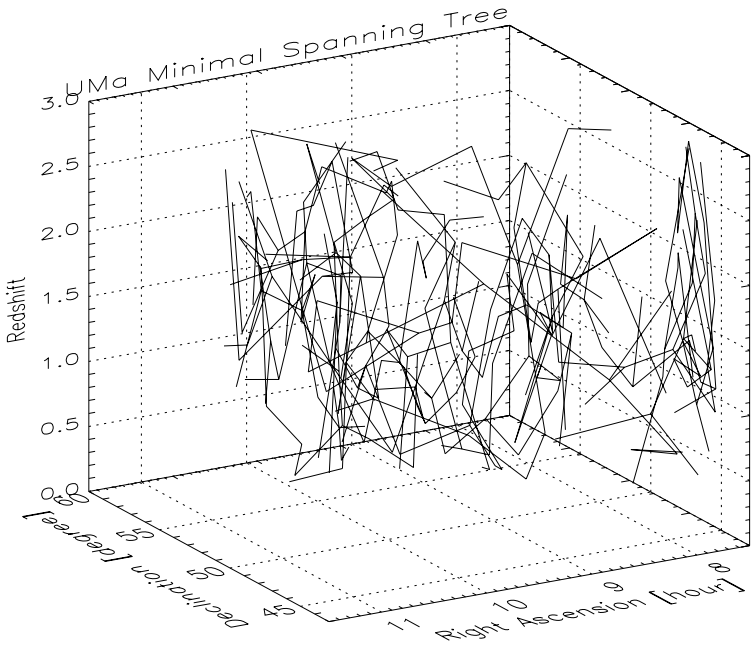

Figure 4.8: Minimal spanning tree for the entire sample in UMa is shown, where the three axes are right ascension in hours, declination in degrees, and redshift z.

Based on the minimal spanning tree, the critical separation distance d_c was found by erasing the connections between AGNs, that have a larger weight (or distance) than a given weight, which is increased by steps of $1h^{-1}$Mpc from 0 to $200h^{-1}$Mpc. For every step size the number of remaining structures in the initial minimal spanning tree was counted (s. Figure 4.9).

The critical separation distance turned out to be d_c=$36h^{-1}$Mpc, at which most structures (N=26) remained in the minimal spanning tree. Nevertheless, it is obvious from figure 4.9 that apart from the first maximum, there

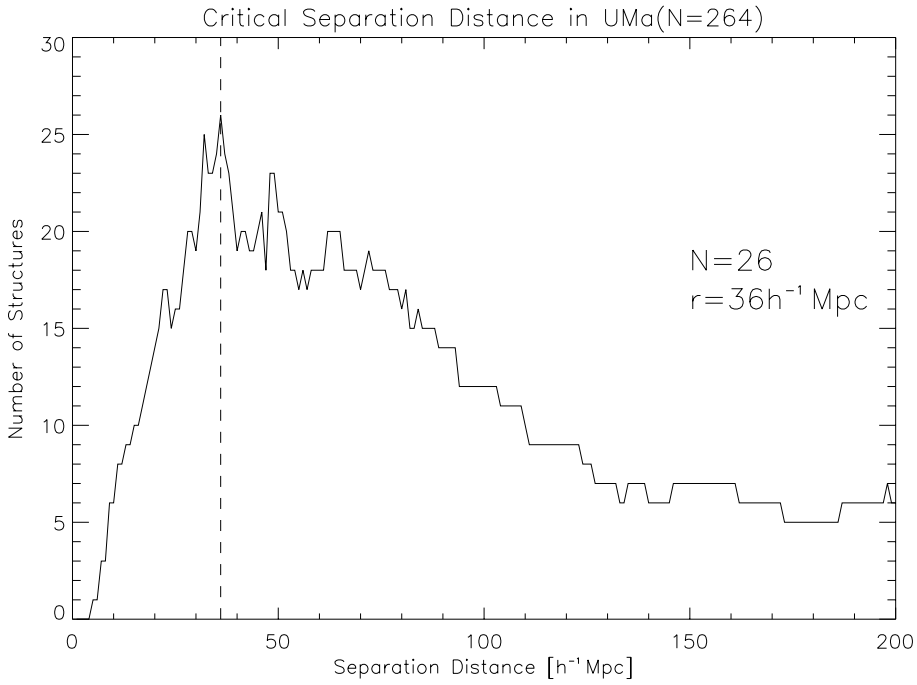

Figure 4.9: The number of structures as a function of the separation distance. The maximum of N=26 structures determines the critical separation distance at d_c=36h^{-1}Mpc.

is a second maximum at d=32h^{-1}Mpc with N=25 structures and a third one at d=48h^{-1}Mpc and d=49h^{-1}Mpc with N=23 structures both. These maxima next to the peak have to be taken into account as well. It is clear that the search for the critical separation distance just gives a *hint* for the scales that have to be considered, while seeking superstructure candidates. At the first peak six superstructure candidates out of 26 were found, that fulfill the requirement of having at least 5 members, but none is a significant superstructure. Since most of the structures are pairs or triplets, it is necessary to impose constraints on the number of members of the superstructure candidate. After the extraction of superstructure candidates their significant level has to be determined. For this purpose, 10,000 random trees were generated within the same volume and with the same number of objects as the superstructure candidate. By comparing the average length and its standard deviation, the significance level is simply the number of random trees n, that have a smaller average length and standard deviation than the candidate

Two significant superstructures have been detected at d=48h^{-1}Mpc, one comprising 26 AGNs on a surface of 19.3×11.2 deg^2 with a significance level of 0.15% (=3.17 σ) at redshifts ranging from 0.086 to 0.197, and the other one consisting of 14 AGNs extended over 12.4 deg in right ascension and 8.9 deg in declination, with a significance level of 1.9% (=3.1 σ). The first stressed structure extends over the whole Uma area in declination, so that the boundaries of

separation distance [h^{-1}Mpc]	32	36	48	49	65
Number of structures	25	26	23	23	20
Superstructure candidates	5	6	8	8	5
Significant superstructures	0	0	2	3	0

Table 4.6: *The search for superstructures was performed on four different separation distances. The number of structures comprises also groups of less than five members, whereas superstructure candidates must possess at least five members. Superstructures that are significant at least on the 2σ level are listed here.*

this agglomeration, that is probably a long filament, are outside of the chosen area. The real size of the structure is hidden and a significance level cannot be derived, so that this structure was omitted from the list of new AGN groups (table 4.7). However, the second significant superstructure of 14 AGNs has dimensions (α, δ,z) of $120.24\times86.39\times141.27h^{-3}$Mpc^3, for a projected extension in right ascension and declination at the mean redshift of 0.215. Surprisingly, the first large (N=26) structure found disappears, when the step size is increased only by $1h^{-1}$Mpc. At d=$49h^{-1}$Mpc three superstructure candidates came up, where one of them was also detected earlier. Thus two further candidates were found with significance levels of 2.44% (=2.27 σ) and 3.86% (=2.07 σ) comprising 19 and 6 members respectively. The superstructure with 19 AGNs is elongated over the entire range in declination, that is why it has to be excluded from the candidates. Conversely, the smaller group with 6 AGNs represents an excellent candidate far from the boundaries of the UMa area. The large new AGN group with 14 members includes optically bright (B$\sim$16.5) as well as faint (B$\sim$19, at the detection limit) AGNs, whereas the smaller group of six AGNs contains mainly faint objects. If the AGNs with B$\geq$19.0 were erased from the groups they would consist of 8 and 4 AGNs, respectively, and their detection as group would have unlikely occurred. That is the reason why the sample with the optical cut at B=19.0 was not investigated.

The results of the MST technique applied to 50 mock samples, that were generated using the selection functions (N(z) and $f_{x_{lim}}$) for the UMa sample, are outlined in figure 4.11. This time the real sample in the redshift range 0.1<z<0.5 with 161 AGNs (instead of 264 AGNs) was chosen as comparison to the mock samples. The findings of the two significant superstructures has not changed in the smaller sample, which is expressed by the same shape of the functions (figs. 4.9 and 4.11) as well as the same critical separation distance of $36h^{-1}$Mpc for both distributions. The number of minimal spanning trees averaged over 50 mock samples peaks at a critical separation distance of $38h^{-1}$Mpc, for which 23.7 groups are found. This number corresponds well with the 23 groups found in the real sample at a separation distance of $36h^{-1}$Mpc. The agreement between the values for the observed sample and the mean of the mock samples indicates that the observed sample is not highly clustered on scales around the peak, which matches to the results of the 2-point correlation function, where no clustering on scales larger than $10h^{-1}$Mpc was found. The small enhance-

AGN groups

α_{2000}	δ_{2000}	z	α_{2000}	δ_{2000}	z
09 28 21.0	+49 37 36	0.238	08 40 01.4	+50 29 44	0.276
09 35 09.4	+48 19 09	0.223	08 42 30.3	+49 58 02	0.305
09 36 12.2	+51 48 08	0.246	08 45 04.3	+54 26 10	0.300
09 46 21.3	+47 11 30	0.230	08 48 56.5	+51 42 25	0.287
09 49 03.6	+47 46 53	0.214	08 54 57.1	+54 48 19	0.255
09 54 09.9	+49 14 58	0.207	08 57 28.4	+52 16 34	0.273
09 56 27.4	+54 04 25	0.208			
09 58 34.0	+56 02 23	0.215			
10 00 32.3	+55 36 29	0.216			
10 04 43.4	+48 01 54	0.197			
10 07 10.1	+50 33 34	0.211			
10 07 44.5	+50 07 47	0.212			
10 15 04.0	+49 25 59	0.200			
10 17 57.7	+47 32 35	0.183			
l_α=120.24h^{-1}Mpc			l_α=53.04h^{-1}Mpc		
l_δ=86.39h^{-1}Mpc			l_δ=58.81h^{-1}Mpc		
l_z=141.27h^{-1}Mpc			l_z=103.60h^{-1}Mpc		

Table 4.7: *Coordinates of the members of the two new significant AGN groups in UMa. Their extension in α and δ is expressed with respect to the medium redshift of each group (z=0.215 and z=0.280).*

ment on small scales of the real sample in comparison to the mock samples could be partially due to the clustering signal that was found earlier. From the concordance of both samples pertaining the MST results, it is not expected that the observed sample has significantly more groups of AGNs than the mock samples. The following limitations were defined for the search of significant superstructures in the mock samples: (1) as in the real sample the superstructure has to contain at least five members, (2) its extension in any direction must be smaller than $200h^{-1}$Mpc, (3) the angular length in right ascension is smaller than 15° and in declination smaller than 10°, otherwise the structure would be too big for the window in the UMa region. In the 50 mock samples, 21 superstructures fulfilling the requirements (1), (2), and (3) at the same time were found, of which only 6 comprised 10 or more members, while the most numerous structure had 13 members. The redshifts of all 21 superstructures matches to the distribution N(z): the majority of 14 structures were located in the redshift regime between 0.1 and 0.2, whereas five were found between $0.2< z <0.3$, and two had slightly larger redshifts than 0.3. The probability of finding superstructures in the mock samples is given by the finding of 21 structures out of 50 (42%), which agrees well with the non-detection of any significant superstructure in the observed AGN sample at the peak of $36h^{-1}$Mpc. Recall, that the two significant AGN groups were found at larger separations. The occurrence of such superstructures is by no means more often than it is

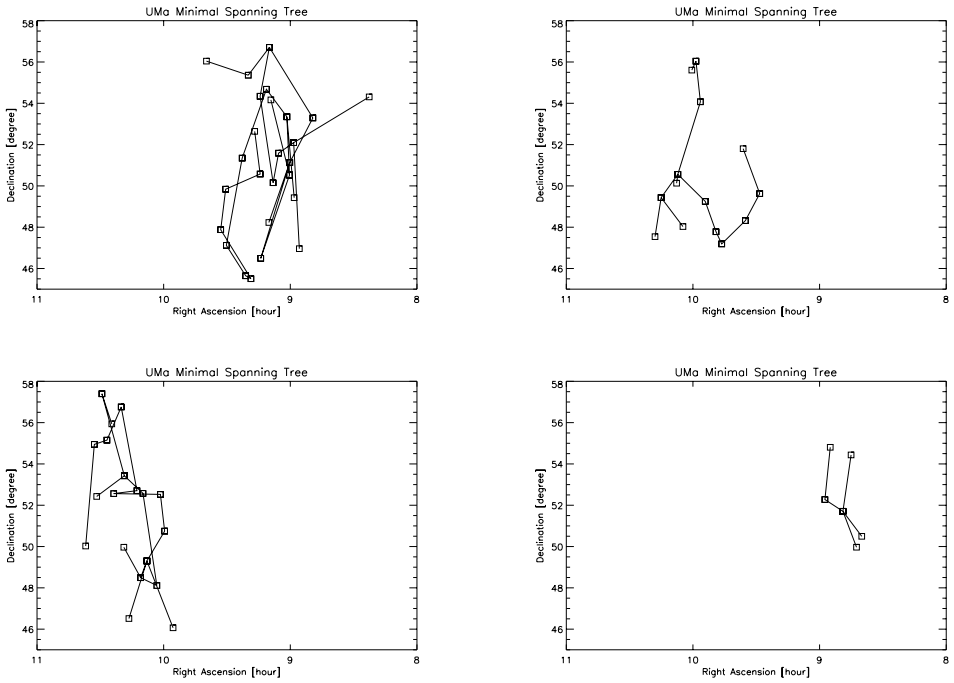

Figure 4.10: Minimal spanning trees of the four significant AGN groups found in UMa. The left panels show the excluded candidates, their elongation over the whole range in declination is clearly visible. On the right are both new AGN groups.

in random distributions, which underlines that their formation happens as frequent as chance fluctuations of similar sizes. It is suggested from the results of the mock samples, that superstructures are scarce in space.

4.4 N-body simulations

4.4.1 Why simulations?

The progress in computer technology within the last ten years has led to an upcoming interest in modeling structure formation. Ever faster computers allow the incorporation of more advanced models, which means that apart from gravitational forces, gas dynamics, chemistry, and radiative transfer have been considered, and also higher resolutions could be realized. In N-body simulations, where dark matter particles of a certain mass are represented by points in a three dimensional space, the gap between pure theory and observations is bridged. The main applications have been the calibration and measurement of cosmological parameters and the attempt to understand nonlinear gravitational clustering.

The first step in all N-body simulations is to define the initial conditions by

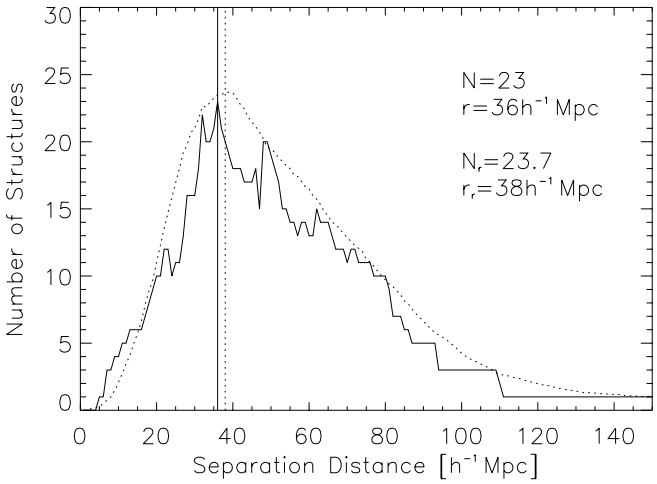

Figure 4.11: Number of minimal spanning trees in 50 mock samples (dashed line) compared to those in the real AGN sample (solid line).

specifying the background cosmology. This, of course, requires more than just the values of H_0 and Ω. The origin of the density fluctuations in the early Universe determines decisively the development of structures as a function of time. The generic predictions of the two plausible mechanisms of inflation (Guth 1981) and topological defects (Vilenkin & Shellard 1994) are opposingly different. Inflation generates Gaussian fluctuations, while topological defects are non-Gaussian.

In principle, two classes of defect models are competing in the non-Gaussian scenario: cosmic strings (Bennett & Bouchet 1990) and global textures (Cen et al. 1991). Independently of the defect class, simulations of non-Gaussian models are complicated, since the formation and evolution of defects is relativistic and fully nonlinear. The more convincing argument as to why Gaussian fluctuations should be considered instead, is that non-Gaussian fluctuations have failed to describe the observed structures in a satisfying manner until now.

In fact, Gaussian fluctuations are simple, because they are completely specified by the power spectrum P(k) (s. chapter 1). The initial conditions are commonly set by the Zeldovich approximation (Zeldovich 1970), that is also valid in the mildly nonlinear regime. In N-body simulations the matter distribution is described as a collection of N particles interacting via gravity. The evolution of the positions and velocities of the dark matter particles, starting from initial conditions at $25 \leq z < 100$, is followed by the chosen numerical technique and gives the gravitational forces between any particles at any time. There are principally four N-body codes: *Particle Mesh (PM) code, P^3M code, TREE code, and Adaptive Refinement Tree (ART) code.* The *particle-mesh or PM code* calculates large-scale forces on particles from a potential obtained by solving the Poisson equation on a regular array of mesh points. This code is fast, so that a large number of particles can be used. A small-scale particle-particle

(PP) contribution can be added to the PM code, which gives the P^3M code (Hockney & Eastwood 1981 and Efstathiou et al. 1985). It has the advantage to evaluate the short range force accurately and the long range force rapidly. A more expensive code with respect to the time it needs to conduct a simulation is the TREE code (Appel 1985, Barnes & Hut 1986, and Hernquist 1987). The main advantage is its flexibility concerning the choice of boundary conditions, which is important for simulating large-scale fluctuations. Finally, Kravtsov et al. (1997) developed the ART code, that refines high-density regions with an automated refinement algorithm in order to reach high force resolution. All the above mentioned codes give similar results, unless scales of individual galaxies ($r<1h^{-1}$Mpc) are concerned (Knebe et al. 2000), where the TREE or ART code should be preferred.

4.4.2 Application to ROSAC

A biased and an unbiased catalogue of dark matter N-body simulations was made available by Rupert Croft, who used the code of Efstathiou et al. (1985), for the needs of the ROSAC project. Every particle has a mass of $1.6{\cdot}10^{14}M_\odot$ and the initial ΛCDM power spectrum is given by the shape parameter $\Gamma=\Omega h=0.25$, which is normalized to $\sigma_8=0.9$.

The crucial point is how to select AGNs from agglomerations of dark matter particles. The local density ρ, defined by the radius to the 10 surrounding particles, in comparison to the mean density $\bar{\rho}$, determines the probability P of *pointing* to an AGN

$$P = A\left(\frac{\rho}{\bar{\rho}}\right)^b, \tag{4.12}$$

where A=0.09 and b=1.5 or 1.0. The meaning of A is to regulate the number of objects that are required for the investigation, and b is close to the linear bias parameter.

For the simulations, a box of length $L=1{,}000h^{-1}$Mpc was chosen including almost 1,000,000 objects. If the observer was in the middle of the volume (box) an All-Sky survey with a depth of L/2, which corresponds to a redshift of ∼0.19, can be simulated. However, ROSAC's AGN sample maps structures out to redshift of ∼0.5, so that the volume had to be extended. This was done by a periodical placing of the same box around itself. 27 cubes placed in the mentioned manner give a big cube with a length of 3L. The center of this big cube is again the location of the observer, but the available depth is now $1{,}500h^{-1}$Mpc. Our analysis was restricted to $z\leq0.5$ ($\sim1{,}100h^{-1}$Mpc), therefore, all objects that are farther away from the observer had to be erased. In other words, a sphere with a radius of $1{,}100h^{-1}$Mpc was cut out of the big cube. The volume of this sphere, which represents the All-Sky survey, is 5.61 times larger than the initial box of length L. Likewise, the expected number of objects within the sphere is about 5,610,000, multiplied by the same factor as the volume. Since the data of the simulated catalogues are in real-space, they have to be converted into redshift-space with the help of their velocities. If the

observer is at position (x_0, y_0, z_0) and the i-th AGN has position (x_i, y_i, z_i) and velocities (v_{x_i}, v_{y_i}, v_{z_i}), the conversion is as follows

$$x_{z-space} = x_i + v_{\mathrm{los_i}} \frac{x_i - x_0}{r_i} \tag{4.13}$$

$$y_{z-space} = y_i + v_{\mathrm{los_i}} \frac{y_i - y_0}{r_i} \tag{4.14}$$

$$z_{z-space} = z_i + v_{\mathrm{los_i}} \frac{z_i - z_0}{r_i} \tag{4.15}$$

where v_{los} is the velocity along the line-of-sight

$$v_{\mathrm{los}} = \left(v_{x_i} + \frac{x_i - x_0}{r_i}\right) + \left(v_{y_i} + \frac{y_i - y_0}{r_i}\right) + \left(v_{z_i} + \frac{z_i - z_0}{r_i}\right) \tag{4.16}$$

with

$$r_i = \sqrt{(x_i - x_0)^2 + (y_i - y_0)^2 + (z_i - z_0)^2}. \tag{4.17}$$

Thus the complete AGN All-Sky survey was constructed and the selection function worked out for the ROSAC sample could be applied in order to get simulated AGN samples. A window having the same size ($8^h \leq \alpha < 11^h$, $45° \leq \delta$ 58°) as the UMa area was projected on the All-Sky survey and the function N(z) was used to filter out 161 objects in the redshift range $0.1 < z < 0.5$. Rotating the All-Sky survey about one of the axis by a random angle Φ, makes it possible to extract several AGN samples from the simulated catalogues in a random way. For five different angles 20 samples from the biased as well as the unbiased simulated catalogue were taken by means of the selection functions for the UMa region, each comprising of 161 objects. For these simulated samples (100 for both types of simulations) the 2-point correlation function was calculated by comparison to 10,000 random samples as it was done before for the real sample (s. chapter 4.2). Since the standard estimator DD(r)/RR(r) was only applied, the cross-term DR(r) has not been taken into account. The results on scales $r < 10h^{-1}$Mpc fit well to a power-law with r_0=3.2-3.3h^{-1}Mpc for the unbiased simulated catalogue, and r_0=5.0-6.5h^{-1}Mpc for the biased one, using γ=1.8 in both cases. The linear bias parameter, b, is defined as

$$\xi_{AGNs}(r) = b^2 \xi_{mass}(r), \tag{4.18}$$

where $\xi_{mass}(r)$ is given by the clustering of the dark matter particles, which is exactly the population of the unbiased simulated catalogue. Adopting a correlation length of $7h^{-1}$Mpc for the soft X-ray selected AGN sample yields $b_{\mathrm{X-ray}} \sim 1.5$. The upper and lower limits for the bias parameter can be taken from the error (± 2) of the AGN correlation length as $b_{low} \sim 1.2$ and $b_{up} \sim 1.7$.

In a last step, the simulated AGN catalogues are used to apply the MST technique for all 100 samples of each catalogue. The distribution of the averaged number of structures with at least five members as a function of the separation distance is shown in figure (4.12). The biased samples peak at the significantly smaller separation distance of $41h^{-1}$Mpc, in contrast to the unbiased sample, that has a maximum at $48h^{-1}$Mpc. The interesting quantity is the number

of significant superstructures (at least on a 2 σ signal) in the random samples. Therefore, some constraints concerning the identification of superstructures has to be defined as only structures with extensions less than $200h^{-1}$Mpc in all of the three axes (α, δ, z), and angular extensions less than 15° in α and 10° in δ are selected. The angular selection is chosen in order to avoid boundary effects on more than one edge of the window of the UMa area. The total number of significant superstructures amounts to 39 in the biased samples and 27 for the unbiased catalogue, which is expected, since the biased samples consists of more strcutures at lower separations (fig. 4.12) and a biased population is by definition more clustered than an unbiased one. This result suggests that the probability of finding superstructures depends on how strong the considered population is biased with respect to the dark matter content of the Universe. The more biased the population is the more superstructures are likely to be found. The bias characteristic of the real sample in UMa resembles the one of the biased simulated AGN catalogues, which implies that superstructures should appear in both samples with a similar probability at the peak of their distribution of number of structures over separation distance. From the biased samples the probability P is given by the occurrence of 39 events out of 100. The non-detection of any significant superstructure in the real sample is consistent with P$\sim$0.4.

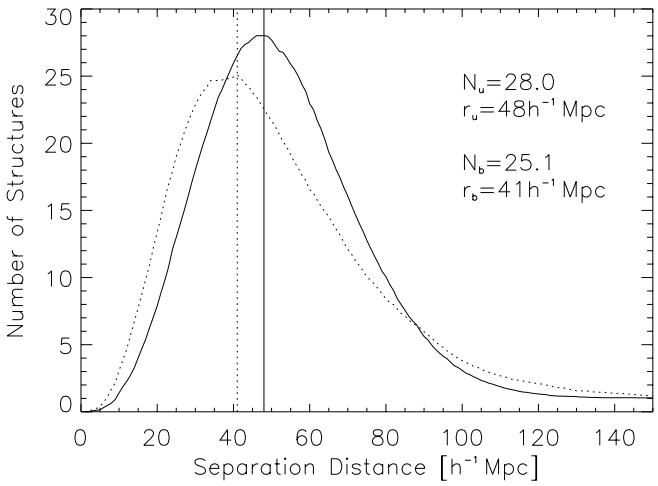

Figure 4.12: The averaged number of superstructures in the unbiased (solid line) and biased samples (dotted line) are shown. Both peaks of the distributions is outlined and the corresponding quantities are given in the panel, where the subscripts u and b denote the unbiased and biased catalogue, respectively.

	0.1-0.2	0.2-0.3	>0.3	N_5	$N_{\geq 10}$	N_{max}	N_{tot}
N_{biased}	26	13	0	7	19	20	39
$N_{unbiased}$	7	16	4	10	4	19	27

Table 4.8: *The number of structures in the biased and unbiased simulated catalogues. The redshift range is divided into three bins: 0.1-0.2, 0.2-0.3, and >0.3. The number of structures comprising 5 (N_5), more than or equal to 10 ($N_{\geq 10}$) members are depicted as well as the largest structures having N_{max} member and total number of significant structures (N_{tot}).*

Chapter 5

Discussion

For an understanding of the evolution of AGN clustering as well as the formation of large-scale structures and/or superclusters traced by AGNs, many points have to be regarded, so that the emerging image is increasingly complex. The goals of ROSAC project were focused on low-redshift AGNs (z<0.5), which was an advantage for the optical follow-up observations, since fainter AGNs are still visible with small telescopes in this redshift range. The incorporation of theoretical ideas is much more complicated here due to the fact that the density field is by far out of the linear stage. Moreover, the reignition of numerous low-redshift AGNs is apparently triggered by the process of minor merging, that is hardly visible and still hidden, so that assumptions about merging rates are no predictable.

5.1 AGN clustering

A complete understanding of the AGN nature is heavily linked to the processes of galaxy formation and evolution. Specifically, the formation of galaxies and/or AGNs has been a matter of debate for years and is hardly known yet. Within the last decade it became observationally clear that the clustering properties of AGNs evolve with time, although the exact clustering evolution has not been resolved completely. The bias of AGNs with respect to the spatial distribution of the dark matter content of the Universe could give deeper insights into the evolution of AGNs and their origin.

5.1.1 Clustering properties of AGNs

The potential of clustering analyses have been outlined in two recently submitted studies (Martini & Weinberg 2000 and Haiman & Hui 2000) on the connection between the clustering and lifetime of AGNs. The authors found results consistent with an AGN lifetime of about 5×10^7 years, assuming a correlation length $r_0 \sim 8h^{-1}$Mpc at z∼2-3. For this work the extended Press-Schechter approximation was used in order to estimate the number density of halos forming

via the process of major merging (Bond et al. 1991 and Lacey & Cole 1993). Unfortunately, this idea cannot be projected to smaller redshifts, where linear theory begins to fail and the dominantly existing low luminosities AGNs are most likely not the product of a major merging process.

The discovery of a close pair of z=4.25 AGNs from the SDSS (Schneider et al. 2000) makes it believable that AGNs cluster extraordinarily strong at high-redshifts. The AGN pair has a separation of 1.1 Mpc in comoving coordinates. The authors postulate that the correlation length r_0 would be between 12 and $30h^{-1}$Mpc at that redshift under the assumption that such an AGN pair occur in only 1% of the sky.

The idea of clustering, that starts with a large signal at high-redshifts, is based on the *biased galaxy formation* scenario, i.e. galaxies form predominantly at sites where the mass density was high along the very highest ridges of large-scale density enhancements. The evolution of the clustering was studied in dark matter N-body simulation (Bagla 1998, Brainerd & Villumsen 1994). Towards lower redshifts, smaller peaks that are farther out of the large-scale density enhancements collapse and form galaxies and AGNs, resulting a in less clustered population. At a later time, when the formation of objects due to collapsing dark matter halos ceases, graviation will drive the galaxy/AGN population to a more clustered state. The minimum of the clustering is expected to be somewhere between z=1-2.

The outlined clustering evolution of dark matter halos has to be compared with galaxies and AGNs. A known bias parameter of these objects as a function of redshifts could help to derive the clustering directly from dark matter N-body simulations. However, the real bias parameter is a function of the mass too, which can be hardly determined from observations. The mass of AGNs is governed by the process of their formation, which in turn depends on the cosmological environment of AGNs. Since there is no way to determine the evolution of the real bias parameter so far, the clustering properties have to be derived directly from well defined samples in a costly manner. A complete list of investigations of the AGN clustering signal is presented in chapter 1.4 and table 1.1. A plot of r_0 as a function of redshift with 1 σ poissonian errors is seen in figure 5.1 At a first glimpse on the clustering data, the evolutionary behavior of the AGN population does not seem to be consistent with the results of dark matter N-body simulation, unless AGN bias is a strange function of redshift and mass. But there is undoubtedly evidence of a large and increasing clustering signal from the PTGS at z>2 (Kundić 1997 and Stephens et al. 1997), whereas the results at low redshifts z<0.5 differ significantly from each other, if the result from the Hα selected sample of Sabbey et al. (2000) is real. The ROSAC result is consistent with the clustering amplitude determined from the IRAS PSC AGNs (Georgantopoulos & Shanks 1994). The clustering in the LBQS survey (Croom & Shanks 1996) at z$\sim$1.5 is consistent with the optical survey of La Franca et al. (1998). These results would match perfectly to the dark matter N-body simulations, if the work of Kundić 1997 underestimated the AGN clustering signal. This is likely, since the considered redshift range in his

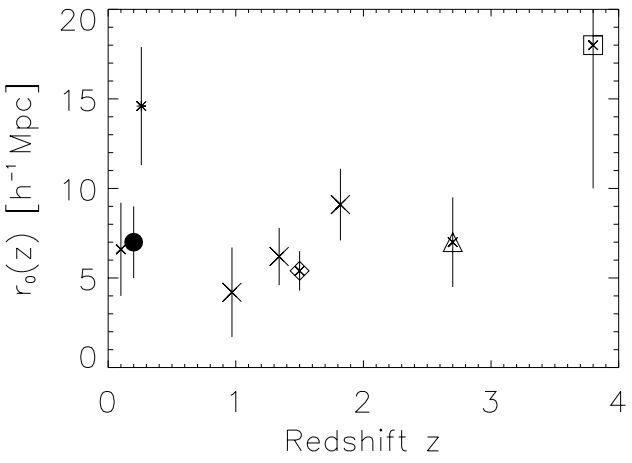

Figure 5.1: The correlation length as a function of redshift gives an idea of the clustering evolution. The results of totally seven AGN clustering explorations are printed: filled dot (ROSAC), small cross (IRAS), small cross with bar (Hα survey), three large crosses (optical survey of La Franca et al.), diamond (LBQS), triangle (PTGS, Kundić), and big square (PTGS, Schneider et al.).

investigation is 0.7-4.7, so that the clustering is averaged over this range. The author found that the clustering amplitude ratio of the high- and low-redshift subsamples is $\xi(z > 2)/\xi(z < 2)$=1.8, which suggests that the correlation length for the high-redshift subsample should be $\sim 10h^{-1}$Mpc. The critical redshift, where the correlation length has a minimum is then obviously located around z$\sim$1. A strong growth towards larger redshifts and a slower development, even if the result of Sabbey et al. is taken into account, towards smaller redshifts evidently occurs.

The ROSAC clustering study strengthens the formerly determined correlation length of IRAS AGNs at low redshifts. Moreover, the clustering evolution scenario, which is based on dark matter N-body simulations, provides a good fit to the observations over the whole available redshift range [0,4]. Future work should investigate the missing and highly interesting redshift range z$\sim$0.5-1.5 in order to assess the minimum clustering signal, where the formation of galaxies and AGNs in the peaks of the density field ceases and gravitation becomes the motor of the growth of structures in the Universe.

Another interesting result pertaining the small-scale clustering is a study of the field X-ray source population from the Chandra X-ray Observatory in 4 different fields (Cappi et al. 2000). Two of them point towards two clusters of galaxies (3C295 and RXJ003033.2+261819 with z=0.46 and z=0.5, respectively), whereas the other two were non-cluster fields. The source surface densities around the two clusters exceeded by a factor of two the value expected from logN-logS from ROSAT and Chandra. In comparison to the two non-cluster

fields no significant excess was found. Further determination of the redshifts of AGN candidates could reveal the first enhanced density of AGNs in the outer skirts of a cluster of galaxies. These objects have expected X-ray luminosities of the order of 10^{42-43}erg s^{-1} with faint optical B magnitudes >19.0. Dressler et al. (1999) measured a frequency of AGNs in one of these clusters that is 10 times larger than in other distant clusters. If this work was supported by the finding of more low luminosity AGNs in the outer skirts of clusters of galaxies, the signal of the 2-point correlation function would rise considerably on small scales ($r \leq$1-2h^{-1}Mpc).

5.1.2 Cosmological environments of AGNs

Studies of AGN environments by means of imaging surveys gave rise to some contradictory results at low redshifts, where the AGN population is dominated by the less luminous Seyfert galaxies. Conversely, good agreement among the published investigations has been achieved at larger redshifts (z>0.6). The environments of radio-loud and radio-quiet AGNs differ from each other in the sense that radio-loud AGNs reside in richer environments than radio-quiet AGNs (Yee & Green 1984, Yee 87 1987, Ellingson et al. 1991, Hintzen et al. 1991, Yee & Ellingson 1993, Boyle & Couch 1993, Smith et al. 1995, Hall & Green 1998, Croom & Shanks 1999, Sánchez & González-Serrano 1999, Smith et al. 2000, Wold et al. 2000). However, in the low-redshift regime the environmental differences of radio-loud and radio-quite AGNs disappear (Fisher et al. 1996, Bahcall et al. 1997, McLure & Dunlop 2000). The preferred AGN environments are generally groups of galaxies with up to 20 galaxies, poor clusters (R=0), and sometimes denser or richer regions like clusters of galaxies with richness R$\geq$1. This paradigm reconciles well with most of the published explorations as long as AGNs that do not belong to density enhancements (superstructures, AGN groups) are considered. Studies of the environments of members of such AGN groups show that the difference between radio-loud and radio-quiet AGNs evaporates even at high redshifts, which is, of course, expected for a density enhancement. This implies that the first question we have to pose in the framework of environmental studies of AGNs is whether the considered AGN is a member of a superstructure or not. If yes, the same environments for all AGN types is expected; if no, the earlier mentioned results apply.

At low redshifts early studies found an excess of neighbors around Seyfert galaxies (Petrosian 1982, Dahari 1984 and MacKenty 1989) in comparison to non-active galaxies. However, Fuentes-Williams & Stocke (1988) found only a marginal excess of companions. Contradictory results regarding the environments of Seyfert 1 and Seyfert 2 galaxies have emerged. According to Petrosian, MacKenty, Laurikainen & Salo (1995), De Robertis et al. (1998), and Dultzin-Hacyan et al. (1999) Seyfert 2s have more neighbors than Seyfert 1s, whereas Dahari and Rafanelli et al. (1995) found no significant differences between them. One of the major problems for such studies is the selection of a comparison sample of normal galaxies.

BL Lacs environments were studied by Wurtz et al. (1997), who detected an enhanced density around 45 BL Lacs at z<0.65. The typical environment of BL Lacs are poor clusters, only 6 objects of the entire sample were found in clusters with richness class >1. Expectedly, BL Lacs exhibit similar clustering environments as radio-loud AGNs, even with a significant increase of the clustering environment with increasing redshift.

The conclusion is that AGNs are located preferentially in groups of galaxies or poor clusters (R=0), and only few of them reside in denser environments with R>1. The studies of the Seyfert environments are still a contentious issue, although most of them showed at least a marginal density enhancement around Seyfert 2 galaxies with respect to Seyfert 1 galaxies. If this is true, the Unified Model (Antonucci 1993), that states a direct view on the central engine (face-on) leads to the appearance of broad-line Seyfert 1 galaxies and the orthogonal view to this axis (edge-on), which is obscured by material, provides a Seyfert 2 galaxy, is called into question in its simplest form. At least a more complex revision of the Unified Model is required in order to match the environmental studies of AGNs; perhaps an evolutionary sequence between Seyfert 1 and 2 as proposed by Maiolino et al. (1995) would help. Finally, three scenarios based on studies of the cosmological environments of AGNs are presented: (1) *The obscuring torus scenario* (Dultzin-Hacyan et al. 1999) predicts an obscured broad-line region, since more companions around Seyfert 2s lead to a higher interaction rate between the AGN and the surrounding galaxies, which in turn enhances the star formation and drives molecular gas toward the center of the galaxy. Therefore all interacting Seyfert 2s should be obscured Seyfert 1s. (2) *The interaction hypothesis* (De Robertis, Yee & Hayhoe 1998) is based on the idea that tidal interactions trigger activity in galactic nuclei. Since different classes of AGNs prefer discordant environments it might be that not a single mechanism is responsible for activity. On the other hand, minor mergers may play a dominant role in low-luminosity AGNs. (3) *The simple interaction hypothesis* (Taniguchi 1999) argues that Seyfert galaxies possess a statistically significant excess of faint (M_V >-18) satellite galaxies leading to minor mergers. The majority of minor mergers may be observed as ordinary galaxies without bars or any signs of distortion. Seyfert galaxies can be explained by minor-merger-driven fueling.

5.1.3 Groups of Galaxies

According to the studies of the cosmological environment of AGNs it seems that groups of galaxies are generally the preferred location for low-redshift AGNs. The low velocity dispersion of their member galaxies supports interactions between them, which means that groups of galaxies should be places in the Universe where tidal interactions (mergers) occur frequently. Consequently, AGNs should be found in groups of galaxies and trace the same large-scale structure as groups of galaxies, which implies that AGN correlations would be due to the groups (their parent population). Bahcall & Chokshi (1991) suggested that optically selected quasars are located in groups of galaxies, whereas radio-selected

quasars reside either in richer groups or clusters of galaxies. Both results are consistent with observations of quasar environments and the universal richness-dependent cluster correlation function (Bahcall & Soneira 1983). The easiest way to perform a consistency check as to whether groups of galaxies are the parent population of the majority of low redshifts AGNs is to compare the clustering properties of both classes. The only published investigation of the clustering of groups of galaxies found a correlation length r_0=8±1h^{-1}Mpc (Girardi et al. 2000), which is in excellent agreement to the ROSAC clustering result. This is a further proof, that groups of galaxies are the preferred locations of AGNs, particularly Seyfert galaxies, in the low redshift Universe.

What else do we know about groups of galaxies? A dense agglomeration of five galaxies, known since it was observed by Stephan (1877) and finally called *Stephan's Quintet*, was the first example of a compact group of galaxies. Hickson (1997) worked out a list of criteria to constrain the selection of compact groups. Hence, these groups are called *Hickson Compact Groups (HCG)*. They consist of about five galaxies placed in a small isolated system. Initially, it was proposed, due to the lack of redshifts, that those groups were filaments seen edge-on (Ostriker, Lubin & Hernquist 1995). Meanwhile, most of the HCGs have been confirmed as *real* groups. The relatively large volume density and the existence of common halos for many compact groups (Ponman & Bertram 1993) as well as a low velocity give rise to a high interaction probability. The merging of all members of the group does not seem to be a surprise, and would form a massive merger remnant. Two such fossils have been reported by observations in X-rays and optical so far: RXJ1340.6+4018 (Ponman et al. 1994) and NGC 1132 (Mulchaey & Zabludoff 1999). The question remains whether AGNs are really linked to compact groups of galaxies. Many HCGs do indeed contain starburst galaxies and/or AGNs. An extreme example is HGC16, that harbors a Seyfert 2 galaxy, two LINERs, and three starburst galaxies (Ribeiro et al. 1996). In an examined sample of 17 HCGs (Coziol et al. 1998) a significant fraction of galaxies display AGN activity. About half of the spectroscopically determined AGNs belong to low-luminosity AGNs (Seyfert 2 galaxies and LINERs). This analysis has been recently confirmed by a more extensive examination of 49 compact groups (Coziol et al. 2000). Another investigation claimed that no statistically significant difference in the occurrence of emission-line galaxies between HCGs and the field exist (Shimada et al. 2000). The fate of the HCGs are the evolution towards luminous or ultraluminous infrared galaxies via multiple mergers (Borne et al. 2000), quasars (Sanders et al. 1988) or even elliptical galaxies (Nishiura et al. 1997). Even though indications emerge from observational studies that compact groups harbor AGNs and starburst galaxies, it is not yet clear if the triggering of nucleus activity is directly linked to the environment of compact groups.

The monster V Zw 311

An excellent target of an ongoing interacting system and future merger is the poor cluster or group of galaxies V Zw 311 (Zwicky 1971, also known as Abell

407 (Abell 1958). This *nightmarish monster*, as Struck (1999) called it in his review about Galaxy collisions, is a multiple-nucleus system consisting of 9 galaxies. The redshift of the group was explored by Peterson (1970) and Trevese et al. (1997), who observed 3 nuclei and later by Schneider & Gunn (1982), who studied the entire group giving z=0.047 for the core of V Zw 311. Stripped material from the group members is responsible for the envelopes (fig. 5.2), which define its boundaries to be in a radial distance of about 10 kpc from the center.

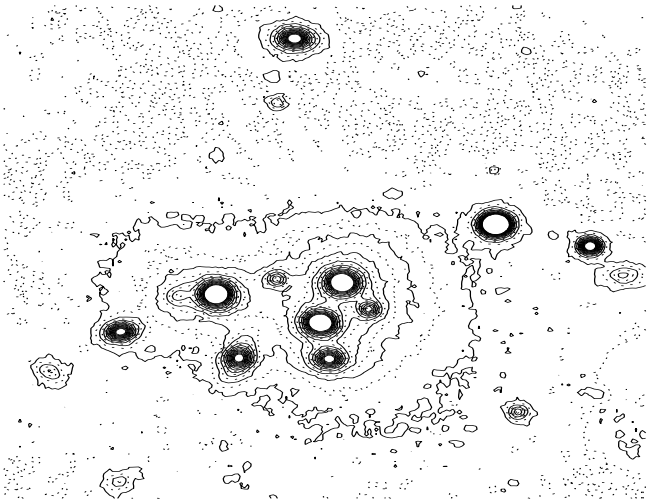

Figure 5.2: Contour plot of the direct image of V Zw 311 exposed for 180s with a Johnson R filter. The envelope of the group is visible. North is at the top, and East to the left.

V Zw 311, $3^h\ 1^m\ 51.5^s\ +35^d\ 50^m\ 30^s$, z=0.047

Own observations of V Zw 311 were made the 18th of March 2000 at the Calar Alto Observatory. For this purpose, spectroscopy of four objects and a direct image in the R-band were obtained at the 2.2m telescope furnished with CAFOS. The best of the four spectra is shown here. None of them reveal any signs of nucleus activity, so that they have to be classified as normal galaxies.

What is the fate of V Zw 311? Without any doubts this group of galaxies will evolve towards a heavily interacting system, that will merge into a cD galaxy during its final stage. This procedure will take a few billion years, meanwhile induced gravitational instabilities or merging could trigger AGN activity in the future. All nuclei seen within the envelope are trapped and will be victims of this unavoidable development. The origin of such an assembly of galaxies is at most poorly understood. A giant galaxy, perhaps two merged galaxies, may capture some smaller surrounding or encountering galaxies almost simultaneously. Now dynamical friction comes into the game and controls the evolution of the group.

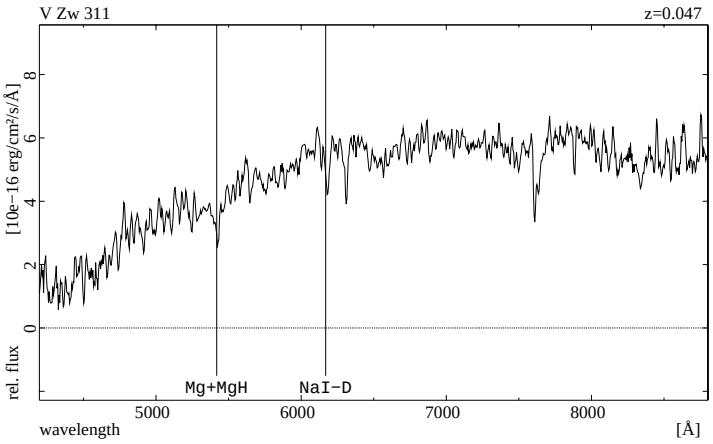

Figure 5.3: This spectra comes from the bright nucleus that has a satellite system as companion. The redshift measured due to absorption of Mg at λ5416 and NaI-D at λ6170 is 0.047, which corresponds to earlier investigations, and the exposure time was 600s.

5.1.4 AGN fueling and merging

A still unsolved problem is how the supermassive black hole in an AGN is fueled. The most promising mechanisms suggested that could remove angular momentum from the host galaxy's gas and pump the fuel into the inner region in order to achieve the observed luminosities of AGNs are tidal interactions (Toomre & Toomre 1972) and stellar bars within the galaxy (Schwarz 1981).

The search for bars within AGNs has revealed few indications of a relation between their existence and nucleus activity. Martini & Pogge (1999) found 5 nuclear bars among a sample of 24 Seyfert 2 galaxies. This result is in good agreement with ground-based (Mulchaey & Regan 1997) and Hubble Space Telescope observations (Regan & Mulchaey 1999). Consequently, only a minority of Seyfert galaxies is furnished with large-scale stellar bars. Likewise, small-scale bars as predicted by the *bars within bars scenario* (Shlosman, Frank & Begelman 1989) are ruled out by observations (Martini & Pogge 1999). Instead, the same authors find a common morphological feature in the center of AGNs to be dusty *nuclear spirals*, that have been observed in normal spiral galaxies before (Phillips et al. 1996) as well as in Seyfert galaxies (Quillen et al. 1999; Regan & Mulchaey 1999). Nuclear spirals are probably formed by shocks propagating in the disk. In this frame, AGN fueling occurs in a two-step process: (1) interactions and large-scale stellar bars can remove angular momentum from the gas and drive it into the inner hundred parsecs of the AGN, where it is assembled in a nuclear disk, and (2) from here shocks or other hydrodynamic effects funnel the fuel into the inner region, where the supermassive black holes capture the gas.

Observational investigations, as mentioned above, indicate that even though stellar bars play certainly a role in fueling AGNs, most of the AGNs are likely ignited by interactions. As Hernquist & Mihos (1995) and Mihos & Hernquist (1996) demonstrated by the means of N-body simulations mergers (major or minor) supply enough gas to fuel an AGN. However, the more luminous AGNs are presumably produced by major mergers ending up in elliptical systems (Hernquist & Barnes 1991), whereas the low-luminosity AGNs, namely the Seyfert galaxies and LINERS (spiral galaxies mainly), are generated by minor mergers. The problem for the minor merger scenario is that these interactions between the host galaxy and the satellite system (dwarf galaxy) are hardly recognizable, then a considerable amount of Seyfert galaxies show little or no evidence for a recent merger. The typical timescale for completion of a minor merger is of the order of $\sim 10^9$yr, which may be enough time to smear out the relics of such a process. Therefore, ordinary-looking galaxies could have had a minor merging occurrence (Walker, Mihos & Hernquist 1996).

How does the cosmological environment influence merging events? Gottlöber, Klypin & Kravtsov (2000) performed N-body simulation in order to find answers to the posed question. Galaxies are formed via merging and accretion of small objects according to hierarchical scenarios. Their result suggests that merging occurs predominantly in clusters and groups of galaxies at $z>2$, whereas at lower redshifts ($z<1$) mergers develop a predilection for groups as their environments. At that redshifts the merger rate of isolated halos is three times larger than that of cluster halos, and the merger rate of halos that have its final stage in groups of galaxies are about a factor of 1.5 less frequent than isolated merger halos. Hence, major merging happens chiefly between field galaxies at low redshifts producing the few known bright elliptical AGNs. Conversely, major mergers in groups or cluster becomes more and more unlikely at $z<1$, which demands a further mechanism for the ignition of low luminosity AGNs.

5.1.5 Ultraluminous infrared galaxies - AGNs

Ultraluminous infrared galaxies (ULIGs) have been suggested to be dust-enshrouded AGNs, that are triggered by strong interaction/mergers of two gas-rich spirals (Sanders et al. 1988; Norman & Scoville 1988; Taniguchi, Ikeuchi & Shioya 1999). This is based on the arguments that (i) the bolometric luminosities of ULIGs are comparable to those for AGNs $\sim 10^{12} L_\odot$, (ii) their luminosity function is similar to that of AGNs (Soifer et al. 1987), and (iii) nearly 100% of the ULIGs tunred out to be galaxy mergers (Sanders & Mirabel 1996). Blain et al. (1999) found that about 80% of the total amount of energy generated in merger-induced starbursts/AGNs is released in the far-infrared waveband. That is why future infrared missions like SIRTF and NGST are urgently needed in order to solve some problems in the AGN-starburst connection.

Taniguchi, Ikeuchi & Shioya (1999) discussed whether a supermassive black hole (SMBH) with a of mass $\geq 10^8 M_\odot$ can grow in ULIGs in order to form AGNs. If the progenitor galaxy already had a SMBH, it would reach masses of

the order of $10^8 M_\odot$ during the course of a merger due to efficient gas accretion. Even if the progenitor galaxy had no SMBH, star clusters could form a SMBH with $\geq 10^8 M_\odot$. The only requirement for the latter case is that the star clusters contain compact remnants like neutron stars or black holes. Thus, more and more arguments are be gathered that corroborate Sanders' idea of a sequential evolution from ULIGs towards AGNs via the process of a merger or interaction.

Interestingly, the first high-redshift pure starburst submilimeter galaxy was found using the Submm Common-User Bolometric Array (SCUBA) (Ivison et al. 2000). This galaxy turned out to be involved in an interacting system at z=2.56. The abovementioned discovery gives confidence that future missions will disentangle some problems even at high redshifts as previously thought.

A further piece to this big puzzle was provided by Borne & Colina (2000), who found evidence for multiple mergers among ULIGs and suggested that their progenitors are compact groups of galaxies. Finally, an evolutionary sequence from compact groups of galaxies to ULIGs to AGNs will be discussed in the future. One problem still remains, since the AGNs generated by the major merging process in ULIGs will predominantly evolve into elliptical (host) galaxies. However, the observations of low luminosity AGNs at low redshifts show mainly spiral galaxies, which is in contradiction to the above scenario. Subsequently, the minor merging scenario as discussed earlier is needed in order to explain the AGNs in spiral host galaxies.

A starburst in the intragroup medium of the compact group of galaxies known as Stephan's Quintet was detected by Xu, Sulentic & Tuffs (1999). The authors reportedly suggested a new mechanism for inducing starbursts as being caused by a collision between a high-velocity ($\delta v \sim 1000$ kms^{-1}) intruder galaxy and the intragroup medium. Such a kind of interaction is probably rare in the local Universe, however, at high redshifts collisions between galaxies and cold intracluster medium may be frequent, due to the larger filling of clusters with cold gas.

5.2 Superstructures in the Universe

Within the two last decades, a few superstructures formed by less than 20 AGNs, therefore called AGN groups, were detected by means of statistical tools, that compare the considered sample with random samples. Physically, there have always been contentious discussions about the nature of such large structures. Specifically, the acceptance of superstructures as more than chance fluctuations is a matter of debate. The emergence of imaging surveys of faint galaxies within the last years made it possible to seek for the underlying density field around members of AGN groups. The main target has been the largest known AGN group (Crampton et al. 1989) having 23 members at z$\sim$1.1. Several investigations found evidence for a significant clustering signature of chiefly faint red galaxies around some selected AGNs of this group (Hutchings, Crampton & Persram 1993; Hutchings, Crampton & Johnson 1995; Yamada et al. 1997; Tanaka et al. 2001). At first Hutchings et al. proposed that these AGNs

are located in compact groups of starbursting galaxies, which would imply that the members of AGN groups are located in isolated associations and not necessarily that AGNs and galaxies trace the same underlying large-scale structure. Further evidence for clustering of faint galaxies around AGNs that are members of AGN groups was reported by Haines & Clowes (2000), who found an 3.5σ overdensity of galaxies around one member of the Clowes & Campusano (1991).

Another method to search for an overdensity around AGNs is to carry out a survey for MgII absorbers in order to probe halo gas from surrounding galaxies. Williger, Campusano & Clowes (1999) obtained 23 spectra of AGNs that are located in the back ground of Clowes-Campusano group. The authors found a 2.7σ excess of MgII absorbers in the main body of the group indicating the enhanced density of this sturcture.

Most AGN groups have been detected at larger redshifts ($z>0.6$) and subsequent imaging of some members of these groups was performed solely at higher redshifts. Notwithstanding, if these superstructures were real associations they should be observed at lower redshifts as well. The finding of two new AGN groups within the ROSAC project underlines the existence of superstructures over the entire available redshift range from 0.2, where galaxy redshift surveys usually stop, to 2.0, which is the upper distance of the formation of superstructures. An even earlier formation of such large-scale sturctures would challenge the cosmological models and are not expected.

Concerning the space density of superstructures, it can be concluded, that about 2770 should populate the Universe (whole sky and $0<z<2$). This simple estimation was derived from the finding of two AGN groups in the ROSAC project in a volume of $V \sim 4.45 \cdot 10^8 h^{-3}\mathrm{Mpc}^3$. The entire sky covers a surface of about 41,253 deg^2, so that the UMa region makes $\sim$0.88% of it. The expected number of superstructures based on results from ROSAC are not compatible with theoretical estimations (s. chapter 1), where 150 in a CDM model and $\sim$700 in a MDM model are suggested. There are two possible explanations: (1) the chosen area in UMa contains above average superstructures at low redshifts and (2) for the determination of the totally expected number of AGN groups no evolution was assumed, which could be inverse to the typical evolution of the 2-point correlation function. Consequently, the space density of superstructures would increase towards lower redshifts. This idea is not that strange, because AGNs producing the signal in the two-point correlation function at high redshifts were born in the largest density peaks. As time goes by, these pairs accumulate more and more neighboring galaxies and/or AGNs via further collapses of dark matter halos and gravitation. Finally, the dense AGN pairs at high redshifts would appear as superstructures at a later time as well as the AGN groups that have already been a superstructure at higher redshifts. Further support was given by Komberg, Kravtsov & Lukash (1996), who derived the number density of superclusters to be $\sim 1.4 \cdot 10^{-7} h^3 \mathrm{Mpc}^{-3}$. Their estimation is based on the finding of eight rich superclusters (Einasto et al. 1984) consisting of more than 10 clusters of galaxies. If this density value was taken into account the total number of expected superstructures would be $\sim$9500 in the same volume as

used above. This overestimation is evident to an increase of superstructures towards lower redshifts, which supports the idea of Komberg & Lukash (1994), that AGN groups are the progenitors of Great-Attractors in the local Universe.

Appendix A

Cosmological distances and volumes

A general relation between the redshift and comoving distance was given by Mattig (1958), called **metric distance**

$$d_m = \frac{c}{H_0 q_0^2 (1+z)^2}[z q_0 + (q_0 - 1)(-1 + \sqrt{2 q_0 z + 1})], \tag{A.1}$$

where c is the speed of light, H_0 denotes the Hubble constant, and q_0 represents the deceleration parameter, which is $q_0 = 3\Omega_m/2 - 1$ for a standard (matter-dominated) Universe ($\Omega_\Lambda = 0$). The distance R between two cosmological sources is given by (Weinberg 1972)

$$R = \sqrt{D^2 d_{m2}^2 + d_{m1}^2 - 2 D d_{m1} d_{m2} cos\theta}, \tag{A.2}$$

where θ is the angle between the sources seen from the observer and

$$D = \sqrt{\sqrt{1 - k d_{m2}^2} + \frac{d_{m2}}{d_{m1}} cos\theta [1 - \sqrt{1 - k d_{m1}^2}]}. \tag{A.3}$$

For k=0 and q_0=0.5 the distance R is reduced to cosine rule, since D=1. In the following table some metric distances d_m for certain redshifts are shown using equation A.1 and the distance R for the cosine rule of two sources separated by an angle $\theta = 10^\circ$ having the same redshift z.

Redshift z	0.1	0.2	0.3	0.4	0.5	1.0	2.0	3.0
$d_m[h^{-1}\mathrm{Mpc}]$	279	523	738	929	1101	1757	2536	3000
R($\theta = 10^\circ$)	49	91	129	162	192	306	442	523

In the nearby Universe it is more common to use velocities as distance indicators: v=$H_0 r_{Hubble}$, v=cz. The simple Hubble relation v=$H_0 r_{Hubble}$ works well up to redshift z≈0.15, where the deviation from the metric distance reaches the 5% border.

v[km/s]	1,000	3,000	5,000	10,000	20,000	30,000	45,000
Redshift z	0.003	0.010	0.017	0.033	0.067	0.100	0.150
$r_{Hubble}[h^{-1}\mathrm{Mpc}]$	10	30	50	100	200	300	450
$d_m[h^{-1}\mathrm{Mpc}]$	10	30	49	98	191	279	405

The **luminosity distance** d_L is related to the metric distance by

$$d_L = (1+z)d_m, \tag{A.4}$$

whereas the **angular distance** $\mathbf{d}_a$ is

$$d_a = d_m/(1+z). \tag{A.5}$$

Another useful quantity is the **lookback-time** $\tau(\mathbf{z})$, which is the difference of the age of the Universe today t_0 and at a given redshift t(z). In an Einstein-de Sitter Universe (q_0) it is simply defined as

$$\tau(z) = \frac{2}{3H_0}\left[1 - \frac{1}{(1+z)^{3/2}}\right]. \tag{A.6}$$

Some scalings of cosmological parameters (Peacock 1999):

$$H(z) = H_0(1+z)\sqrt{1+\Omega z} \tag{A.7}$$

$$\Omega(z) = \frac{\Omega_m(1+z)}{1+\Omega_m z} \tag{A.8}$$

$$q(z) = \frac{q_0(1+z)}{1+2q_0 z} \tag{A.9}$$

The **comoving volume element** is defined as

$$\frac{dV}{dz} = \frac{d_L^2 c dz \delta\Omega}{H_0(1+z)^3\sqrt{1+2q_0 z}}, \tag{A.10}$$

where $\delta\Omega$ is the solid angle. For a given redshift z' the comoving volume has to be calculated as

$$V(z') = \int_0^{z'} \frac{d_L^2 c dz}{H_0(1+z)^3\sqrt{1+2q_0 z}}. \tag{A.11}$$

Appendix B

Lists of X-ray sources

An overview of the content of the ROSAC project in the Ursa Major area is presented in four tables:

1. AGNs (N=265)
2. Galaxies (N=11)
3. Stars (N=24, of which two are Cataclysmic Variables (CVs))
4. AGN candidates (N=74, of which four are BL Lacs)

The columns are labeled as follows:

RX name	-	X-ray name from ROSAT
α_{2000}	-	Right ascension in equinox 2000
δ_{2000}	-	Declination in equinox 2000
z	-	Redshift
B	-	Apparent magnitude in the Johnson B-band
N_H	-	Hydrogen column densities $[10^{20}\mathrm{cm}^{-2}]$
f_x	-	X-ray flux $[10^{-12}$ ergcm^{-2}s$^{-1}]$
$\log L_x$	-	logarithmic X-ray luminosity in the energy band 0.5-2.0 keV $[h^{-2}\mathrm{erg/s}]$
M_B	-	Absolute B-magnitude
Cat	-	Flag, that is referred to the origin of the redshift

The Flag, that is printed in the left column of the table below, denotes at what telescope and when the X-ray source was observed. The sources with a flag of 1, 2 or 40 have been observed before the ROSAC project was launched. Sources, that were taken from the NASA Extragalactic Database (flag 2), may have also been observed during the performance of ROSAC.

Note, that the X-ray fluxes in the table of the AGN candidates were derived supposing the candidate is indeed an AGN, otherwise the value is wrong.

1 Hamburg Quasar Survey	
2 NASA Extragalactic Database	
3 Calar Alto (2.2m telescope)	
30	Bade & Beckmann, Feb. 1998, 3.5m
31	2.2m Nov. 1997
32	2.2m Sep. 1998
33	2.2m Mai 1999
34	2.2m Nov. 1999
35	2.2m Mar. 2000
4 Xinglong station (2.16m telescope)	
40	already observed
41	Jan. 1998
42	Apr. 1998
43	Oct. 1998
44	Nov. 1998
45	Jan. 1999
5 OHP (1.93m telescope)	
51	Apr. 1998
52	Mar. 1999
6 SAO (6m telescope)	
61	Apr. 1998

AGNs

RX name	α_{2000}	δ_{2000}	z	B	N_H	f_x	$\log L_x$	M_B	Cat
RXJ08013+4827	08 01 18.4	+48 27 23	0.428	16.9	3.504	0.682	44.203	-24.02	45
RXJ08015+4736	08 01 32.3	+47 36 18	0.158	15.8	3.831	4.103	44.074	-22.94	2
RXJ08017+5140	08 01 43.6	+51 40 39	0.193	18.7	4.204	0.559	43.388	-20.52	34
RXJ08023+4956	08 02 19.0	+49 56 16	0.527	18.6	3.854	0.269	43.992	-22.81	33
RXJ08029+4909	08 02 59.0	+49 09 29	0.813	18.7	3.638	0.345	44.509	-23.66	33
RXJ08038+4610	08 03 47.9	+46 10 18	0.514	18.4	3.884	0.364	44.100	-22.96	45
RXJ08044+4917	08 04 24.0	+49 17 04	0.170	19.0	3.617	0.877	43.470	-19.89	52
RXJ08051+5240	08 05 07.6	+52 40 00	0.157	18.6	3.771	0.324	42.965	-20.13	52
RXJ08056+5431	08 05 34.6	+54 31 32	0.405	16.4	3.416	2.090	44.638	-24.39	52
RXJ08067+4841	08 06 44.0	+48 41 44	0.369	18.7	3.802	1.228	44.321	-21.91	33
RXJ08068+4855	08 06 50.1	+48 55 10	0.635	18.9	3.881	0.340	44.269	-22.93	33
RXJ08068+5643	08 06 50.7	+56 43 58	0.180	18.1	3.785	0.361	43.136	-20.93	52
RXJ08077+4518	08 07 43.4	+45 18 48	1.035	18.9	3.763	0.590	44.974	-24.01	45
RXJ08080+5436	08 08 02.7	+54 36 39	0.991	19.0	3.561	0.396	44.758	-23.80	33
RXJ08082+4752	08 08 14.9	+47 52 46	0.546	17.7	3.895	0.427	44.227	-23.79	45
RXJ08087+4949	08 08 41.7	+49 49 55	1.430	18.8	4.235	0.274	44.951	-24.87	2
RXJ08088+5451	08 08 47.4	+54 51 45	0.139	18.4	3.596	0.852	43.277	-20.04	52
RXJ08096+4852	08 09 35.2	+48 52 53	0.116	18.8	4.204	0.600	42.963	-19.30	45
RXJ08098+5218	08 09 49.0	+52 18 56	0.138	15.9	3.870	9.080	44.298	-22.55	2
RXJ08100+5025	08 10 02.7	+50 25 37	1.200	16.9	4.444	0.334	44.869	-26.40	2
RXJ08108+5013	08 10 54.8	+50 13 17	0.324	17.3	4.430	0.287	43.569	-23.08	1
RXJ08110+5714	08 11 00.8	+57 14 15	0.608	18.3	3.595	0.853	44.628	-23.41	34
RXJ08112+5730	08 11 10.2	+57 30 10	0.421	17.5	3.451	0.718	44.210	-23.38	33
RXJ08116+4831	08 11 36.0	+48 31 23	0.700	18.2	4.279	0.461	44.494	-23.88	2
RXJ08122+5717	08 12 09.7	+57 17 37	0.139	18.9	3.440	0.523	43.063	-19.53	52
RXJ08130+5017	08 13 00.0	+50 17 29	0.973	19.0	4.386	0.290	44.606	-23.83	34
RXJ08133+5415	08 13 13.0	+54 16 45	0.779	17.5	3.399	0.561	44.680	-24.74	35
RXJ08133+5012	08 13 18.5	+50 12 27	0.572	18.5	4.390	0.367	44.204	-23.14	34
RXJ08133+4608	08 13 19.4	+46 08 48	0.056	17.6	4.105	1.309	42.657	-18.90	1
RXJ08145+5610	08 14 32.9	+56 10 08	0.511	19.0	4.253	0.706	44.383	-22.38	2
RXJ08149+5325	08 14 56.0	+53 25 32	0.121	17.0	3.467	0.428	42.854	-21.13	1
RXJ08150+5252	08 15 01.8	+52 52 54	0.125	16.8	3.497	2.059	43.565	-21.40	1
RXJ08151+5408	08 15 09.3	+54 08 31	0.451	18.7	3.576	0.702	44.264	-22.34	31
RXJ08152+4604	08 15 17.0	+46 04 30	0.041	17.2	4.284	1.814	42.525	-18.63	2
RXJ08163+4735	08 16 17.6	+47 35 06	0.431	18.4	4.493	0.291	43.839	-22.62	2
RXJ08165+4933	08 16 30.8	+49 33 30	0.684	18.7	4.189	0.496	44.503	-23.32	34
RXJ08168+4953	08 16 51.8	+49 53 31	0.157	18.1	4.175	1.013	43.461	-20.66	41
RXJ08173+5202	08 17 18.7	+52 01 47	0.037	18.4	3.880	0.933	42.146	-17.17	1
RXJ08192+4817	08 19 16.3	+48 17 43	0.222	18.8	4.311	0.467	43.436	-20.74	31
RXJ08194+5223	08 19 28.5	+52 23 53	0.624	19.0	3.885	0.306	44.208	-22.79	2
RXJ08198+4953	08 19 49.2	+49 54 07	0.130	18.6	3.982	0.669	43.111	-19.73	31
RXJ08205+4853	08 20 28.1	+48 53 44	0.130	18.8	4.149	0.312	42.781	-19.54	2
RXJ08226+5419	08 22 36.8	+54 18 35	0.086	16.5	4.178	0.543	42.653	-20.94	2
RXJ08248+4732	08 24 51.2	+47 32 18	0.960	19.0	3.850	0.581	44.895	-23.75	2
RXJ08280+5149	08 28 02.1	+51 49 29	0.355	17.6	4.031	0.532	43.922	-22.95	1
RXJ08313+4500	08 31 17.9	+45 00 22	0.146	18.3	2.658	0.982	43.382	-20.17	31
RXJ08313+4831	08 31 21.0	+48 31 52	0.340	17.5	3.521	1.588	44.357	-22.91	1
RXJ08320+4614	08 32 02.2	+46 14 24	0.050	16.5	2.945	1.776	42.690	-19.65	1
RXJ08342+4914	08 34 17.9	+49 14 37	0.173	16.8	3.581	0.580	43.306	-22.12	31

AGNs

RX name	α_{2000}	δ_{2000}	z	B	N_H	f_x	$\log L_x$	M_B	Cat
RXJ08391+5754	08 39 06.7	+57 54 16	1.534	17.3	4.107	0.286	45.039	-26.52	2
RXJ08398+4846	08 39 49.6	+48 46 59	0.040	16.4	3.171	4.515	42.899	-19.28	1
RXJ08400+5029	08 40 01.4	+50 29 44	0.276	19.0	3.074	0.354	43.514	-20.91	31
RXJ08424+5145	08 42 25.1	+51 45 00	0.790	18.4	2.789	0.302	44.425	-23.82	35
RXJ08425+4957	08 42 30.3	+49 58 02	0.305	17.8	2.873	0.421	43.681	-22.31	2
RXJ08432+5357	08 43 13.5	+53 57 17	0.218	17.1	2.845	0.729	43.614	-22.27	31
RXJ08451+5426	08 45 04.3	+54 26 10	0.300	18.9	2.752	0.510	43.749	-21.16	34
RXJ08486+4753	08 48 38.3	+47 53 18	0.187	17.8	2.550	0.361	43.170	-21.20	35
RXJ08489+5142	08 48 56.5	+51 42 25	0.287	19.0	2.629	0.800	43.904	-20.96	31
RXJ08493+5318	08 49 18.5	+53 17 26	0.112	19.0	2.500	0.698	42.997	-18.87	2
RXJ08518+5228	08 51 51.5	+52 28 23	0.064	17.6	2.417	1.591	42.860	-19.04	1
RXJ08535+5029	08 53 27.5	+50 29 36	0.495	17.8	2.326	0.424	44.131	-23.34	35
RXJ08546+5757	08 54 42.3	+57 57 29	1.322	17.8	4.069	0.284	44.892	-25.68	2
RXJ08549+5448	08 54 57.1	+54 48 19	0.255	18.9	2.369	0.507	43.598	-20.77	31
RXJ08552+5616	08 55 16.4	+56 16 58	0.442	17.8	3.149	0.321	43.906	-23.16	2
RXJ08557+4657	08 55 43.3	+46 57 38	0.090	18.2	2.277	0.715	42.814	-19.17	31
RXJ08565+5041	08 56 32.5	+50 41 12	0.235	16.3	2.114	0.333	43.342	-23.17	1
RXJ08574+4845	08 57 26.0	+48 45 19	0.406	19.0	2.221	0.660	44.139	-21.69	33
RXJ08574+5216	08 57 28.4	+52 16 34	0.273	18.8	1.878	0.660	43.775	-20.98	31
RXJ08578+4622	08 57 52.0	+46 21 53	0.559	17.2	2.073	1.505	44.796	-24.19	1
RXJ08582+4925	08 58 09.4	+49 25 46	0.168	18.5	2.174	0.269	42.946	-20.23	35
RXJ08583+5205	08 58 24.3	+52 05 39	0.089	18.1	1.889	0.824	42.865	-19.22	31
RXJ08585+4822	08 58 27.1	+48 22 52	0.470	18.8	2.124	0.335	43.981	-22.21	35
RXJ08594+4637	08 59 24.3	+46 37 16	0.962	16.9	1.949	0.587	44.901	-25.69	1
RXJ09002+5108	09 00 15.4	+51 07 58	0.125	17.5	2.064	1.665	43.472	-20.58	1
RXJ09003+5031	09 00 22.4	+50 31 36	0.149	17.7	2.067	5.311	44.133	-20.76	1
RXJ09006+5023	09 00 35.2	+50 23 39	0.208	17.5	2.020	0.266	43.132	-21.69	35
RXJ09016+5320	09 01 38.0	+53 20 50	0.162	17.6	1.647	2.827	43.934	-21.01	1
RXJ09030+4650	09 03 03.6	+46 51 05	1.462	19.0	1.686	0.334	45.067	-24.50	2
RXJ09045+4917	09 04 31.9	+49 17 20	0.362	19.0	1.842	0.284	43.668	-21.40	35
RXJ09049+5114	09 04 55.0	+51 14 44	0.225	17.4	1.729	1.104	43.822	-21.94	1
RXJ09055+5135	09 05 33.4	+51 35 06	0.089	17.5	1.672	1.198	43.028	-19.80	1
RXJ09060+4851	09 06 01.0	+48 51 50	0.390	17.2	1.736	1.866	44.554	-23.36	1
RXJ09077+5324	09 07 45.4	+53 24 21	0.711	17.5	1.569	0.724	44.704	-24.38	33
RXJ09081+5009	09 08 08.9	+50 09 18	0.100	18.1	1.569	0.946	43.029	-19.44	1
RXJ09088+4939	09 08 54.5	+49 39 19	0.421	19.0	1.501	1.079	44.387	-21.71	1
RXJ09091+5410	09 09 11.7	+54 09 53	0.142	18.7	1.775	0.709	43.216	-19.63	41
RXJ09094+5216	09 09 24.7	+52 16 34	0.409	18.7	1.359	0.753	44.204	-21.93	41
RXJ09096+5131	09 09 43.5	+51 31 17	0.516	18.7	1.313	1.076	44.575	-22.44	34
RXJ09098+5642	09 09 54.6	+56 42 37	0.111	18.2	2.687	0.399	42.746	-19.67	51
RXJ09098+4510	09 09 54.9	+45 09 49	1.980	16.8	1.271	0.415	45.449	-27.34	2
RXJ09101+4813	09 10 09.7	+48 13 44	0.117	16.5	1.440	4.343	43.830	-21.38	1
RXJ09113+5440	09 11 19.5	+54 40 44	0.169	18.5	1.912	0.277	42.964	-20.22	35
RXJ09127+4602	09 12 43.9	+46 02 35	0.447	18.3	1.222	1.644	44.625	-22.52	31
RXJ09130+5259	09 13 00.9	+52 59 30	1.375	16.7	1.384	1.163	45.542	-26.64	2
RXJ09140+4629	09 14 00.0	+46 29 36	0.137	19.0	1.302	0.378	42.910	-19.21	35
RXJ09142+5034	09 14 17.2	+50 34 29	0.185	17.3	1.271	1.372	43.740	-21.57	1
RXJ09142+5419	09 14 18.8	+54 20 32	0.101	18.6	1.844	0.521	42.779	-18.99	41
RXJ09168+5238	09 16 52.0	+52 38 27	0.190	17.0	1.267	5.211	44.344	-21.93	2

AGNs

RX name	α_{2000}	δ_{2000}	z	B	N_H	f_x	$\log L_x$	M_B	Cat
RXJ09187+4530	09 18 39.3	+45 30 21	0.194	18.7	1.317	0.363	43.206	-20.28	35
RXJ09199+5521	09 19 55.3	+55 21 37	0.122	16.4	2.788	2.711	43.663	-21.69	2
RXJ09199+5106	09 19 57.5	+51 06 08	0.553	16.1	1.208	0.472	44.282	-25.19	2
RXJ09211+4538	09 21 08.5	+45 38 55	0.174	18.8	1.421	1.498	43.723	-19.95	2
RXJ09220+4923	09 22 03.8	+49 23 04	0.762	19.0	1.486	0.773	44.798	-23.03	33
RXJ09228+5121	09 22 47.9	+51 20 44	0.161	17.1	1.257	5.096	44.185	-21.46	2
RXJ09231+4530	09 23 09.7	+45 30 44	0.293	18.1	1.504	1.514	44.200	-21.80	2
RXJ09232+4602	09 23 12.7	+46 02 41	0.725	18.6	1.516	0.336	44.389	-23.32	1
RXJ09245+4722	09 24 35.2	+47 22 29	0.419	18.7	1.523	0.836	44.271	-22.00	41
RXJ09252+5217	09 25 12.7	+52 17 10	0.035	14.6	1.243	20.590	43.441	-20.62	2
RXJ09252+5444	09 25 14.4	+54 44 26	0.474	16.0	2.361	0.597	44.240	-25.05	1
RXJ09257+4852	09 25 43.8	+48 52 30	0.571	18.4	1.435	0.866	44.576	-22.98	41
RXJ09259+4535	09 25 54.3	+45 35 43	0.328	18.0	1.655	0.729	43.986	-22.17	31
RXJ09270+5223	09 27 03.2	+52 23 15	0.603	16.8	1.358	1.360	44.823	-24.69	1
RXJ09283+4937	09 28 21.0	+49 37 36	0.238	18.3	1.278	0.424	43.458	-21.12	31
RXJ09296+5718	09 29 39.6	+57 18 38	1.153	18.5	2.513	0.374	44.880	-24.54	45
RXJ09302+4707	09 30 17.7	+47 07 20	0.160	17.2	1.418	5.575	44.218	-21.36	1
RXJ09305+4644	09 30 36.0	+46 45 07	2.032	19.0	1.518	0.647	45.667	-25.22	2
RXJ09306+4950	09 30 37.6	+49 50 24	0.188	18.7	1.296	26.260	45.036	-20.21	2
RXJ09329+4752	09 32 57.8	+47 52 48	0.197	18.6	1.364	0.822	43.574	-20.41	41
RXJ09330+4950	09 33 01.5	+49 50 28	0.615	18.6	1.336	0.637	44.512	-22.94	33
RXJ09331+5347	09 33 08.8	+53 47 46	0.057	17.8	1.546	0.825	42.473	-18.51	35
RXJ09331+4615	09 33 09.3	+46 15 34	0.770	18.8	1.531	0.282	44.371	-23.25	41
RXJ09340+4943	09 34 00.3	+49 43 19	0.370	19.0	1.370	0.452	43.889	-21.41	41
RXJ09351+4819	09 35 09.4	+48 19 09	0.223	17.6	1.464	0.748	43.645	-21.70	2
RXJ09355+5348	09 35 32.4	+53 48 35	0.686	18.2	1.640	0.589	44.581	-23.61	35
RXJ09361+5148	09 36 12.2	+51 48 08	0.246	18.3	1.283	1.149	43.921	-21.20	41
RXJ09367+5052	09 36 42.9	+50 52 47	0.054	17.1	1.170	0.661	42.329	-19.06	34
RXJ09371+5008	09 37 11.8	+50 08 47	0.275	18.4	1.189	1.302	44.077	-21.34	34
RXJ09375+5437	09 37 32.8	+54 37 06	0.465	18.0	1.918	0.801	44.350	-22.96	1
RXJ09392+4605	09 39 12.3	+46 05 06	0.399	19.0	1.230	0.287	43.762	-21.56	33
RXJ09394+5141	09 39 29.9	+51 41 03	0.608	18.0	1.070	0.853	44.628	-23.49	2
RXJ09395+5449	09 39 31.7	+54 49 09	0.292	18.8	1.605	0.579	43.779	-21.10	2
RXJ09397+5602	09 39 43.7	+56 02 30	0.117	17.5	1.837	2.217	43.538	-20.41	2
RXJ09403+4856	09 40 18.3	+48 56 18	0.793	19.0	1.300	0.399	44.549	-23.10	35
RXJ09405+4623	09 40 33.8	+46 23 15	0.699	17.7	1.178	1.287	44.938	-24.11	1
RXJ09440+4807	09 44 04.4	+48 06 45	0.390	18.5	1.104	0.713	44.136	-22.00	2
RXJ09460+5229	09 46 01.0	+52 29 44	0.449	18.7	0.853	0.616	44.203	-22.09	51
RXJ09463+4711	09 46 21.3	+47 11 30	0.230	17.7	1.037	1.285	43.908	-21.63	2
RXJ09465+5123	09 46 31.6	+51 23 39	0.746	18.3	0.882	0.512	44.599	-23.63	41
RXJ09467+4819	09 46 41.0	+48 19 47	0.426	19.0	0.982	0.305	43.849	-21.69	2
RXJ09470+4721	09 47 04.5	+47 21 42	0.541	18.3	1.019	1.632	44.800	-22.92	1
RXJ09472+5306	09 47 12.7	+53 06 13	0.482	18.5	0.886	0.381	44.061	-22.45	41
RXJ09486+5029	09 48 42.7	+50 29 29	0.056	16.5	0.973	0.333	42.062	-19.72	2
RXJ09490+4747	09 49 03.6	+47 46 53	0.214	19.0	1.010	0.736	43.601	-20.17	41
RXJ09491+5351	09 49 09.7	+53 51 25	0.411	18.2	0.941	0.278	43.775	-22.40	41
RXJ09491+4942	09 49 11.7	+49 43 01	1.098	18.7	0.941	0.428	44.891	-24.09	41
RXJ09500+4831	09 50 00.5	+48 31 30	0.590	16.7	0.854	1.274	44.774	-24.70	2
RXJ09507+4535	09 50 41.0	+45 35 11	1.038	17.3	1.144	0.387	44.794	-25.39	2

AGNs

RX name	α_{2000}	δ_{2000}	z	B	N_H	f_x	$\log L_x$	M_B	Cat
RXJ09528+4937	09 52 48.2	+49 37 46	0.258	16.5	0.853	0.581	43.668	-23.06	41
RXJ09541+4914	09 54 09.9	+49 14 58	0.207	16.5	0.836	2.303	44.066	-22.58	2
RXJ09555+4603	09 55 32.9	+46 03 59	0.152	19.0	1.306	0.195	42.716	-19.44	2
RXJ09556+4532	09 55 39.9	+45 32 15	0.259	16.7	1.256	1.629	44.119	-22.91	2
RXJ09558+4925	09 55 45.2	+49 25 02	0.397	18.7	0.810	0.212	43.626	-21.82	35
RXJ09562+5529	09 56 10.9	+55 29 44	1.401	18.0	0.840	0.501	45.195	-25.33	52
RXJ09562+5459	09 56 13.4	+54 59 04	0.316	18.1	0.787	0.444	43.737	-21.91	41
RXJ09564+5648	09 56 23.7	+56 48 05	0.075	18.2	0.886	0.868	42.736	-18.65	42
RXJ09564+5404	09 56 27.4	+54 04 25	0.208	19.0	0.733	1.078	43.741	-20.08	1
RXJ09570+5631	09 57 02.9	+56 31 35	0.680	17.6	0.836	0.762	44.684	-24.12	1
RXJ09576+5523	09 57 38.2	+55 22 56	0.901	17.8	0.781	0.906	45.027	-24.54	2
RXJ09583+4608	09 58 19.3	+46 08 23	0.648	16.6	1.272	1.216	44.842	-25.05	2
RXJ09585+5602	09 58 34.0	+56 02 23	0.215	18.7	0.835	1.083	43.773	-20.46	45
RXJ09585+5551	09 58 37.6	+55 50 51	1.030	17.8	0.823	0.492	44.890	-24.84	1
RXJ09595+5044	09 59 31.7	+50 44 47	0.144	17.4	0.842	1.253	43.476	-20.88	1
RXJ10002+5036	10 00 13.7	+50 36 45	0.236	18.3	0.833	1.230	43.913	-21.07	1
RXJ10005+5536	10 00 32.3	+55 36 29	0.216	19.0	0.771	0.416	43.362	-20.17	2
RXJ10013+5553	10 01 21.0	+55 53 48	1.390	16.4	0.795	1.605	45.692	-26.91	2
RXJ10015+5231	10 01 32.3	+52 31 33	0.145	18.3	0.720	0.717	43.240	-19.98	41
RXJ10020+5540	10 02 00.2	+55 40 54	0.004	15.2	0.754	0.592	40.009	-15.26	2
RXJ10022+4929	10 02 13.7	+49 29 35	0.400	18.5	0.987	0.584	44.073	-22.05	2
RXJ10022+4808	10 02 14.7	+48 04 22	0.948	19.0	1.037	0.142	44.270	-23.48	2
RXJ10032+4807	10 03 14.1	+48 06 45	0.163	19.0	1.008	0.404	43.095	-19.57	41
RXJ10038+5706	10 03 49.6	+57 06 59	0.289	18.8	0.911	0.322	43.516	-21.02	51
RXJ10042+4826	10 04 13.8	+48 26 06	0.563	18.2	0.985	0.637	44.429	-23.11	1
RXJ10047+4802	10 04 43.4	+48 01 54	0.197	19.0	0.992	0.727	43.521	-19.98	41
RXJ10051+5624	10 05 06.2	+56 24 29	0.090	17.5	0.776	2.049	43.271	-19.74	1
RXJ10053+4805	10 05 16.1	+48 05 32	2.370	17.8	0.969	0.386	45.592	-26.71	2
RXJ10068+4638	10 06 50.3	+46 38 19	0.896	19.0	0.876	0.420	44.688	-23.34	41
RXJ10071+5033	10 07 10.1	+50 33 34	0.211	19.0	0.953	0.490	43.411	-20.13	41
RXJ10077+5007	10 07 44.5	+50 07 47	0.212	17.5	0.953	3.390	44.256	-21.64	1
RXJ10079+4918	10 07 56.3	+49 18 08	0.149	18.6	0.961	0.852	43.339	-19.76	1
RXJ10081+4705	10 08 11.4	+47 05 20	0.343	18.9	0.819	13.290	45.288	-21.29	2
RXJ10085+4629	10 08 31.5	+46 29 53	0.388	19.0	0.862	5.039	44.980	-21.47	1
RXJ10086+5437	10 08 36.1	+54 37 28	0.783	18.8	0.652	0.332	44.458	-23.21	2
RXJ10098+5234	10 09 48.1	+52 34 36	0.174	16.9	0.684	0.842	43.472	-21.78	1
RXJ10108+4829	10 10 53.9	+48 29 27	0.158	19.0	0.910	0.234	42.830	-19.49	41
RXJ10126+5242	10 12 38.6	+52 42 21	0.128	18.9	0.663	0.995	43.270	-19.10	1
RXJ10127+5135	10 12 44.5	+51 35 01	0.672	18.5	0.767	0.455	44.449	-23.18	35
RXJ10128+5652	10 12 55.4	+56 52 18	0.963	19.0	0.826	0.254	44.539	-23.49	33
RXJ10135+5315	10 13 30.1	+53 15 56	1.495	16.2	0.689	0.305	45.042	-27.26	2
RXJ10137+5646	10 13 42.1	+56 46 01	0.292	19.0	0.783	0.252	43.417	-20.83	33
RXJ10140+4619	10 14 01.8	+46 19 51	0.321	17.5	0.843	1.802	44.359	-22.55	1
RXJ10144+5654	10 14 22.7	+56 54 51	0.568	18.0	0.780	0.630	44.432	-23.31	2
RXJ10150+4926	10 15 04.0	+49 25 59	0.200	16.7	0.917	23.450	45.043	-22.31	2
RXJ10151+5728	10 15 07.5	+57 28 55	0.434	18.1	0.991	0.842	44.307	-22.63	33
RXJ10163+4532	10 16 20.2	+45 32 56	1.380	19.0	0.935	0.268	44.908	-24.30	35
RXJ10164+4706	10 16 22.7	+47 06 58	0.820	18.1	1.003	0.364	44.542	-24.05	35
RXJ10165+4630	10 16 28.1	+46 30 50	0.140	18.4	0.956	0.446	43.002	-19.83	41

AGNs

RX name	α_{2000}	δ_{2000}	z	B	N_H	f_x	$\log L_x$	M_B	Cat
RXJ10167+4550	10 16 43.8	+45 50 52	0.333	19.0	0.889	0.640	43.943	-21.13	33
RXJ10169+5235	10 16 52.9	+52 35 10	0.438	18.9	0.674	0.430	44.024	-21.82	51
RXJ10169+4850	10 16 55.4	+48 50 03	0.660	18.7	0.998	0.287	44.232	-22.96	35
RXJ10173+5051	10 17 20.2	+50 51 16	0.484	18.9	0.836	0.417	44.103	-22.06	33
RXJ10175+4702	10 17 31.0	+47 02 23	0.335	18.3	1.072	1.327	44.266	-21.86	2
RXJ10175+4905	10 17 35.0	+49 05 56	0.768	19.0	0.971	0.481	44.600	-23.00	35
RXJ10180+4732	10 17 57.7	+47 32 35	0.183	19.0	1.156	0.414	43.210	-19.83	35
RXJ10183+5137	10 18 17.6	+51 37 45	0.369	18.7	0.876	0.273	43.667	-21.66	33
RXJ10186+5325	10 18 37.8	+53 25 37	0.174	18.7	0.678	0.287	43.005	-19.98	33
RXJ10189+4957	10 18 52.2	+49 57 59	0.154	18.3	0.896	1.692	43.666	-20.13	35
RXJ10189+5726	10 18 54.2	+57 26 46	0.154	18.7	0.964	0.365	43.000	-19.74	34
RXJ10189+4738	10 18 58.3	+47 38 14	2.921	19.0	1.171	0.254	45.615	-25.99	2
RXJ10194+5347	10 19 23.9	+53 48 15	0.757	17.6	0.692	0.783	44.798	-24.34	41
RXJ10195+4832	10 19 35.2	+48 32 27	0.361	19.0	1.106	0.313	43.707	-21.33	33
RXJ10200+5645	10 20 06.5	+56 45 35	0.125	18.6	0.926	0.713	43.104	-19.38	51
RXJ10207+4920	10 20 44.3	+49 20 46	0.390	19.0	1.034	0.543	44.017	-21.50	33
RXJ10211+4523	10 21 05.9	+45 23 31	0.364	19.0	1.059	0.835	44.141	-21.34	45
RXJ10221+4821	10 22 09.6	+48 21 14	0.062	18.6	1.302	0.269	42.060	-17.87	2
RXJ10229+5407	10 22 56.7	+54 07 16	0.341	18.9	0.724	0.286	43.615	-21.27	35
RXJ10236+5234	10 23 39.7	+52 33 48	0.137	17.2	1.040	0.815	43.244	-20.99	41
RXJ10238+5633	10 23 49.9	+56 33 47	0.230	17.8	0.737	0.720	43.657	-21.50	51
RXJ10245+5556	10 24 34.9	+55 56 23	0.197	18.0	0.700	1.408	43.808	-20.96	2
RXJ10250+4556	10 25 04.8	+45 56 06	0.520	18.5	1.281	0.306	44.036	-22.66	51
RXJ10252+4808	10 25 12.8	+48 08 53	0.331	19.0	1.389	0.451	43.786	-21.16	45
RXJ10255+5140	10 25 31.3	+51 40 33	0.045	15.9	1.274	21.280	43.676	-19.87	2
RXJ10261+5238	10 26 14.0	+52 37 50	0.260	17.7	1.180	1.636	44.125	-21.91	40
RXJ10268+5509	10 26 52.9	+55 09 07	0.119	17.2	0.710	4.476	43.858	-20.65	1
RXJ10287+4904	10 28 41.8	+49 04 18	0.043	17.8	1.245	0.885	42.255	-17.87	51
RXJ10292+5723	10 29 15.0	+57 23 53	0.186	17.4	0.570	3.054	44.092	-21.42	2
RXJ10292+5302	10 29 15.3	+53 03 04	0.424	18.5	1.155	0.496	44.055	-22.19	51
RXJ10298+5411	10 29 53.3	+54 11 35	0.232	18.2	0.957	0.272	43.242	-21.14	61
RXJ10304+5516	10 30 25.0	+55 16 20	0.440	17.1	0.660	2.455	44.785	-23.63	1
RXJ10308+5310	10 30 51.0	+53 10 25	1.180	18.3	1.215	0.599	45.106	-24.68	1
RXJ10309+5002	10 30 55.5	+50 02 53	0.790	18.6	1.073	0.257	44.355	-23.47	35
RXJ10309+5119	10 30 56.8	+51 19 00	0.290	18.3	1.254	0.634	43.813	-21.56	52
RXJ10310+4626	10 31 03.4	+46 26 14	0.926	18.5	1.311	1.313	45.214	-23.95	1
RXJ10313+5053	10 31 18.6	+50 53 34	0.239	16.8	1.266	54.370	45.570	-22.63	2
RXJ10317+5225	10 31 43.6	+52 25 34	0.169	18.8	1.233	0.279	42.966	-19.87	35
RXJ10328+5457	10 32 50.0	+54 56 54	0.118	18.7	0.769	1.066	43.228	-19.14	51
RXJ10335+4517	10 33 32.6	+45 17 40	0.822	17.9	1.319	0.314	44.479	-24.28	51
RXJ10355+4503	10 35 32.8	+45 03 54	1.442	18.3	1.274	0.307	45.010	-25.13	35
RXJ10369+5001	10 36 56.7	+50 01 35	0.109	17.9	1.207	0.272	42.564	-19.80	35
RXJ10393+4848	10 39 21.5	+48 48 00	0.426	16.5	1.237	2.227	44.712	-24.21	1
RXJ10396+5330	10 39 35.7	+53 30 36	0.232	17.7	1.153	0.521	43.524	-21.66	35
RXJ10417+5233	10 41 46.8	+52 33 26	0.677	17.0	1.226	0.937	44.770	-24.74	2
RXJ10423+5012	10 42 18.4	+50 12 42	0.469	17.6	1.249	0.531	44.179	-23.32	41
RXJ10434+5307	10 43 25.4	+53 07 51	0.948	18.6	1.099	0.368	44.684	-23.88	45
RXJ10438+4748	10 43 49.4	+47 48 57	1.107	17.0	1.383	0.338	44.797	-25.85	1
RXJ10441+5322	10 44 09.9	+53 22 16	1.897	18.6	1.067	0.512	45.498	-25.42	2

AGNs

RX name	α_{2000}	δ_{2000}	z	B	N_H	f_x	$\log L_x$	M_B	Cat
RXJ10441+4755	10 44 10.1	+47 54 56	0.480	18.1	1.389	0.811	44.385	-22.89	1
RXJ10456+5202	10 45 41.7	+52 02 34	0.290	16.9	1.266	2.710	44.443	-22.96	1
RXJ10456+5251	10 45 42.2	+52 51 10	1.050	18.5	1.136	0.763	45.099	-24.21	2
RXJ10462+5255	10 46 13.8	+52 55 52	0.497	17.6	1.137	3.902	45.100	-23.44	51
RXJ10471+5444	10 47 05.2	+54 44 02	0.216	18.7	0.824	3.061	44.228	-20.47	61
RXJ10487+5131	10 48 41.8	+51 31 16	0.196	18.9	1.282	1.552	43.846	-20.10	51
RXJ10494+5754	10 49 26.0	+57 54 21	0.070	17.5	0.661	3.142	43.234	-19.18	1
RXJ10495+5539	10 49 28.3	+55 39 27	0.315	18.3	0.607	0.301	43.564	-21.68	35
RXJ10507+5003	10 50 43.8	+50 03 28	0.627	18.0	1.396	0.628	44.524	-23.58	41
RXJ10509+5527	10 50 55.2	+55 27 22	0.333	16.9	0.692	4.492	44.790	-23.22	1
RXJ10516+4847	10 51 37.3	+48 47 53	0.373	18.5	1.492	0.303	43.722	-21.94	35
RXJ10525+5030	10 52 37.4	+50 30 40	0.246	18.5	1.354	0.565	43.613	-21.00	61
RXJ10537+4929	10 53 44.2	+49 29 55	0.140	17.5	1.466	1.299	43.466	-20.77	41
RXJ10538+5601	10 53 46.5	+56 01 31	0.645	18.7	0.645	0.321	44.260	-22.88	35
RXJ10539+5401	10 53 57.0	+54 01 47	0.995	19.0	1.028	0.384	44.749	-23.58	2
RXJ10547+4831	10 54 44.7	+48 31 40	0.286	15.6	1.422	5.556	44.743	-24.24	1
RXJ10561+5515	10 56 09.7	+55 16 02	0.257	18.3	0.761	0.346	43.440	-21.25	51
RXJ10569+5215	10 56 57.1	+52 15 23	1.317	18.5	1.135	0.288	44.894	-24.72	51
RXJ10586+5628	10 58 37.6	+56 28 10	0.144	16.2	0.712	5.515	44.119	-22.07	2
RXJ10591+5001	10 59 10.4	+50 01 21	0.595	18.6	1.322	0.545	44.413	-22.86	51

Stars

RX name	α_{2000}	δ_{2000}	B	N_H	Cat	
RXJ08208+4934	08 20 51.1	+49 34 29	18.2	3.970	45	CV
RXJ08312+5134	08 31 14.5	+51 35 05	14.9	3.813	35	
RXJ08388+4910	08 38 45.1	+49 10 53	15.8	3.318	35	CV
RXJ08599+5602	09 00 01.0	+56 02 28	17.7	2.364	52	
RXJ09043+4702	09 04 16.3	+47 02 57	16.7	1.564	35	
RXJ09077+5057	09 07 44.1	+50 57 36	16.6	1.551	35	
RXJ09094+5133	09 09 23.7	+51 33 05	17.2	1.341	35	
RXJ09117+4933	09 11 39.3	+49 33 25	16.1	1.327	35	
RXJ09132+5747	09 13 14.9	+57 47 24	19.0	3.091	45	
RXJ09139+5642	09 13 55.2	+56 42 40	18.6	2.744	51	
RXJ09257+4513	09 25 40.9	+45 13 12	11.5	1.652	35	
RXJ09301+5228	09 30 06.8	+52 28 02	16.0	1.392	35	
RXJ09454+5632	09 45 28.8	+56 32 52	18.2	1.204	52	
RXJ09482+5336	09 48 13.7	+53 36 04	18.2	0.930	35	
RXJ10029+4722	10 03 00.0	+47 22 53	16.3	1.046	35	
RXJ10093+5349	10 09 25.5	+53 49 56	19.0	0.708	33	
RXJ10097+4544	10 09 40.4	+45 44 43	10.0	0.843	35	
RXJ10127+4833	10 12 43.4	+48 33 04	10.0	0.895	35	
RXJ10156+5302	10 15 37.4	+53 02 04	10.0	0.665	35	
RXJ10402+4731	10 40 15.1	+47 31 13	18.9	1.343	35	
RXJ10469+5731	10 46 59.4	+57 30 55	19.0	0.621	45	
RXJ10566+5757	10 56 37.0	+57 57 25	18.4	0.610	35	
RXJ10571+5510	10 57 08.6	+55 09 41	18.0	0.770	35	
RXJ10593+5124	10 59 16.3	+51 24 41	10.0	1.184	35	

AGN candidates

RX name	α_{2000}	δ_{2000}	B	N_H	f_x	
RXJ08040+4923	08 04 02.1	+49 23 29	19.0	3.716	0.335	
RXJ08070+5547	08 07 01.1	+55 47 46	18.5	4.113	0.337	
RXJ08104+5740	08 10 24.5	+57 40 23	19.0	3.434	0.331	
RXJ08124+4651	08 12 25.9	+46 51 30	19.0	4.162	0.322	
RXJ08164+5739	08 16 24.6	+57 39 10	19.0	3.908	1.538	
RXJ08255+4817	08 25 35.3	+48 16 03	17.9	3.961	0.385	
RXJ08273+4905	08 27 16.8	+49 05 31	18.8	3.836	0.254	
RXJ08299+5256	08 29 52.8	+52 56 47	19.0	3.889	0.397	
RXJ08346+5328	08 34 37.1	+53 28 17	18.5	3.515	0.318	
RXJ08401+5216	08 40 05.3	+52 16 18	19.0	2.912	0.203	
RXJ09005+4911	09 00 32.4	+49 11 47	19.0	2.068	0.413	
RXJ09015+5100	09 01 32.0	+51 00 14	19.0	1.987	0.379	
RXJ09036+4600	09 03 37.7	+46 00 37	19.0	1.556	0.280	
RXJ09059+5237	09 05 54.3	+52 37 23	19.0	1.582	0.238	
RXJ09069+4533	09 06 57.0	+45 33 26	18.0	1.420	1.177	
RXJ09080+4615	09 08 59.2	+46 15 37	19.0	1.372	0.161	
RXJ09203+4636	09 20 19.5	+46 36 08	19.0	1.403	0.354	
RXJ09209+4506	09 20 55.3	+45 06 56	19.0	1.434	0.356	
RXJ09292+5013	09 29 15.4	+50 13 35	18.3	1.326	0.919	BL Lac
RXJ09324+4607	09 32 21.1	+46 07 14	19.0	1.637	0.400	
RXJ09331+4845	09 33 04.3	+48 45 40	19.0	1.330	0.238	
RXJ09380+4843	09 38 00.3	+48 43 16	19.0	1.463	0.403	
RXJ09392+5121	09 39 15.7	+51 21 31	19.0	1.071	0.360	
RXJ09393+4823	09 39 19.2	+48 23 33	19.0	1.355	0.210	
RXJ09426+5758	09 42 33.9	+57 58 34	19.0	1.408	0.270	
RXJ09484+5149	09 48 25.9	+51 49 32	19.0	0.800	0.248	
RXJ09490+4627	09 49 58.9	+46 27 24	19.0	1.127	0.352	
RXJ09501+4813	09 50 05.0	+48 13 14	19.0	0.896	0.375	
RXJ09502+4553	09 50 11.9	+45 53 19	18.9	1.146	0.193	BL Lac
RXJ09520+5708	09 51 59.0	+57 08 53	19.0	0.952	0.210	
RXJ09523+5314	09 52 20.1	+53 14 54	19.0	0.801	0.303	
RXJ09542+5635	09 54 10.5	+56 35 30	19.0	0.885	0.364	
RXJ09549+5719	09 54 55.7	+57 19 51	18.5	0.955	0.250	
RXJ09550+4955	09 54 59.0	+49 55 54	19.0	0.816	0.432	
RXJ10042+4626	10 04 13.0	+46 26 20	19.0	0.994	0.186	
RXJ10068+4651	10 06 45.5	+46 51 10	19.0	0.890	0.262	
RXJ10112+5110	10 11 11.3	+51 10 34	19.0	0.849	0.163	
RXJ10114+4700	10 11 22.7	+47 00 41	19.0	0.839	0.317	
RXJ10139+4851	10 13 52.4	+48 51 24	19.0	0.928	0.277	
RXJ10174+5621	10 17 24.6	+56 21 07	18.2	0.860	0.297	
RXJ10179+4706	10 17 53.7	+47 06 16	19.0	1.070	0.531	
RXJ10200+5454	10 20 00.2	+54 54 40	19.0	0.715	0.372	
RXJ10210+5024	10 21 01.0	+50 24 42	19.0	0.982	0.300	
RXJ10227+5104	10 22 41.8	+51 04 08	17.3	1.104	0.322	
RXJ10234+4951	10 23 21.9	+49 51 18	19.0	1.068	0.376	
RXJ10251+5553	10 25 03.3	+55 53 19	18.5	0.702	0.318	
RXJ10256+5105	10 25 37.8	+51 05 43	19.0	1.223	0.352	
RXJ10260+5254	10 26 02.7	+52 54 04	19.0	1.148	0.319	
RXJ10292+5228	10 29 13.2	+52 28 38	19.0	1.226	0.664	

AGN candidates

RX name	α_{2000}	δ_{2000}	B	N_H	f_x	
RXJ10292+4919	10 29 13.6	+49 19 31	19.0	1.186	0.366	
RXJ10295+5106	10 29 33.8	+51 06 17	19.0	1.290	0.271	
RXJ10307+4821	10 30 44.0	+48 21 44	19.0	1.394	0.293	
RXJ10307+5521	10 30 44.1	+55 21 00	19.0	0.676	0.453	
RXJ10316+5035	10 31 37.6	+50 35 36	18.5	1.229	0.335	
RXJ10316+5303	10 31 40.7	+53 03 38	18.7	1.234	0.316	
RXJ10327+4729	10 32 43.8	+47 29 10	19.0	1.514	0.141	
RXJ10346+5505	10 34 37.3	+55 05 09	19.0	0.669	0.780	
RXJ10349+4507	10 34 54.9	+45 07 39	19.0	1.287	0.620	
RXJ10372+4858	10 37 13.7	+48 58 59	18.6	1.183	0.266	
RXJ10373+4755	10 37 23.0	+47 55 21	19.0	1.498	0.327	
RXJ10377+5711	10 37 44.5	+57 11 54	16.5	0.442	2.861	BL Lac
RXJ10381+4642	10 38 10.1	+46 42 40	18.8	1.310	0.387	
RXJ10397+5234	10 39 40.8	+52 34 18	18.4	1.197	0.299	
RXJ10403+5640	10 40 20.3	+56 40 04	19.0	0.407	0.337	
RXJ10407+5644	10 40 44.7	+56 44 47	19.0	0.415	0.886	
RXJ10411+5419	10 41 08.4	+54 19 22	19.0	0.980	0.271	
RXJ10411+5551	10 41 11.7	+55 51 46	18.7	0.459	0.697	
RXJ10443+5043	10 44 17.0	+50 43 52	19.0	1.330	0.333	
RXJ10451+4951	10 45 09.4	+49 51 19	19.0	1.294	0.261	
RXJ10475+4835	10 47 32.3	+48 35 30	19.0	1.390	0.314	
RXJ10477+5437	10 47 47.1	+54 37 45	19.0	0.817	0.563	BL Lac
RXJ10507+4828	10 50 45.0	+48 28 54	16.3	1.410	0.434	
RXJ10532+5441	10 53 10.8	+54 41 56	19.0	0.870	0.245	
RXJ10536+5642	10 53 38.3	+56 42 15	19.0	0.660	0.481	

Galaxies

RX name	α_{2000}	δ_{2000}	z	B	N_H	f_x	$\log L_x$	M_B	Cat
RXJ08036+4753	08 03 34.9	+47 53 53	0.059	18.5	3.703	0.287	42.044	-18.08	45
RXJ08109+5536	08 10 54.3	+55 36 36	0.140	19.0	4.053	0.215	42.685	-19.50	34
RXJ08137+5300	08 13 46.7	+53 00 51	0.140	19.0	3.499	0.215	42.684	-19.45	41
RXJ08561+5418	08 56 08.4	+54 18 53	0.251	19.0	2.022	1.474	44.047	-20.61	31
RXJ09033+5330	09 03 20.7	+53 30 29	0.063	17.9	1.617	0.365	42.206	-18.64	41
RXJ09137+4741	09 13 46.1	+47 41 58	0.060	18.3	1.441	1.812	42.859	-18.11	1
RXJ09326+4901	09 32 38.5	+49 01 46	0.077	17.8	1.398	0.229	42.180	-19.16	45
RXJ09377+5647	09 37 44.8	+56 47 00	0.139	19.0	2.094	0.434	42.983	-19.31	51
RXJ09527+5153	09 52 47.3	+51 53 06	0.214	18.3	0.726	2.900	44.196	-20.84	2
RXJ09585+4738	09 58 33.5	+47 38 52	0.418	18.3	1.130	0.349	43.889	-22.36	2
RXJ10387+5330	10 38 45.8	+53 30 11	0.003	10.0	1.148	1.504	40.164	-19.87	2

Appendix C

AGN pairs

The 19 pairs of AGNs with separations r <$20h^{-1}$Mpc are listed in the table on the next page. Recall, that the separations were calculated for a standard cosmology (Ω_m=1.0, Ω_Λ=0), and distances in a Λ-model or an open Universe at low redshifts (z<0.5) are larger by a factor of $\sim$1.3 or $\sim$1.1, respectively. Moreover, the three triplets are marked by a T_i in the right column of the table.

AGN pairs

RX name	α_{2000}	δ_{2000}	B	z	r	
RXJ08088+5451	08 08 47.4	+54 51 45	0.139	18.4	17.01	T_1
RXJ08098+5218	08 09 49.0	+52 18 56	0.138	15.9		
RXJ08088+5451	08 08 47.4	+54 51 45	0.139	18.4	16.97	T_1
RXJ08122+5717	08 12 09.7	+57 17 37	0.139	18.9		
RXJ08149+5325	08 14 56.0	+53 25 32	0.121	17.0	10.58	
RXJ08150+5252	08 15 01.8	+52 52 54	0.125	16.8		
RXJ08152+4604	08 15 17.0	+46 04 30	0.041	17.2	16.39	T_2
RXJ08173+5202	08 17 18.7	+52 01 47	0.037	18.4		
RXJ08152+4604	08 15 17.0	+46 04 30	0.041	17.2	14.08	T_2
RXJ08398+4846	08 39 49.6	+48 46 59	0.040	16.4		
RXJ08173+5202	08 17 18.7	+52 01 47	0.037	18.4	15.29	T_2
RXJ08398+4846	08 39 49.6	+48 46 59	0.040	16.4		
RXJ08198+4953	08 19 49.2	+49 54 07	0.130	18.6	6.33	
RXJ08205+4853	08 20 28.1	+48 53 44	0.130	18.8		
RXJ08583+5205	08 58 24.3	+52 05 39	0.089	18.1	8.12	
RXJ09055+5135	09 05 33.4	+51 35 06	0.089	17.5		
RXJ09331+5347	09 33 08.8	+53 47 46	0.057	17.8	11.88	T_3
RXJ09367+5052	09 36 42.9	+50 52 47	0.054	17.1		
RXJ09331+5347	09 33 08.8	+53 47 46	0.057	17.8	14.74	T_3
RXJ09486+5029	09 48 42.7	+50 29 29	0.056	16.5		
RXJ09367+5052	09 36 42.9	+50 52 47	0.054	17.1	10.03	T_3
RXJ09486+5029	09 48 42.7	+50 29 29	0.056	16.5		
RXJ09585+5602	09 58 34.0	+56 02 23	0.215	18.7	6.76	
RXJ10005+5536	10 00 32.3	+55 36 29	0.216	19.0		
RXJ09595+5044	09 59 31.7	+50 44 47	0.144	17.4	12.87	
RXJ10015+5231	10 01 32.3	+52 31 33	0.145	18.3		
RXJ10032+4807	10 03 14.1	+48 06 45	0.163	19.0	18.95	
RXJ10108+4829	10 10 53.9	+48 29 27	0.158	19.0		
RXJ10071+5033	10 07 10.1	+50 33 34	0.211	19.0	4.89	
RXJ10077+5007	10 07 44.5	+50 07 47	0.212	17.5		
RXJ10098+5234	10 09 48.1	+52 34 36	0.174	16.9	19.09	
RXJ10186+5325	10 18 37.8	+53 25 37	0.174	18.7		
RXJ10167+4550	10 16 43.8	+45 50 52	0.333	19.0	17.42	
RXJ10175+4702	10 17 31.0	+47 02 23	0.335	18.3		
RXJ10255+5140	10 25 31.3	+51 40 33	0.045	15.9	8.28	
RXJ10287+4904	10 28 41.8	+49 04 18	0.043	17.8		
RXJ10268+5509	10 26 52.9	+55 09 07	0.119	17.2	8.93	
RXJ10328+5457	10 32 50.0	+54 56 54	0.118	18.7		

References

Abell G., 1958, ApJS 3, 211
Adelberger K. L., Steidel C. C., Giavalisco M., Dickinson M., Pettini M., Kellogg M., 1998, ApJ 505, 18
Akylas A., Georgantopoulos I., Plionis M., 2000, submitted to MNRAS
Alpher R. A., Herman R. C., 1948, Nature 162, 774
Anderson N., Kunth D., Sargent W. L. W., 1988, AJ 95, 644
Andreani P., Christiani S., 1992, ApJ 398, L13
Antonucci R., 1993, ARA&A 31, 473
Appel A., 1985, SIAM J. Sci. Stat. Comput. 6, 85
Arp H., 1984, ApJ 285, 547
Avni Y., Bahcall J. N., 1980, ApJ 235, 694
Bade N., 1993, PhD thesis University of Hamburg
Bade N., Engels D., et al. W. V., 1998, A&AS 127, 145
Bagla J. S., 1998, MNRAS 299, 417
Bahcall J. N., Kirhakos S., Saxe D. H., Schneider D. P., 1997, ApJ 479, 642
Bahcall N. A., 1991, ApJ 376, 43
Bahcall N. A., Ostriker J. P., Perlmutter S., Steinhardt P. J., 1999, Science 284, 1481
Bahcall N. A., Soneira R. M., 1983, ApJ 270, 20
Bahcall N. A., Soneira R. M., 1984, ApJ 277, 27
Baldwin J. A., Phillips M. M., Terlevich R., 1981, PASP 93, 5
Balzano V. A., 1983, ApJ 268, 602
Barbieri C., Christiani S., Iovino A., Nota A., 1987, A&AS 67, 551
Bardeen J. M., Bond J. R., Kaiser N., (BBKS) A. S. S., 1986, ApJ 304, 15
Barnes J., Hut P., 1986, Nature 324, 446
Barnes J. E., Hernquist L., 1992, ARA&A 30, 705
Barrow J. D., Bhavsar S. P., Sonoda D. H., 1984, MNRAS 210, 19
Barrow J. D., Bhavsar S. P., Sonoda D. H., 1985, MNRAS 216, 17
Bennett D. P., Bouchet F. R., 1990, Phys. Rev D 41, 2408
Benoist C., Cappi A., Costa L. N. D., Maurogordato S., Bouchet F. R., Schaeffer R., 1999, ApJ 514, 563
Bertschinger E., 1998, ARA&A 36, 599
Bertschinger E., Dekel A., Faber S. M., Dressler A., Burstein D., 1990a, ApJ 364, 370
Bertschinger E., Gorski K. M., Dekel A., 1990b, Nature 345, 507
Bertschinger E., Juszkiewicz R., 1988, ApJ 334, L59

Blain A. W., Jameson A., Smail I., Longair M. S., Kneib J. ., Ivison R. J., 1999, MNRAS 309, 715
Blandford R. D., Rees M. J., 1978, Pittsburgh Conference on BL Lac objects
Bolton J. G., Peterson B. A., Wills B. J., Wills D., 1976, ApJ 210, L1
Bond J. R., Cole S., Efstathiou G., Kaiser N., 1991, ApJ 379, 440
Bondi H., 1952, MNRAS 112, 195
Borne K. D., Bushouse H., Lucas R. A., Colina L., 2000, ApJ 529, L77
Boyle B. J., Fong R., Shanks T., Peterson B. A., 1990, MNRAS 243, 1
Boyle B. J., Jones L. R., Shanks T., 1991, MNRAS 251, 482
Boyle B. J., McMahon R. G., Wilkes B. J., Elvis M., 1995, MNRAS 272, 462
Boyle B. J., Mo H. J., 1993, MNRAS 260, 925
Boyle B. J., Wilkes B. J., Elvis M., 1997, MNRAS 285, 511
Braccesi A., Formiggini L., Gandolfi E., 1970, A&A 5, 264
Brainerd T. G., Villumsen J. V., 1994, ApJ 431, 477
Brandenberger R. H., 1985, Rev. mod. Phys. 57, 1
Broadhurst T. J., Ellis R. S., Koo D. C., Szalay A. S., 1990, Nature 343, 726
Bunn E. F., White M., 1997, ApJ 480, 6
Burbidge G. R., Burbidge E. M., Sandage A. R., 1963, Rev. mod. Phys. 35, 947
Burles S., Nollett K. M., Truran J. N., Turner M. S., 1999, Phys. Rev. Lett. 82, 4176
Caldwell R. R., Dave R., Steinhardt P. J., 1998, Phys. Rev. Lett. 80, 1582
Calzetti D., Giavalisco M., Meiksin A., 1992, ApJ 398, 429
Cappi M., Mazzotta P., Elvis M., Burke D. J., Comastri A., Fiore F., Forman W., Fruscione A., Green P., Harris D., Hooper E. J., Jones C., Kaastra J. S., Kellogg E., Murray S., McNamara B., Nicastro F., Ponman T. J., Schlegel E. M., Siemiginowska A., Tananbaum H., Vikhlinin A., Virani S., Wilkes B., 2000, ApJ accepted
Carrera F. J., Barcons X., Fabian A. C., Hasinger G., Mason K. O., McMahon R. G., Mittaz J. P. D., Page M. J., 1998, MNRAS 299, 229
Carroll S. M., Press W. H., 1992, ARAA 30, 499
Cen R. Y., Ostriker J. P., Spergel D. N., Turok N., 1991, ApJ 383, 1
Chandrasekhar S., Muench G., 1952, ApJ 115, 103
Chen H. ., Lanzetta K. M., Pascarelle S., 1999, Nature 398, 586
Chu Y., Zhu X., 1983, ApJ 267, 4
Chu Y., Zhu X., 1988, A&A 205, 1
Clowes R. G., Campusano L. E., 1991, MNRAS 249, 218
Clowes R. G., Campusano L. E., 1994, MNRAS 266, 317
Clowes R. G., Haines C. P., Machura I. K., Campusano L. E., 1999, American Astronomical Society Meeting, 195, 1706
Cohen R. D., 1983, ApJ 273, 489
Colberg J. M., White S. M. D., MacFarland T. J., Jenkins A., Frenk C. S., Pearce F. R., Evrard A. E., Couchman H. M. P., Efstathiou G., Peacock J. A., Thomas P. A., 1998, in Wide Field Surveys in Cosmology 14th IAP meeting in Paris, eds. S. Colombi and Y. Mellier, 247
Coles P., 1996, Contemporary Physics 37, 429
Collins C. A., Guzzo L., Boehringer H., Schmuecker P., Chincarini G., Cruddace

R., Grandi S. D., MacGillivray H. T., Neumann D. M., Schindler S., Shaver P., Voges W., 2000, submitted to MNRAS
Condon J. J., Cotton W. D., Greisen E. W., Yin Q. F., Perley R. A., Taylor G. B., Broderick J. J., 1999, AJ 115, 1693
Coziol R., Iovino A., de Carvalho R. R., 2000, AJ 120, 47
Coziol R., Ribeiro A. L. B., de Carvalho R. R., Capelato H. V., 1998, ApJ 493, 563
Crampton D., Cowley A. P., Hartwick F. D. A., 1987, ApJ 314, 129
Crampton D., Cowley A. P., Hartwick F. D. A., 1989, ApJ 345, 59
Crane P., Hegyi D. J., Mandolesi N., Danks A. C., 1986, ApJ 309, 822
Croom S. M., Shanks T., 1996, MNRAS 281, 893
Croom S. M., Shanks T., 1999, MNRAS 303, 411
Dahari O., 1984, AJ 89, 966
Dalton G. B., Croft R. A. C., Efstathiou G., Sutherland W. J., Maddox S. J., Davis M., 1994, MNRAS 271, L47
Davis M., Peebles P. J. E., 1983, ApJ 267, 465
de Grijp M. H. K., Lub J., Miley G. K., 1987, A&AS 70, 95
de Lapparent V., Geller M. J., Huchra J. P., 1986, ApJ 302, L1
de Lapparent V., Geller M. J., Huchra J. P., 1988, ApJ 332, 44
de Robertis M. M., Yee H. K. C., Hayhoe K., 1998, ApJ 496, 93
Dekel A., Aarseth S. J., 1984, ApJ 283, 1
Dey A., Spinrad H., Stern D., Graham J. R., Chaffee F. H., 1998, ApJ 498, L93
Drinkwater M., 1988, MNRAS 235, 1111
Dultzin-Hacyan D., Krongold Y., Fuentes-Guridi I., Marziani P., 1999, ApJ 513, L111
Dussert C., Rasigni M., Llebaria A., 1988, J. Theor. Biol. 135, 295
Dussert C., Rasigni M., Palmari J., Rasigni G., Llebaria A., Marty F., 1987, J. Theor. Biol. 125, 317
Edge D. O., Shakesshaft J. R., McAdam W. B., Bladwin J. E., Archer S., 1959, MmRAS 68, 37
Efstathiou G., Davis M., White S. D. M., Frenk C. S., 1985, ApJS 57, 241
Einasto J., Einasto M., Frisch P., Gottlober S., Muller V., Saar V., Starobinsky A. A., Tago E., Tucker D., Andernach H., 1997a, MNRAS 289, 801
Einasto J., Einasto M., Frisch P., Gottlober S., Saar V. M. V., Starobinsky A. A., Tucker D., 1997b, MNRAS 289, 813
Einasto J., Klypin A. A., Saar E., Shandarin S. F., 1984, MNRAS 206, 529
Einasto M., Tago E., Jaaniste J., Einasto J., Andernach H., 1997c, A&AS 123, 119
Ellingson E., Yee H. K. C., Green R. F., 1991, ApJ 371, 49
Elvis M., Maccacaro T., Wilson A. S., Ward M. J., Penston M. V., Fosbury R. A. E., Perola G. C., 1978, MNRAS 183, 129
Engels D., Cordis L., Köhler T., 1994, IAU Symposium 161 eds. H. T. MacGillivray et al. (Kluwer, Dordrecht), 317
Engels D., Keil R., 2000, New Astronomy 44, 2
Fath E. A., 1911, ApJ 33, 58
Feldman F. R., Weedman D. W., Balzano V. A., Ransey L. W., 1982, ApJ 256,

427
Ferland G. J., Osterbrock D. E., 1986, ApJ 300, 658
Févre O. L., Hudon D., Lilly S. J., Crampton D., Hammer F., Tresse L., 1996, ApJ 461, 534
Fisher K. B., Bahcall J. N., Kirhakos S., Schneider D. P., 1996, ApJ 468, 469
Fisher K. B., Davis M., Strauss M. A., Yahil A., Huchra J., 1994, MNRAS 266, 50
Fixsen D. J., Cheng E. S., Gales J. M., Mather J. C., Shafer R. A., Wright E. L., 1996, ApJ 473, 576
French H. B., 1980, ApJ 240, 41
Fuentes-Williams T., Stocke J. T., 1988, AJ 96, 1235
Gamov G., 1946, Phys. Rev. 70, 572
Geller M. J., Huchra J. P., 1989, Science 246, 897
Georgantopoulos I., Shanks T., 1994, MNRAS 271, 773
Giavalisco M., Steidel C. C., Adelberger K. L., Dickinson M. E., Pettini M., Kellogg M., 1998, ApJ 503, 543
Girardi M., Boschin W., da Costa L. N., 2000, A&A 353, 57
Gottlöber S., Klypin A., Kravtsov A. V., 2000, submitted to ApJ
Graham M. J., Clowes R. G., Campusano L. E., 1995, MNRAS 275, 790
Graham R. L., Hell P., 1985, Annals of the History of Computing 7, 1
Greenstein J. L., Matthews T. A., 1963, AJ 68, 279
Groth E. J., Peebles P. J. E., 1977, ApJ 217, 385
Guth A. H., 1981, Phys. Rev. D 23, 347
Guzzo L., Bartlett J. G., Cappi A., Maurogordato S., Zucca E., Zamorani G., Balkowski C., Blanchard A., Cayatte V., Chincarini G., Collins C. A., Maccagni D., MacGillivray H., Merighi R., Mignoli M., Proust D., Ramella M., Scaramella R., Stirpe G. M., Vettolani G., 2000, A&A 355, 1
Guzzo L., Iovino A., Chincarini G., Giovanelli R., Haynes M. P., 1991, ApJ 382, L5
Guzzo L., Strauss M. A., Fisher K. B., Giovanelli R., Haynes M. P., 1997, ApJ 489, 37
Hagen H.-J., Groote D., Engels D., Reimers D., 1995, A&AS 111, 195
Haiman Z., Hui L., 2000, ApJ submitted
Haines C. P., Clowes R. G., Campusano L. E., 2000, IAU Symposia, 201, E62
Hall P. B., Green R. F., 1998, ApJ 507, 558
Hamilton A. J. S., 1993, ApJ 417, 19
Hartmann D., Burton W. B., 1997, Atlas of galactic neutral hydrogen Cambridge University Press, ISBN 0521471117
Heath D. J., 1977, MNRAS 179, 351
Heavens A. F., 1991, MNRAS 251, 267
Heckman T. M., 1980, A&A 87, 152
Hermit S., Santiago B. X., Lahav O., Strauss M. A., Davis M., Dressler A., Huchra J. P., 1996, MNRAS 283, 709
Hernquist L., 1987, ApJS 64, 715
Hernquist L., Barnes J. E., 1991, Nature 354, 210
Hernquist L., Mihos J. C., 1995, ApJ 448, 41
Hewett P. C., 1982, MNRAS 201, 867

Hewett P. C., Foltz C. B., Chaffee F. H., 1995, AJ 109, 1498
Hewitt A., Burbidge G., 1987, ApJS 63, 1
Hickson P., 1997, ARAA 35, 357
Hintzen P., Romanishin W., Valdes F., 1991, ApJ 366, 7
Hnatyk B. I., Lukash V. N., Novosyadlyj B. S., 1995, A&A 300, 1
Ho L. C., 1996, PASP 108, 637
Hockney R. W., Eastwood J. W., 1981, Numerical simulations using particles New York: McGraw-Hill
Hoffman R., Jain A. K., 1983, Patt. Rec. Lett. 1, 175
Hoyle F., Fowler W. A., 1963, MNRAS 125, 169
Hu E. M., McMahon R. G., Cowie L. L., 1999, ApJ 522, L9
Huchra J. P., 1977, ApJ 217, 928
Huchra J. P., Davis M., Latham D., Tonry J., 1983, ApJS 52, 89
Huchra J. P., Vogeley M. S., Geller M. J., 1999, ApJS 121, 287
Hutchings J. B., Crampton D., Johnson A., 1995, AJ 109, 73
Hutchings J. B., Crampton D., Persram D., 1993, AJ 106, 1324
Iovino A., Shaver P. A., 1988, ApJ 330, L13
Ivison R. J., Smail I., Barger A. J., Kneib J. ., Blain A. W., Owen F. N., Kerr T. H., Cowie L. L., 2000, MNRAS 315, 209
Jaaniste J., Tago E., Einasto M., Einasto J., Andernach H., Mueller V., 1998, A&A 336, 35
Jing Y. P., Mo H. J., Boerner G., 1998, ApJ 494, 1
Jones L. R., McHardy I. M., Merrifield M. R., Mason K. O., Smith P. J., Abraham R. G., Branduardi-Raymont G., Newsam A. M., Dalton G., Rowan-Robinson M., Luppino G., 1997, MNRAS 285, 547
Kaiser N., 1984, ApJ 284, L9
Kaiser N., 1986, MNRAS 222, 323
Kaiser N., 1987, MNRAS 227, 1
Kaiser N., Peacock J. A., 1991, ApJ 379, 482
Keel W. C., 1983, AJ 269, 466
Keil R., 2000, Diploma thesis University of Hamburg
Kerscher M., 1999, A&A 343, 333
Kerscher M., Szapudi I., Szalay A. S., 2000, astro-ph/9912088
Knebe A., Kravtsov A. V., Gottlöber S., Klypin A. A., 2000, MNRAS 317, 630
Kolb E. W., Turner M. S., 1990, The Early Universe Addison-Wesley Publishing Company
Komberg B. V., Kravtsov A. V., Lukash V. N., 1994, A&A 286, L19
Komberg B. V., Kravtsov A. V., Lukash V. N., 1996, MNRAS 282, 713
Komberg B. V., Lukash V. N., 1994, MNRAS 269, 277
Kormendy J., Richstone D., 1995, ARA&A 33, 581
Kravtsov A. V., Klypin A. A., Khokhlov A. M., 1997, ApJS 111, 73
Krolik J. H., 1999, Active Galactic Nuclei Princeton University Press
Kruskal J. B., 1956, Proc. Am. Math. Soc. 7, 48
Kundić T., 1997, ApJ 482, 631
Kunth D., Sargent W. L. W., 1986, AJ 91, 761
La Franca F., Andreani P., Cristiani S., 1998, ApJ 497, 529
La Franca F., Cristiani S., 1997, AJ 113, 1517

La Franca F., Cristiani S., Barbieri C., 1992, AJ 103, 1062
La Franca F., Lissandrini C., Cristiani S., Miller L., Hawkins M. R. S., McGillivray H. T., 1999, A&AS 140, 351
Lacey C., Cole S., 1993, MNRAS 262, 627
Lacy M., 2000, astro-ph/0005016
Lahav O., Lilje P. B., Primack J. R., Rees M. J., 1991, MNRAS 251, 128
Landy S. D., Shectman S. A., Lin H., Kirshner R. P., Oemler A. A., Tucker D., 1996, ApJ 456, L1
Landy S. D., Szalay A. S., 1993, ApJ 412, 64
Lasker B. M., Sturch C. R., et al. C. L., 1988, ApJS 68, 1L
Laurikainen E., Salo H., 1995, A&A 293, 683
Liddle A. R., Lyth D. H., 1993, MNRAS 265, 379
Liddle A. R., Lyth D. H., Viana P. T. P., White M., 1996, MNRAS 282, 281
Limber D. N., 1953, ApJ 117, 134
Limber D. N., 1954, ApJ 119, 655
Limber D. N., 1957, ApJ 125, 9
Linde A., 1993, Elementarteilchen und inflation"arer Kosmos Spektrum Akademischer Verlag
Ling E. N., Frenk C. S., Barrow J. D., 1986, MNRAS 223, 21
Lockman F. J., Jahoda K., McCammon D., 1986, ApJ 302, 432
Loveday J., Efstathiou G., Peterson B. A., Maddox S. J., 1992, ApJ 400, L43
Loveday J., Maddox S. J., Efstathiou G., Peterson B. A., 1995, ApJ 442, 457
Lynden-Bell D., 1969, Nature 223, 690
Lynden-Bell D., Faber S. M., Burstein D., Davies R. L., Dressler A., Terlevich R. J., Wegner G., 1988, ApJ 326, 19
Ma C.-P., Caldwell R. R., Bode P., Wang L., 1999, ApJ 521, L1
Maccacaro T., Ceca R. D., Gioia I. M., Morris S. L., Stocke J. T., Wolter A., 1991, ApJ 374, 117
MacKenty J. W., 1989, ApJ 343, 125
Maiolino R., Ruiz M., Rieke G. H., Keller L. D., 1995, ApJ 446, 561
Malkan M. A., Sargent W. L. W., 1982, ApJ 254, 22
Martini P., Pogge R. W., 1999, AJ 118, 2646
Martini P., Weinberg D. H., 2000, submitted to ApJ astro-ph/0002384
Mason K. O., Carrera F. J., Hasinger G., Andernach H., Aragon-Salamanca A., Barcons X., Bower R., Brandt W. N., Branduardi-Raymont G., Burgos-Martín J., Cabrera-Guerra F., Carballo R., Castander F., Ellis R. S., González-Serrano J. I., Martínez-González E., Martín-Mirones J. M., McMahon R. G., Mittaz J. P. D., Nicholson K. L., Page M. J., Pérez-Fournon I., Puchnarewicz E. M., Romero-Colmenero E., Schwope A. D., Vila B., Watson M. G., Wonnacott D., 2000, MNRAS 311, 456
Mathez G., 1976, A&A 53, 15
Mattig W., 1958, AN 284, 109
Maza J., Wischnjeweski M., Antezana R., Gonzalez L. E., 1995, Rev. Mex. Astron. Astrofis. 31, 119
McKellar A., 1940, PASP 52, 187
McLure R. J., Dunlop J. S., 2000, sub. to MNRAS astro-ph/0007219
Meinhold P., Lubin P., 1991, ApJ 370, L11

Mihos J. C., Hernquist L., 1996, ApJ 464, 641
Miyaji T., Hasinger G., Schmidt M., 2000, A&A 353, 25
Mo H. J., Fang L. Z., 1993, ApJ 410, 493
Mo H. J., Jing Y. P., Boerner G., 1992, ApJ 392, 452
Mo H. J., White D. M., 1996, MNRAS 282, 347
Morrison R., McCammon D., 1983, ApJ 270, 119
Mould J. R., Huchra J. P., Freedman W. L., Kennicutt R. C., Ferrarese L., Ford H. C., Gibson B. K., Graham J. A., Hughes S. M. G., Illingworth G. D., Kelson D. D., Macri L. M., Madore B. F., Sakai S., Sebo K. M., Silbermann N. A., Stetson P. B., 2000, ApJ 529, 786
Mulchaey J. S., Regan M. W., 1997, ApJ 482, L135
Mulchaey J. S., Zabludoff A. I., 1999, ApJ 514, 133
naga E. G., Baugh C. M., 1998, MNRAS 294, 229
Newman P. R., Clowes R. G., Campusano L. E., Graham M. J., 1998, Large Scale Structure: Tracks and Traces, 133
Neyman J., 1962, Problems in Extra-Galactic Research ed. G. C. McVittie (Macmillan New York), 294
Neyman J., Scott E. L., 1952, ApJ 116, 144
Neyman J., Scott E. L., Shane C. D., 1953, ApJ 117, 92
Nishiura S., Sato Y., Murayama Y., Taniguchi Y., 1997, IAU Symp. 186 Galaxy Interactions at Low and High Redshift, eds. J. E. Barnes & D. B. Sanders (Dordrecht: Kluwer)
Norman C., Scoville N., 1988, ApJ 332, 124
Oort J. H., 1981, A&A 94, 359
Oort J. H., 1983, ARA&A 21, 373
Osmer P. S., 1980, ApJS 42, 523
Osmer P. S., 1981, ApJ 247, 762
Osmer P. S., Hewett P. C., 1991, ApJS 75, 273
Osmer P. S., Smith M. G., 1980, ApJS 42, 333
Ostriker J. P., Lubin L. M., Hernquist L., 1995, ApJ 444, L61
Page M. J., Carrera F. J., Hasinger G., Mason K. O., McMahon R. G., Mittaz J. P. D., Barcons X., Carballo R., Gonzalez-Serrano I., Perez-Fournon I., 1996, MNRAS 281, 579
Page M. J., Mason K. O., McHardy I. M., Jones L. R., Carrera F. J., 1997, MNRAS 291, 324
Park C., Gott J. R. I., 1991, MNRAS 249, 288
Peacock J. A., 1999, Cosmological Physics Cambridge University Press
Peacock J. A., Dodds S. J., 1994, MNRAS 267, 1020
Peacock J. A., Nicholson D., 1991, MNRAS 253, 307
Peebles J. P. E., 1973, ApJ 185, 413
Peebles J. P. E., 1980, The Large-Scale Structure of the Universe Princeton University Press
Penzias A. A., Wilson R. W., 1965, ApJ 142, 419
Peterson B. A., 1970, AJ 75, 695
Peterson B. A., 1997, Cambridge University Press An introduction to active galactic nuclei
Petrosian A. R., 1982, Astrofizika 18, 548

Pfeffermann E., Briel U. G., Hippmann H., 1988, Proc. SPIE 733, 519
Phillips A. C., Illingworth G. D., MacKenty J. W., Franx M., 1996, AJ 111, 1566
Ponman T. J., Allan D. J., Jones L. R., Merrifield M., McHardy I. M., Lehto H. J., Luppino G. A., 1994, Nature 369, 462
Ponman T. J., Bertram D., 1993, Nature 363, 51
Popowski P. A., Weinberg D. H., Ryden B. S., Osmer P. S., 1998, ApJ 498, 11
Postman M., Geller M. J., Huchra J. P., 1986, AJ 91, 1267
Postman M., Geller M. J., Huchra J. P., 1988, AJ 95, 267
Press W. H., Schechter P., 1974, ApJ 187, 425
Prim R. C., 1957, Bell Sys. Tech. J. 36, 1389
Quillen A. C., Alonso-Herrero A., Rieke M. J., McDonald C., Falcke H., Rieke G. H., 1999, ApJ 525, 685
Rafanelli P., Violato M., Baruffolo A., 1995, AJ 109, 1546
Rees M. J., 1984, ARA&A 22, 471
Regan M. W., Mulchaey J. S., 1999, AJ 117, 2676
Ribeiro A. L. B., de Carvalho R. R., Coziol R., Capelato H. V., Zepf S. E., 1996, ApJ 463, L5
Roth K. C., Meyer D. M., 1993, ApJ 413, L67
Rubin V. C., 1954, PhD Thesis Georgetown University
Sabbey C. N., 2000, PASP 112, 867
Sachs R. K., Wolfe A. M., 1967, ApJ 147, 73
Sahni V., Coles P., 1995, Physics Reports 262, 1
Salpeter E. E., 1964, ApJ 140, 796
Sánchez S. F., González-Serrano J. I., 1999, A&A 352, 383
Sanders D. B., Mirabel I. F., 1996, ARA&A 34, 749
Sanders D. B., Soifer B. T., Elias J. H., Neugebauer G., Matthews K., 1988, ApJ 328, L35
Savage A., Bolton J. G., 1979, MNRAS 188, 599
Schmidt M., 1963, Nature 197, 1040
Schmidt M., 1968, ApJ 151, 393
Schmidt M., 1969, ARA&A 7, 527
Schmidt M., Green R. F., 1983, ApJ 269, 352
Schneider D. P., Gunn J. E., 1982, ApJ 263, 14
Schneider D. P., Schmidt M., Gunn J. E., 1994, AJ 107, 1245
Schwarz M. P., 1981, ApJ 247, 77
Setti G., Woltjer L., 1977, ApJ 218, L33
Seyfert C. K., 1943, ApJ 97, 28
Shane C. D., Wirtanen C. A., 1967, Publ. Lick Obs. 22, Part 1.
Shanks T., Boyle B. J., 1994, MNRAS 271, 753
Shanks T., Fong R., Boyle B. J., Peterson B. A., 1987, MNRAS 227, 739
Shanks T., Georgantopoulos I., Stewart G. C., Pounds K. A., Boyle B. J., Griffiths R. E., 1991, Nature 353, 315
Shapley H., 1930, Harvard Obs. Bull. 874, 9
Shaver P. A., 1984, A&A 136, L9
Shectman S. A., Landy S. D., Oemler A., Tucker D. L., Lin H., Kirshner R. P., Schechter P. L., 1996, ApJ 470, 172

Shepherd C. W., Carlberg R. G., Yee H. K. C., Ellingson E., 1997, ApJ 479, 82
Shields G. A., 1978, Nature 272, 706
Shimada M., Ohyama Y., Nishiura S., Murayama T., Taniguchi Y., 2000, AJ 119, 2664
Shlosman I., Begelman M. C., Frank J., 1990, Nature 345, 679
Shlosman I., Frank J., Begelman M. C., 1989, Nature 338, 45
Shuder J. M., Osterbrock D. E., 1981, ApJ 250, 55
Silk J., Weinberg D., 1991, Nature 350, 272
Simkin S. M., Su H. J., Schwarz M. P., 1980, ApJ 237, 404
Small T. A., Ma C.-P., Sargent W. L. W., Hamilton D., 1999, ApJ 524, 31
Smith H. J., Hoffleit D., 1963, AJ 68, 293
Smith R. J., Boyle B. J., Maddox S. J., 1995, MNRAS 277, 270
Smith R. J., Boyle B. J., Maddox S. J., 2000, MNRAS 313, 252
Smoot G., Bennett C., Weber R., Maruschak J., Ratliff R., Janssen M., Chitwood J., Hilliard L., Lecha M., Millis R., Patschke R., Richards C., Backus C., Mather J., Hauser M., Weiss R., Wilkinson D., Gulkis S., Boggess N., Cheng E., Kelsall T., Lubin P., Meyer S., Moseley H., Murdock T., Shafer R., Silverberg R., Wright E., 1990, ApJ 360, 685
Soifer B. T., Sanders D. B., Madore B. F., Neugebauer G., Danielson G. E., Elias J. H., Lonsdale C. J., Rice W. L., 1987, ApJ 320, 238
Spinrad H., Stern D., Bunker A., Dey A., Lanzetta K., Yahil A., Pascarelle S., Fernández-Soto A., 1998, AJ 116, 2617
Stark A. A., Gammie C. F., et al. R. W. W., 1992, ApJS 79, 77
Steidel C. C., Adelberger K. L., Dickinson M., Giavalisco M., Pettini M., Kellogg M., 1998, ApJ 492, 428
Stephan M., 1877, MNRAS 37, 334
Stephens A. W., Schneider D. P., Schmidt M., Gunn J. E., Weinberg D. H., 1997, AJ 114, 41
Stocke J. T., Morris S. L., Gioia I. M., Maccacaro T., Schild R., Wolter A., Fleming T. A., Henry J. P., 1991, ApJS 76, 813
Stockton A. N., 1972, Nature Physical Science 238, 37
Strauss M. A., A Y., Davis M., 1991, PASP 103, 1012
Strauss M. A., Willick J. A., 1995, Physics Reports 261, 271
Struck C., 1999, Physics Reports 321, 1-137
Subramanian K., Padmanabhan T., 1993, MNRAS 265, 101
Sugiyama N., 1995, ApJS 100, 281
Tanaka I., Yamada I., Turner E. L., Suto Y., 2001, ApJ accepted
Tananbaum H., Avni Y., Branduardi G., 1979, ApJ 234, L9
Taniguchi Y., 1999, ApJ 524, 65
Tesch F., Engels D., 2000, MNRAS 313, 377
Toomre A., Toomre J., 1972, ApJ 178, 623
Totsuji H., Kihara T., 1969, PASJ 21, 221
Trevese D., Cirimele G., Cencie A., Appodia B., Flin P., Hickson P., 1997, A&AS 125, 459
Trümper J., 1991, ROSAT call for proposals for the second observing period technical appendix

Tucker D. L., Jr. A. O., Kirshner R. P., Lin H., Shectman S. A., Landy S. D., Schechter P. L., Mueller V., Gottloeber S., Einasto J., 1997, MNRAS 285, L5
Tully R. B., 1986, ApJ 303, 25
Tully R. B., 1987, ApJ 323, 1
Tully R. B., 1992, ApJ 388, 9
van Breugel W., de Breuck C., Stanford S. A., Stern D., Röttgering H., Miley G., 1999, ApJ 518, L61
van Dalen A., Schaeffer R. K., 1992, ApJ 398, 33
Veilleux S., Osterbrock D. E., 1987, ApJS 63, 295
Véron-Cetty M.-P., Véron P., 1991, ESO Sci. Rep. N10 A catalogue of Quasars and Active Nuclei. ESO, Garching
Vilenkin A., Shellard E. P. S., 1994, Cosmic Strings and Other Topological Defects Cambridge University Press
Voges W., Aschenbach B., et al. T. B., 1999, A&A 349, 389
Walker I. R., Mihos J. C., Hernquist L., 1996, ApJ 460, 121
Wampler E. J., Baldwin J. A., Burke W. L., Robinson L. B., Hazard C., 1973, Nature 246, 203
Wang L., Caldwell R. R., Ostriker J. P., Steinhardt P. J., 2000, ApJ 530, 17
Warren S. J., Hewett P. C., Irwin M. J., Osmer P. S., 1987, Nature 330, 453
Warren S. J., Hewett P. C., Osmer P. S., 1991, ApJS 76, 23
Webster A., 1982, MNRAS 199, 683
Weedman D. W., Feldman F. R., Balzano V. A., Ramsey L. W., 1981, ApJ 248, 105
Weinberg S., 1972, Gravitation and Cosmology New York: Wiley, p. 413
Weymann R. J., Stern D., Bunker A., Spinrad H., Chaffee F. H., Thompson R. I., Storrie-Lombardi L. J., 1998, ApJ 505, L95
Wilkes B. J., Elvis M., 1987, APJ 323, 243
Williger G. M., Campusano L. E., Clowes R. G., 1999, American Astronomical Society Meeting, 194, 8703
Wills B. J., Netzer H., Wills D., 1985, ApJ 288, 94
Wold M., Lacy M., Lilje P. B., Serjeant S., 2000, MNRAS 316, 267
Wright E. L., Mather J. C., Fixsen D. J., Kogut A., Shafer R. A., Bennett C. L., Boggess N. W., Cheng E. S., Silverberg R. F., Smoot G. F., Weiss R., 1994, ApJ 420, 450
Wurtz R., Stocke J. T., Ellingson E., Yee H. K. C., 1997, ApJ 480, 547
Xu C., Sulentic J. W., Tuffs R., 1999, ApJ 512, 178
Yahil A., Strauss M. A., Davis M., Huchra J. P., 1991, ApJ 372, 380
Yamada T., Tanaka I., Aragon-Salamanca A., Kodama T., Ohta K., Arimoto N., 1997, ApJ 487, L125
Yee H. K. C., 1987, AJ 94, 1461
Yee H. K. C., Ellingson E., 1993, ApJ 411, 43
Yee H. K. C., Green R. F., 1984, ApJ 280, 79
Zel'Dovich Y. B., 1970, A&A 5, 84
Zitelli V., Mignoli M., Zamorani G., Marano M., Boyle B. J., 1992, MNRAS 256, 349
Zwicky F., 1971, Catalog of Selected Compact and of Post Eruptive Galaxies

Textbooks

This is a list of used and recommended textbooks for the work in the field of AGNs and large-scale structures. Some of the quoted books appear in the references too, but most of them do not, although motivation or ideas arose from them.

Quasars and Active Galactic Nuclei
A. K. Kembhavi and J. V. Narlikar
Cambridge University Press, 1999

An introduction to active galactic nuclei
B. M. Peterson
Cambridge University Press, 1997

Active Galactic Nuclei J. Krolik
Princeton University Press, 1999

Cosmological Physics
J. A. Peacock
Cambridge University Press, 1999

Large-scale structure in the Universe
A. Fairall
Wiley-Praxis Series in Astronomy and Astrophysics, 1998

Unsolved problems in astrophysics
J. N. Bahcall and J. P. Ostriker
Princeton University Press, 1997

Teilchenastrophysik
H. V. Klapdor-Kleingrothaus und K. Zuber
Teubner Stuttgart 1997

Formation of structure in the Universe
A. Dekel and J. P. Ostriker
Cambridge University Press, 1999

Structure formation in the Universe
T. Padmanabhan
Cambridge University Press, 1993

The large-scale structure of the Universe
P. J. E. Peebles
Princeton University Press, 1980

Cosmology
P. Coles and F. Lucchin
John Wiley & Sons, 1995

The Early Universe
E. W. Kolb and M. S. Turner
Addison-Wesley Publishing Company, 1990

Is the Universe Open or Closed?
P. Coles and G. F. R. Ellis
Cambridge University Press, 1997

Cosmology and large scale structure
Les Houches, Session LX, Nato ASI
R. Schaeffer, J. Silk, M. Spiro and J. Zinn-Justin
North Holland, 1996

Galaxy interactions at low and high redshift
IAU Symposium No. 186
J. E. Barnes and D. B. Sanders
Kluwer Academic Publishers, 1999

Statistics in theory and practice
R. Lupton
Princeton University Press, 1993

Ich erkläre, daß ich diese Arbeit selbständig und nur mit den angegebenen Quellen und Hilfsmitteln angefertigt habe.

Hamburg, 10.10.2000